THE UNIVERSITY OF CHICAGO

BOUNDARY MULTIFRACTALITY AND CONFORMAL INVARIANCE AT
LOCALIZATION-DELOCALIZATION TRANSITIONS

A DISSERTATION SUBMITTED TO
THE FACULTY OF THE DIVISION OF THE PHYSICAL SCIENCES
IN CANDIDACY FOR THE DEGREE OF
DOCTOR OF PHILOSOPHY

DEPARTMENT OF PHYSICS

BY
ARVIND R. SUBRAMANIAM

CHICAGO, ILLINOIS
DECEMBER 2008

To my late grandmother, Visalakshy.

Abstract

Disordered non-interacting electronic sytems can undergo transitions between delocalized and localized single particle wavefunctions as their energy is varied. In this thesis, mutifractal behavior of wavefunctions at such transitions near sample boundaries and corners and its relation to conformal invariance in two dimensions are studied. The concepts of boundary and corner multifractality are formulated and the influence of boundaries on various observables is analyzed from a general perspective. These ideas are then applied to a number of localization-delocalization (LD) transitions, each occurring in a single-particle system with a distinct dimensionality and symmetry. These analyses reveal a number of expected as well as novel features some of which are specific to the systems studied while others are common to all LD transitions. Study of boundary multifractality has a direct bearing on the nature of the unknown critical theories for LD transitions. In addition, the behavior of entanglement entropy near LD transitions has been analyzed and its scaling behavior illustrated in a few model systems.

Acknowledgments

I am grateful to my thesis advisor Prof. Ilya Gruzberg who has guided me through every aspect of my graduate school career. His scientific and professional mentoring have played an indispensable role in shaping my transition from a student to a researcher. I am thankful to him for being extremely supportive in all my research and career pursuits.

I thank Prof. Andreas Ludwig in UCSB for his collaboration in many of the research topics explored in this thesis and for his willingness to patiently explain a number of difficult concepts. I am also grateful to my other main collaborators, Prof. Akira Furusaki and Dr. Hideaki Obuse in RIKEN, Japan and Prof. Alexander Mirlin in Karlsruhe University, Germany. All of them devoted a great deal of time and effort to teach me different topics in the field of disordered electronic systems. I acknowledge my other collaborators, Prof. Sudip Chakravarty in UCLA and his student Xun Jia as well as Prof. Ferdinand Evers and Dr. Achim Mildenberger in Karlsruhe, Germany for performing some of the numerical simulations reported in this thesis.

I acknowledge Prof. Woowon Kang, Prof. Emil Martinec and Prof. Gene Mazenko for serving on my thesis committee and for reviewing my thesis. I thank Nobuko McNeill, the graduate secretary in the physics department at the University of Chicago for cheerfully helping me with all the adminstrative issues throughout my graduate school years. I acknowledge all my graduate school friends who were part of numerous stimulating discussions. I thank my classmates, Jonathan Logan and Sophia Domokos who helped me in choosing the right research direction at the end of my first year.

Finally, I thank my parents and sister for their unconditional love and support

and helping me tide over all challenges in every stage of my life. I thank my friends Mani Mathur, Aswath Manohar, Aneesh Chamakuzhi and Suresh Manohar for providing clear advice and helping me through numerous difficulties. I acknowledge Mara Werner and her family who have treated me with much kindness and affection.

List of Publications

This thesis is based on research reported in the following publications:

1. *Surface criticality and multifractality at localization transitions*, **A. R. Subramaniam**, I. A. Gruzberg, A. W. W. Ludwig, F. Evers, A. Mildenberger, A. D. Mirlin, Phys. Rev. Lett. **96**, 126802 (2006), cond-mat/0512040.

2. *Surface and corner multifractality at the metal-insulator transition in the two-dimensional spin-orbit (symplectic) symmetry class*, H. Obuse, **A. R. Subramaniam**, A. Furusaki, I. A. Gruzberg, A. W. W. Ludwig, Phys. Rev. Lett. **98**, 156802 (2007), cond-mat/0609161.

3. *Boundary multifractality in critical 1D systems with long-range hopping*, A. Mildenberger, **A. R. Subramaniam**, R. Narayanan, F. Evers, I. A. Gruzberg, A. D. Mirlin, Phys. Rev. B **75**, 094204 (2007), cond-mat/0611713.

4. *Corner multifractality for reflex angles and conformal invariance at 2D Anderson metal-insulator transition with spin-orbit scattering*, H. Obuse, **A. R. Subramaniam**, A. Furusaki, I. A. Gruzberg, A. W. W. Ludwig, Physica E **40**, 1404 (2008), arXiv:0709.1018.

5. *Entanglement entropy and multifractality at localization transitions*, X. Jia, **A. R. Subramaniam**, I. A. Gruzberg, S. Chakravarty, Phys. Rev. B **77**, 014208 (2008), arXiv:0710.1871.

6. *Boundary multifractality at the integer quantum Hall plateau transition: implications for the critical theory*, H. Obuse, **A. R. Subramaniam**, A. Furusaki, I. A. Gruzberg, A. W. W. Ludwig, Phys. Rev. Lett. **101**, 116802 (2008), arXiv:0804.2409.

7. *Boundary criticality and multifractality at the 2D spin quantum Hall transition,*
   A. R. Subramaniam, I. A. Gruzberg, A. W. W. Ludwig, Phys. Rev. B (to
   be published), arXiv:0803.1343.

Table of Contents

List of Figures

List of Tables

Chapter 1

Introduction

Five decades ago, Anderson found [1] that a single quantum particle moving in a random potential can get localized in space. In particular, at a given energy and disorder strength, all wave functions of the particle are either localized or delocalized. This implies that there can be transitions between localized and delocalized states as the energy of the particle is varied. Such transitions are commonly referred to as Anderson transitions or more generally as localization-delocalization (LD) transitions (for a recent review, see [2]). Significant progress in understanding the nature of these transitions was achieved through the development of scaling theory [3] and field theoretic descriptions [4] of localization. These ideas emphasized the analogy between the LD transition and conventional second-order phase transitions.

One of the central results arising out of the scaling and field theory based formulations was that an arbitrarily weak disorder is sufficient to localize a quantum particle in two and lower dimensions. This can be formalized using perturbative and renormalization group (RG) calculations. A number of exceptions to this result have been found, the most spectacular and experimentally important one being the integer quantum Hall (IQH) plateau transition [5]. Other examples include systems with time reversal symmetry but broken spin rotation symmetry (the so called symplectic-class), particle-hole symmetric systems (superconducting classes) and systems with sublattice symmetry (chiral classes). The natural question to ask is whether the LD transitions occurring in these two dimensional (2D) systems can be described using a field theoretic formulation. In fact, in the light of exact conformal field theory techniques which have been developed for conventional second-order phase transitions in 2D [6], we might very well ask for similar non-perturbative formulations of the 2D LD

critical points. This has been achieved for a few LD transitions but the important IQH and symplectic-class critical point theories have remained elusive till today.

Despite the aforementioned issue, our understanding of LD transitions has been greatly refined due to a number of important developments. One of them is the symmetry classification proposed by Altland and Zirnbauer [7, 8] which puts each disordered system with a distinct symmetry in correspondence with one of the ten families of symmetric spaces of Cartan. This idea was central to the discovery of delocalized phases in some of the previously mentioned 2D systems and has also given us a broader perspective of all possible disordered single particle systems that can occur. We summarize this classification in Table 1.1 at the end of this chapter. Another important development has been the description of critical wave functions at the LD transition using the language of multifractality. The similarities and distinctions between multifractal and ordinary critical behavior have given us keen insights into the nature of the field theories which can describe LD transitions.

A key aspect of ordinary critical behavior is that the scaling behavior of observables in the critical theory which are measured near the boundary can be significantly different from those of bulk observables. In particular, the boundary ('surface') scaling dimensions of observables can be (and typically are) distinct from their bulk scaling dimensions. From this perspective, a very natural question to ask is how does one understand multifractality at the LD transitions in the presence of a boundary. Answering this question is the main motivation for this thesis work. This investigation has a number of implications. One of them is that the 2D LD critical points are expected to be conformally invariant and in the case of an unknown field theory for the bulk, boundaries can constrain and restrict this unknown bulk theory. This idea has already been demonstrated in the context of ordinary 2D critical behavior [9]. Moreover, systems with boundary can be used to unambiguously test the hypothesis

of conformal invariance itself which is often assumed to exist at the unknown 2D critical points describing the LD transitions.

The investigation of boundary multifractality at LD transitions reveals a number of expected as well as novel features which are described in this thesis. Chapter 2 deals with the concept of boundary multifractality in a generic situation and sets forth the essential ideas. In particular, we find the surprising result that boundary contribution can dominate over the bulk contribution to multifractality even in the thermodynamic limit, for certain observables. In the same chapter, we also recapitulate some essential concepts on conformal invariance in systems with boundary and derive consequences of this conformal invariance for multifractality. While all this is done with LD critical points in mind, the applicability of the results is much more general and they can be used to study boundary critical behavior in any system where multifractal scaling and conformal invariance are expected to be present, such as in random 2D magnets.

From Chapter 3 onwards, we investigate boundary multifractality at various specific LD critical points (The 2D transitions below are among the ones listed in Table 1.1). In Chapter 3, we investigate the 2D spin quantum Hall transition and calculate multifractal exponents using a supersymmetric network model. In Chapter 4, we study a one dimensional model of random power-law banded matrices which exhibits critical behavior. We discover a one-dimensional family of boundary critical theories and analyze the corresponding multifractal behavior. In Chapter 5 and 6, we apply some of the general principles of boundary multifractal analysis to understand numerical simulations (done by collaborators) and constrain possible candidate theories for the 2D symplectic-class transition and the IQH plateau transition, respectively. In Chapter 7, we describe the relation between the language of multifractal analysis and entanglement entropy in disordered non-interacting electron systems. In Chapter 8, we provide a brief summary and possible future directions. Some of the

Usual Designation	TRS	SRS	CS	SC	Well known 2D transitions
A	-	±	-	-	Integer quantum Hall plateau transition
AI	+	+	-	-	
AII	+	-	-	-	Symplectic-class transition
AIII	-	±	+	-	Line of fixed points
BDI	+	+	+	-	Line of fixed points
CII	+	-	+	-	Line of fixed points
C	-	+	-	+	Spin quantum Hall transition
CI	+	+	-	+	
BD	-	-	-	+	Thermal quantum Hall transition
DIII	+	-	-	+	

Table 1.1: Symmetry classes of disordered electronic systems from [8]. The $+$ and $-$ symbols denote the presence or absence respectively, of a particular symmetry. TRS - time reversal symmetry, SRS - spin rotation symmetry, CS - chiral symmetry, SC - superconductor. The line of fixed points occurs in the chiral classes because the vector potential disorder in the chiral classes is an exactly marginal perturbation [10].

technical details regarding the spin quantum Hall transition have been relegated to the appendices: Appendix A gives the relevant representation theory of the sl(2|1) superalgebra. Appendix B discusses the supersymmetry at the boundary of the spin quantum Hall network model.

Chapter 2

Multifractality and Conformal Invariance - Generalities

2.1   Multifractal scaling

Multifractal scaling refers to the existence of an infinite set of critical exponents characterizing the scaling behavior of moments of some distribution. This has been observed in a wide variety of complex systems such as in turbulence, chaotic dynamical systems and diffusion-limited aggregation. In the context of LD transitions, multifractal exponents characterize the scaling of moments of the wave function intensity. The exponents reflect the strong spatial fluctuations of the critical wave functions.

The wave function moments conventionally appear in the form of the so-called averaged generalized inverse participation ratios (IPR) P_q (the overbar below denotes disorder average):

$$P_q = \int d^d r \; \overline{|\psi(r)|^{2q}} \tag{2.1}$$

Here $\psi(r)$ denotes the wave function amplitude and the integration is typically carried out over the whole sample volume of dimension d.

Since we are interested in studying the scaling of wave functions in other geometries, we define a more general version of the above quantity:

$$P_q^x = \int_{\mathcal{M}_x} d^{D_x} r_x \; \overline{|\psi(r_x)|^{2q}}. \tag{2.2}$$

Here, D_x is the dimension of the region $\mathcal{M}_x$ over which the wave function intensity is integrated over. In particular, we will be interested in the cases of bulk $(x = b)$, boundary or surface $(x = s)$ and corner $(x = c)$ where D_x takes on the values d,

$d - 1$ and $d - 2$, respectively. Boundaries and corners are defined in the same sense as in usual critical phenomena. For example, boundaries refer to region of finite width (in terms of a lattice model) along the boundary where the scaling behavior of observables is distinctly different from those observed deep in the bulk, far away from any boundary. Corners are also defined in a similar way.

In a critical system, P_q^x exhibits multifractal scaling:

$$P_q^x \propto L^{D_x} \overline{|\psi(r_x)|^{2q}} \propto L^{-\tau_q^x}, \qquad \tau_q^x = dq + \Delta_q^x + q\mu_x - D_x. \qquad (2.3)$$

Here L is the linear system size and τ_q^x is called the multifractal spectrum and Δ_q^x is often referred to as 'anomalous' multifractal exponent or dimension. Multifractal scaling is synonymous with a non-linear dependence of Δ_q^x on q. Depending on the region of interest $\mathcal{M}_x$, the corresponding multifractal dimensions are denoted by Δ_q^b, Δ_q^s and Δ_q^c referring to bulk, boundary (surface) and corner dimensions respectively.

Note that Δ_0^x is always zero, by definition. Further $\Delta_1^b = 0$ due to the fact that wave function intensities are normalized to unity with respect to the whole system (implying $P_{q=1}^b = 1$ and $\mu_b = 0$). There is no such general constraint for Δ_1^s and Δ_1^c. However, we adopt the convention of setting them equal to zero and the corresponding contribution to τ_1^x is reflected in μ_s and μ_c respectively. With this choice, a non-vanishing exponent μ_x characterizes a non-trivial scaling behavior of the local wave function intensity at the sample location r_x,

$$L^d \, \overline{|\psi(r_x)|^2} \propto 1/L^{\mu_x} \qquad (2.4)$$

which is known to occur in certain non-conventional Anderson localization symmetry classes [8, 7]. We will relate Δ_q^x and μ_x to the scaling dimensions of field theory

operators in Sec. 2.3.

2.2 Singularity spectrum - boundary and corner

Another way to characterize multifractal behavior is through the singularity spectrum $f(\alpha)$. Similar to the previous section, here we use a general notation which is valid for bulk, boundary and corner points in the sample. Formally $f^x(\alpha^x)$ is the Legendre transform of τ_q^x:

$$f^x(\alpha^x) = \alpha^x q - \tau_q^x, \quad \alpha^x = \frac{d\tau_q^x}{dq}. \tag{2.5}$$

More physically, $f^x(\alpha^x)$ is the fractal dimension of all points r_x in the sample where the wave function intensity has the scaling behavior $|\psi(r_x)|^2 \sim L^{-\alpha}$. This is evident by looking at the distribution function for the wave function intensity which has the scaling behavior,

$$P(|\psi(r_x)|^2) \sim |\psi(r_x)|^{-2} L^{f^x(\alpha^x) - d_x}, \qquad \alpha^x = -\ln|\psi(r_x)|^2 / \ln L. \tag{2.6}$$

Note that α^x cannot be negative since the wave function intensity has to be normalizable. $f^x(\alpha^x)$ cannot be negative for a single sample, but the disorder averaged $f^x(\alpha^x)$ can be negative due to contributions from rare realizations of disorder which will not occur in a typical sample (for a discussion of this point, see Ref. [11]).

Above we chose to define the singularity spectrum $f^x(\alpha^x)$ separately for the bulk, boundary and corner cases. To illustrate another important point (see also Ref. [12]), for the sake of simplicity let us consider a sample with just bulk and boundary regions without any corners. One can now ask the following question: Imagine that one performs a multifractal analysis for the whole sample, without separating it into bulk

and boundary regions. Would the boundary exponents then play any role? A naive answer is no: since the weight of boundary points is down by a factor $1/L$, one could expect that only the bulk exponents would matter. This is however, not true. To illustrate this point, we take an example where the whole multifractal spectrum can be studied analytically. Consider a 2D weakly localized metallic system (dimensionless conductance $g \gg 1$), which shows weak multifractality [13,14] on length scales below the localization length $\xi \sim e^{(\pi g)^{\beta}}$, where $\beta = 1$ (2) for systems with preserved (broken) time-reversal symmetry. (With minor modifications, the formulas below describe also the Anderson transition in $2 + \epsilon$ dimensions).

The bulk multifractal spectrum of this system was obtained via the perturbative renormalization group treatment of the underlying field theory (σ-model) [15] and also within the instanton approach [13,14]. The result reads

$$\tau_q^b = 2q + \gamma q(1-q) - 2; \qquad \gamma = (\beta \pi g)^{-1} \ll 1. \tag{2.7}$$

This can be readily generalized to the case of a semi-infinite sample with reflecting boundary giving,

$$\tau_q^s = 2q + 2\gamma q(1-q) - 1. \tag{2.8}$$

Each of the three terms in the above equations correspond to the non-zero terms contributing to τ_q^x in (2.3) with $\mu^x = 0$. The factor of 2 in front of the second term (anomalous multifractal exponent) can be traced back to using the half-space Neumann Green's function instead of the full-plane version (for e.g., see [16]). Performing the Legendre transformation, we find the corresponding singularity spectra,

$$f^b(\alpha^b) = 2 - (\alpha^b - 2 - \gamma)^2/4\gamma, \tag{2.9}$$

$$f^s(\alpha^s) = 1 - (\alpha^s - 2 - 2\gamma)^2/8\gamma. \tag{2.10}$$
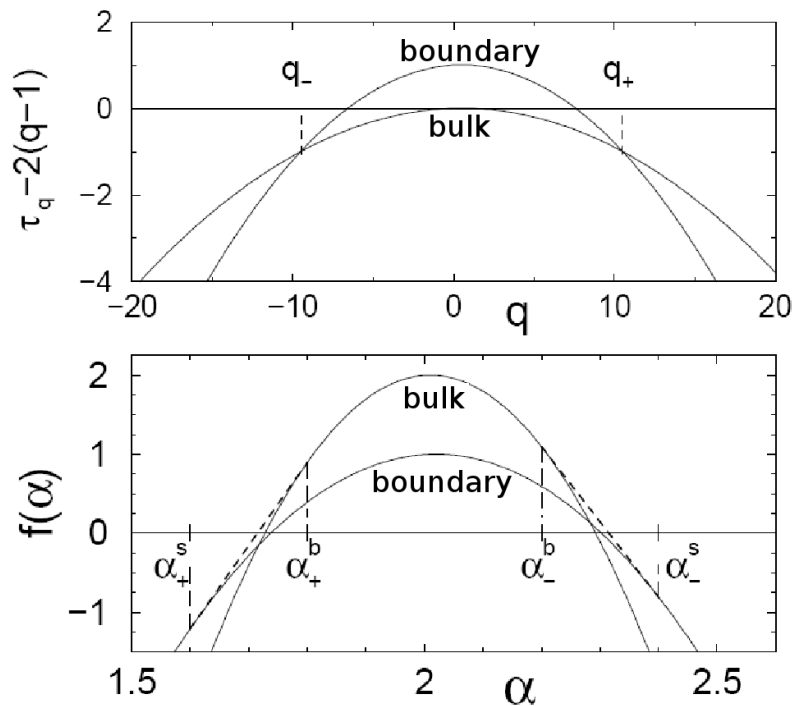
Figure 2.1: Boundary and bulk multifractal and singularity spectra for a 2D metal with $\gamma = 0.01$.

These results are illustrated in Fig. 2.1 and understood in the following way. The scaling behavior of the wave-function moments integrated over the whole sample can be analyzed using a scaling form which interpolates between the bulk and boundary (ρ denotes the distance perpendicular to the boundary):

$$\int_{\text{whole sample}} d^d r \overline{|\psi(r)|^{2q}} \sim L^{d-1} \int_1^L d\rho \left(\frac{L}{\rho}\right)^{-\tau_q^s - d + 1} \rho^{-\tau_q^b - d}, \qquad (2.11)$$

$$\sim \begin{cases} L^{-\tau_q^s}, \tau_q^s < \tau_q^b, \\ L^{-\tau_q^b}, \tau_q^b < \tau_q^s. \end{cases} \qquad (2.12)$$

We see that the lowest of the τ_q exponents 'wins' since the corresponding term will dominate in the limit of large system size L. It is easy to see that the boundary effects

become dominant outside the range $q_- < q < q_+$, where $q_\pm \simeq \pm\gamma^{-1/2}$ are the roots of the equation $\tau_q^b = \tau_q^s$. The lower panel of Fig. 2.1 shows how this is translated into the $f(\alpha)$ for the whole sample. The total singularity spectrum $f(\alpha)$ is given by the bulk function $f^b(\alpha^b)$ only for $\alpha_+^b < \alpha < \alpha_-^b$, where $\alpha_\pm^b - 2 \simeq \mp 2\gamma^{1/2}$. Outside this range boundary effects are important. Specifically, $f(\alpha)$ is equal to the boundary spectrum $f^s(\alpha^s)$ for $\alpha < \alpha_+^s$ and $\alpha > \alpha_-^s$, where $\alpha_\pm^s - 2 \simeq \mp 4\gamma^{1/2}$, while in the intermediate intervals $\alpha_+^s < \alpha < \alpha_+^b$ and $\alpha_-^b < \alpha < \alpha_-^s$ its dependence on α becomes linear (shown by dashed lines). The latter behavior is governed by intermediate (between 'bulk' and 'boundary') points with a distance from the boundary $r \sim L^\nu$, $0 < \nu < 1$; The wave function intensity at these points has a multifractal spectrum which interpolates between the bulk and the boundary spectra: $\tau_q^\nu = \tau_q^s + \nu(\tau_q^b - \tau_q^s)$. the corresponding contribution to the singularity spectrum of the whole sample is easily found to be $f(\alpha) = \nu f^b(\alpha_\pm^b) + (1 - \nu)f^s(\alpha_\pm^s)$ where $\nu = (\alpha - \alpha_\pm^s)(\alpha_\pm^b - \alpha_\pm^s)$.

Note that in this particular case the boundary effects modify $f(\alpha)$ in the whole range below $f(\alpha) \simeq 1$. Therefore, we arrive at the important result that the boundary exponents can affect the multifractal spectrum of the sample not only for rare realizations of disorder (governing the negative part of $f(\alpha)$) but also in a typical sample. This is in contrast to usual second-order phase transitions where boundary contribution is always less important than the bulk contribution to all observables.

2.3 Multifractality and field theory

The multifractal exponents describing the wave function moments can be related to the scaling dimensions of certain operators describing the local density of states and its moments in the field-theoretic description. One can understand this at the perturbative level using the non-linear sigma model description of disordered electronic

systems (for a review, see [17]).

Let us explain the connection here since this will be the basis for interpreting the numerical results discussed in later chapters. The local density of states (LDOS) at a particular energy E and at a specific point r_x in the sample can be written as:

$$\rho_E(r_x) = \sum_n |\psi_n(r_x)|^2 \delta(E - E_n), \qquad (2.13)$$

where n labels the energy eigenstates $\psi_n(r_x)$ at energy E_n. The global density of states (DOS) ρ_E is the integral of the LDOS over the whole sample. If we assume that all wave functions at a given E show statistically identical multifractal scaling behavior, we can then write,

$$|\psi_E(r_x)|^2 \sim \frac{\sum_n |\psi_n(r_x)|^2 \delta(E - E_n)}{\sum_n \delta(E - E_n)} = \frac{\rho_E(r_x)}{\rho_E}. \qquad (2.14)$$

Now disorder average of powers of the LDOS $\rho_E(r_x)$ are represented by the expectation value of operators in the corredponding field theory. We denote this symbolically as,

$$\overline{\left[L^d \rho_E(r_x)\right]^q} \sim \left\langle \mathcal{O}_q(r_x) \right\rangle, \qquad (2.15)$$

where the angular brackets denote the expectation value in the corresponding field theory. Here $\mathcal{O}_q(r_x)$ is the operator which corresponds to moments of $\left[L^d \rho_E(r_x)\right]$. This operator can be found explicitly in the sigma model description but we will not need that here.

In field theory, operators can be located in the bulk, on the boundary or at the corner of the sample (i.e. the point r_x can denote r_b, r_s or r_c respectively). At criticality, the expectation value of the corresponding operators exhibits a power-law

scaling:

$$\langle \mathcal{O}_q(r_x) \rangle \sim \frac{1}{L^{\mathrm{X}_q^x}}. \tag{2.16}$$

Here X_q^x is called the scaling dimension of the field theory operator $\mathcal{O}_q(r_x)$. (Unfortunately, due to convention, we use very similar notations X and x for the scaling dimension and in the location r_x of the operator respectively. The context should make it clear as to which one is being referred to.) In general, X_q^x is distinct for the $x = b, s$ and c cases as we will indeed see in later chapters.

Having introduced the scaling dimensions X_q^x, we can then relate it to the anomalous multifractal dimensions, Δ_q^x. There are two cases to consider: one when the global DOS, ρ_E is not critical at the LD transition and the other case when it is critical.

For the simple case when ρ_E is not critical, from Eqs. (2.3), (2.14), (2.15) and (2.16), we see that the scaling dimension X_q^x is the same as the anomalous multifractal dimension Δ_q^x and $\mu_x = 0$ for all the cases $x = b, s$ and c. The different multifractal exponents at the bulk, boundary and corners are just the bulk, boundary and corner scaling dimension of the corresponding operators in the field theory. This is summarized by the following relation for the case of non-critical DOS,

$$\overline{\left[L^d |\psi_{E_c}(r_x)|^2 \right]^q} \sim \langle \mathcal{O}_q(r_x) \rangle \sim \frac{1}{L^{\Delta_q^x}}, \tag{2.17}$$

where r_x is a point in the bulk, boundary or corner of the sample (i.e. $x = b, s$ or c).

For LD transitions where the density of states has a non-trivial critical scaling (this is the case with the SQH transition discussed later), the above identification between Δ_q^x and X_q^x has to be modified. In this case, the DOS ρ_E has a scaling

dimension X_ρ. Irrespective of the critical DOS, the wave function intensity is still normalized to unity over the whole sample. This implies that for points r_b which lie deep in the bulk of the sample, the operator corresponding to $L^d|\psi_{E_c}(r_b)|^2$ does not scale with the system size i.e. its dimension $\Delta_1^b = 0$. Using this in Eqs. (2.3), (2.14), (2.15) and (2.16), we see that,

$$\mathrm{X}_1^b = X_\rho \quad \text{and} \quad \mu_b = 0. \tag{2.18}$$

Using the same equations and adopting the convention that $\Delta_1^x \equiv 0$ for all $x = b, s$ and c, we arrive at the identifications,

$$\Delta_q^x = \mathrm{X}_q^x - q\mathrm{X}_1^x \quad \text{and} \quad \mu_x = \mathrm{X}_1^x - X_\rho. \tag{2.19}$$

Eqs. (2.18) and (2.19) are general relations that are valid for both critical and non-critical DOS cases and for all points ($x = b, s$ or c) in the sample. μ_x can be interpreted as an exponent expressing the supression of wave-function intensity near the boundaries or corners of a sample with critical DOS.

2.4 Conformal invariance at LD transitions

In the previous section, we outlined the general interpretation of multifractal scaling in terms of field theory operators. Here we specialize to the case of LD transitions occurring in two dimensions (2D) where we can say more.

The field theories describing phase transitions are in general, conformally invariant at the critical point. Conformal invariance can be thought of as local scale invariance. Conformal invariance is especially powerful in 2D where the corresponding symmetry becomes infinite dimensional and provides strong constraints on the various observ-

ables in the field theory (for reviews, see [18,19]). In particular, the ability to predict the value of observables in any sample geometry given the value of the observables in a single sample geometry is one of the important features of conformally invariant 2D systems. We will use this idea extensively in our analyses of LD transitions in 2D.

The disorder averaged field theories describing LD transitions are generally expected to be conformally invariant. Here we explain consequences of this conformal invariance for multifractal scaling. These consequences can be verified against numerical simulations (as we do in later chapters) which tests the hypothesis of conformal invariance at LD transitions. Even if we do not know the exact conformal field theory (CFT) describing an LD transition, numerical simulation of systems with boundaries can be used to glean important information about the unknown CFT. This is the motivation for some of the numerical analyses carried out for the symplectic-class and the IQH plateau transitions in Chapters 5 and 6, respectively.

Restricting ourselves to 2D, any conformal transformation can be represented by an analytic transformation $w(z)$ which maps a particular sample geometry parametrized by the complex co-ordinate z into a sample with different geometry parmetrized by w. (The complex conjugate $\bar{z}$ is mapped to $\bar{w}(\bar{z})$.) Specific examples of interest to us are the transformations,

1. $w(z) = \dfrac{L}{2\pi} \ln z$, which maps the full complex plane into an infinite cylinder of circumference L,

2. $w(z) = \dfrac{L}{\pi} \ln z$, which maps the upper half plane into an infinite strip of width L,

3. $w(z) = z^{\theta/\pi}$, which maps the upper half plane into a wedge with angle θ.

The last two transformations are shown in Fig. 2.2.
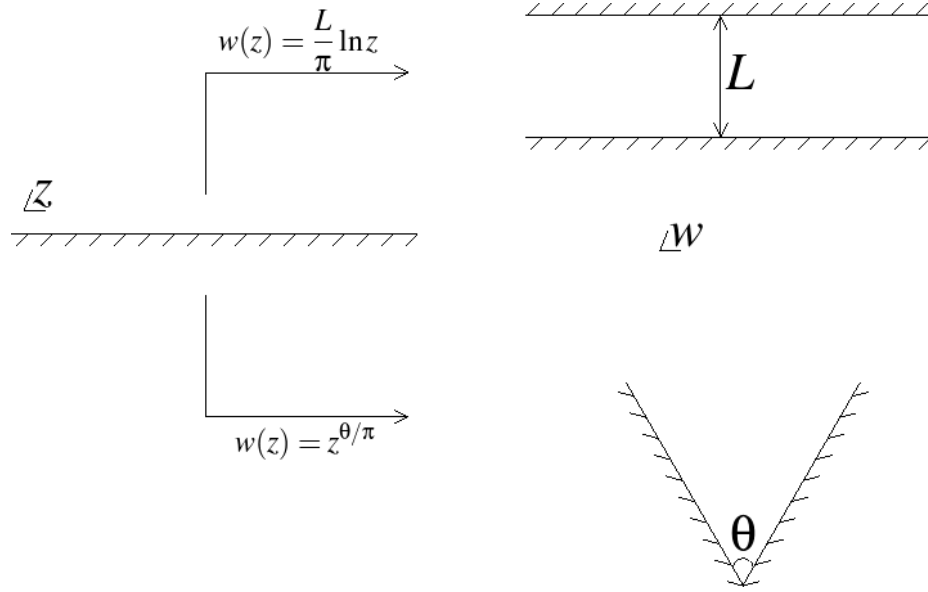
Figure 2.2: Conformal transformations mapping the upper half plane to a strip and to a wedge.

2D CFTs have a special class of operators called Virasoro primary fields that transform in a simple way under the above tranformations:

$$\phi(w) = \left|\frac{dw}{dz}\right|^{X_\phi} \phi(z). \tag{2.20}$$

X_ϕ is the scaling dimension of the Virasoro primary field ϕ. The primary field can be located either in the bulk or on the boundary of the 2D sample.

The two point correlation function of bulk fields in the full complex plane or the boundary fields on the upper half plane have a simple form in a conformally invariant field theory:

$$\langle \phi(z_1^x)\phi(z_2^x)\rangle = \frac{1}{\left|z_1^x - z_2^x\right|^{2X_\phi^x}}. \tag{2.21}$$

Here we have used the superscript x to denote that these could be either bulk $(x = b)$

fields in the full plane or boundary ($x = s$) fields in the upper half plane. In the later case, z_1 and z_2 will be real. Further, the one point function (expectation value) of the fields in any field theory (not necessarily a CFT) have the finite size scaling behavior,

$$\langle \phi(z^x) \rangle = \frac{1}{L^{X_\phi^x}}, \tag{2.22}$$

where L is the linear system size.

Using the transformation $w(z) = z^{\theta/\pi}$ in Eq. (2.20), Cardy pointed out [16] that a boundary primary field ϕ in the upper half plane with a scaling dimension X_ϕ^s has a modified scaling dimension $\pi X_\phi^s / \theta$ when it is located on the tip of a wedge of angle θ as can be seen from Eq. (2.21) and Eq. (2.22).

Again using the transformation $w(z) = \frac{L}{2\pi} \ln z$ in Eq. (2.20), it can be shown [20] that the two point correlation function of the bulk primary field $\phi(z^b)$ decays exponentially with a correlation length $\frac{L}{2\pi X_\phi^b}$ along the length of a cylinder of circumference L. A similar statement can be made [20] that the two point correlation function of the boundary primary field $\phi(z^s)$ decays exponentially with a correlation length $\frac{L}{\pi X_\phi^s}$ along the length of a strip of width L.

Now if we identify the operators corresponding to the wave function moments in Eq. (2.15) as Virasoro primaries, then the above mentioned transformations enable us to relate the mutifractal exponents in infinite and semi-infinite plane geometry to exponents in a wedge geometry and in the cylinder and strip geometry. Numerical verification of the relations below constitute stringent tests for conformal invariance at a 2D LD transition.

The half-plane to wedge transformation implies a relation between the boundary

and corner multifractal exponents as:

$$\Delta_q^\theta = \frac{\pi}{\theta}\Delta_q^s. \tag{2.23}$$

Here we have denoted the multifractal exponent at the tip of a wedge of angle θ as Δ_q^θ. We have to be careful in using this relation for all values of q. This is because the strict positivity bound on the Legendre transformed variable α mentioned in Sec. 2.2 will constrain the range of q over which the above relation is valid. We will discuss this in more detail in the Chapter 5 when we discuss numerical simulations of the 2D symplectic-class transition.

Next we use the mapping from the complex plane to the cylinder and from the upper half plane to the strip and relate the bulk and boundary multifractal exponents to the localization length on the cylinder and strip. Taking the limit $q \to 0$, we arrive at the relations,

$$\frac{\xi_p}{L} = \frac{1}{\alpha_0^b - 2}, \quad \text{and} \quad \frac{\xi_s}{L} = \frac{2}{\alpha_0^s - 2}. \tag{2.24}$$

Here ξ_c and ξ_s are the localization lengths of the wave function in the cylinder and strip geometry with L being the circumference of the cylinder or the width of the strip.

Chapter 3

Spin Quantum Hall Transition

3.1   Network model

The spin quantum Hall (SQH) transition was first studied, numerically, in Ref. [21]. A simple physical picture of the SQH effect was given in Ref. [22] and we direct the reader to this reference for a clear discussion of the basic physics of the SQH transition. Here we discuss the network model formulation of the SQH transition as explained in Refs. [21-23]. Network models have been very convenient for both numerical and analytical work on various disordered non-interacting fermion problems. The best known such model is the Chalker-Coddington network model [24] for the integer quantum Hall plateau transition.

Similar network models can be constructed for other localization problems, including the chiral metal [25,26], the random bond Ising model and the thermal quantum Hall effect [27-30].

The SQH network consists of a lattice of directed links and two types of nodes, A and B, forming a square lattice (see Fig. 3.1) on which spin-1/2 particles at energy $\epsilon = 0$ can propagate. Uni-directional propagation through each link is represented by a random SU(2) matrix. As in the case of Chalker-Coddington network, to study the critical behavior at the SQH transition it is sufficient to introduce disorder only for propagation along the links, while all the nodes can be taken to have the same (non-random) scattering matrices. The node scattering matrices are diagonal in the
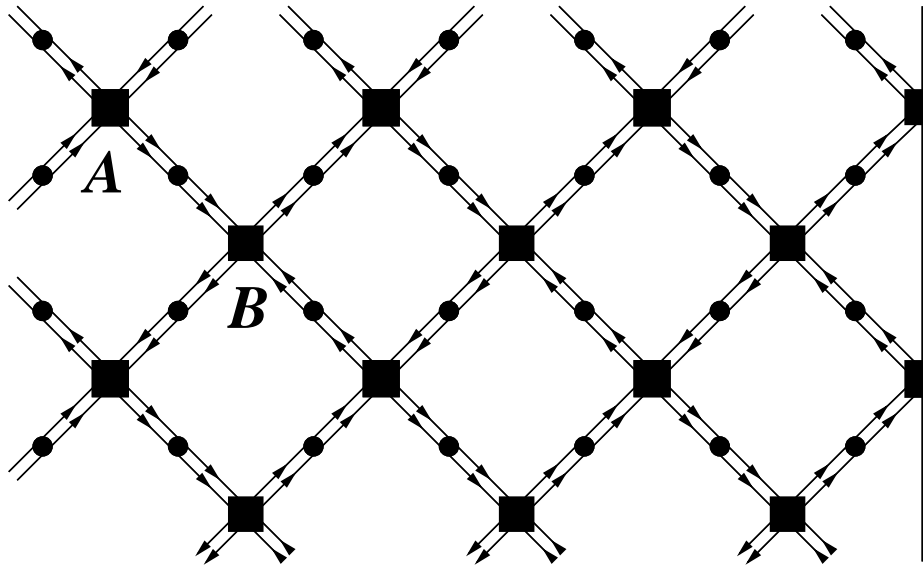
Figure 3.1: SQH network with a vertical reflecting boundary. The black squares represent the non-random node scattering matrices [Eq. (3.1)]. The black circles on the links represent the random SU(2) scattering matrices.

spin indices: $S_S = S_{S\uparrow} \otimes S_{S\downarrow}$,

$$S_{S\sigma} = \begin{pmatrix} (1 - t_{S\sigma}^2)^{1/2} & t_{S\sigma} \\ -t_{S\sigma} & (1 - t_{S\sigma}^2)^{1/2} \end{pmatrix}, \tag{3.1}$$

where $S = A, B$ labels whether the node is on the A or the B sublattice, and $\sigma = \uparrow, \downarrow$ labels the spin-index of the propagating particle. Apart from the case of boundary nodes (which will be treated in detail later), the remaining network is isotropic (invariant under 90 degree rotation of the lattice) when the scattering amplitudes on the two sublattice nodes are related by $t_{A\sigma}^2 + t_{B\sigma}^2 = 1$. The critical point of the isotropic network is located at $t_{A\sigma} = t_{B\sigma} = 1/\sqrt{2}$. Varying $t_{S\sigma}$ while keeping $t_{A\sigma}^2 + t_{B\sigma}^2 = 1$ and $t_{S\uparrow} = t_{S\downarrow}$ drives the system between a spin insulator and a SQH state and the spin Hall conductance jumps from 0 to 2. Taking $t_{S\uparrow} \neq t_{S\downarrow}$ breaks the global SU(2) symmetry and splits the transition into two ordinary IQH transitions each in the

unitary symmetry class (investigated, for example, in Ref. [24]). Here we consider only the spin-rotation invariant case with $t_{S\uparrow} = t_{S\downarrow} = t_S$.

3.2   Green's functions and symmetries

Network models can be studied using either a first quantized or a second quantized formalism. The first quantized method is adopted in Refs. [31-33]. It is also very useful for numerical work. Here we use it to derive certain symmetry relations. The rest of this chapter will employ the second quantized formalism (see next section).

All physical quantities of interest in the SQH problem such as wave function correlators and conductance can be expressed in terms of the Green's functions. Usually, the latter are represented in continuous time notation, but the network models use the discrete time analogs. In particular, network models use a single step time-evolution operator $\mathcal{U}$ which acts on the single particle wave function $\Psi(r, t)$ at discrete time t to give the wave function at time $t + 1$, where r denotes a link of the network. For a network with N links, $\mathcal{U}$ is a $2N \times 2N$ matrix (accounting for the spin-index), which represents a finite-time version of the infinitesimal time-evolution operator. Thus $\mathcal{U} = \exp\{i\mathcal{H}\}$ where the Hamiltonian $\mathcal{H}$ (which describes the time evolution of the edge states separating 'puddles' of topologically distinct regions) has the following symmetry property due to the spin rotation invariance in the problem [22],

$$\sigma_y \mathcal{H} \sigma_y = -\mathcal{H}^*, . \tag{3.2}$$

This implies that $\mathcal{U}$ is a (unitary) symplectic matrix and as such satisfies the condition

$$\mathcal{U}^{-1} = \sigma_y \mathcal{U}^T \sigma_y. \tag{3.3}$$

where σ_y is the conventional Pauli matrix acting on the 2 dimensional spin space. Now we can write the retarded [advanced] Green's function $G_R(r_1, r_2)$ $[G_A(r_1, r_2)]$ as the resolvent of the operator $\mathcal{U}$:

$$\left[G_R(r_1, r_2)\right]_{\alpha\beta} = \left\langle r_1, \alpha \left| \frac{1}{1 - z\mathcal{U}} \right| r_2, \beta \right\rangle, \tag{3.4}$$

$$\left[G_A(r_1, r_2)\right]_{\alpha\beta} = \left\langle r_1, \alpha \left| \frac{1}{1 - z^{-1}\mathcal{U}} \right| r_2, \beta \right\rangle. \tag{3.5}$$

Here $z = e^{i(\epsilon + i\gamma)}$ where ϵ is the energy and γ is a finite level broadening. Since the SQH transition of interest to us occurs only at zero energy, we will set $\epsilon = 0$ and hence $z = e^{-\gamma}$ from here on. In the above equation, (r_1, r_2) and (α, β) denote the network link and the spin index, respectively.

Making use of Eq. (3.3) in Eqs. (3.4, 3.5) leads to the following relationship between advanced and retarded Green's functions

$$\left[G_A(r_1, r_2)\right]_{\alpha'\alpha} - \delta_{\alpha'\alpha}\delta_{r_1, r_2} = \epsilon_{\alpha\beta}\left[G_R(r_2, r_1)\right]_{\beta\beta'}\epsilon_{\beta'\alpha'}, \tag{3.6}$$

where $\epsilon_{\alpha\beta}$ is the antisymmetric Levi-Civita tensor. The above equation will turn out to be crucial for our calculations since it implies that we need not introduce separate operators for the advanced sector Green's functions but can work solely with retarded ones (as we will see below).

3.3   Second-quantized description in the bulk

All network models can also be studied using the second-quantized supersymmetry (SUSY) technique [26,34,35].

The second-quantization of the SQH network is described in Ref. [23] and we review the main steps here. The basic idea is quite similar to the transfer matrix

formulation of various 2D statistical mechanics problems such as the Ising model (for a review, see Ref. [36]). The presence of disorder introduces a number of additional features which are sketched below.

All physical quantities in the network model including conductance, wave function amplitudes etc. may be expressed in first quantization in terms of sums over paths on the network. Such a sum may be written in second-quantized supersymmetric (SUSY) language as a correlation function, $\langle \ldots \rangle \equiv \text{STr}\left[\ldots (U_B U_A)^{L_T}\right]$ where the supertrace 'STr' contains the row-to-row transfer matrices U_A and U_B and the ellipsis $\ldots$ stands for operators that are inserted at the beginning and the ends of paths and correspond physically to density, current, etc. L_T is the number of A nodes (or B nodes) along the vertical direction, interpreted as discrete (imaginary) time. (The operator $(U_B U_A)^{L_T}$ was denoted by U in Ref. [23]). The supertrace STr implements periodic boundary condition along the vertical direction. Let there be L_X nodes in each row (the 'horizontal', or X direction). The operator U_A (resp. U_B) is formed by multiplying all the L_X transfer matrices at A (resp. B) nodes in a given row. These matrices act on a tensor product of bosonic and fermionic Fock spaces defined for each vertical column of links. The quantum state in the Fock spaces in each horizontal row of links should be thought of as resulting from the quantum state of the previous (in discrete imaginary time) row upon action of either U_A or U_B, within a single time step. The presence of a fermion or boson on a link represents an element of a path traversing that link [26,35]. Both bosons and fermions are needed to ensure the cancelation of contributions from closed loops (this ensures that $\text{STr}\,(U_B U_A)^{L_T} = 1$).

Usually one needs two types of bosons and fermions, 'retarded' and 'advanced', to be able to obtain two-particle properties (that is averages of products of retarded and advanced Green's functions) relevant for the calculation of transport properties. However, the symmetry relation in Eq. (3.6) relates retarded and advanced Green's

functions. Hence, as it turns out, for the computation of low enough moments of, say, retarded Green's functions, we need only one fermion and one boson per spin direction per link of a row. (This will be discussed in detail below.) We denote them by f_σ, b_σ for the links going up (up links), and $\bar{f}_\sigma$, $\bar{b}_\sigma$ for the down links. On the up links, f_σ, b_σ satisfy canonical fermion and boson commutation relations, respectively. But to ensure the cancelation of closed loops we must either take the fermions on the down links to satisfy $\{\bar{f}_\sigma, \bar{f}_{\sigma'}^\dagger\} = -\delta_{\sigma\sigma'}$ (while fermions on the up links and bosons on both types of links satisfy canonical commutation relations), or do the same for the bosons on down links instead of the fermions. Each node transfer matrix can be written in terms of these bosons and fermions. For any *given* disorder realization, this node transfer matrix turns out to commute with all the generators of the sl(2|1) superalgebra, as shown in Ref. [23] (see Appendix A for a summary of the relevant superalgebra representation theory). Performing the average over disorder (independently on each link) projects [23] the Fock space of bosons and fermions into the fundamental (dual-fundamental) 3 dimensional representation of sl(2|1) on up links (down links). These are precisely the states which are singlets under the random ('gauge') SU(2) on the links.

3.4 Network boundary

The extension of the above formalism to the case of a network with a reflecting boundary in the vertical direction is straightforward. Relegating some technical details to Appendix B, the reflecting boundary is seen to preserve the full sl(2|1) SUSY present in the bulk. Using the fully intact SUSY, one can then retain the mapping to the perimeters of percolation clusters (we refer to them as hulls henceforth) obtained in Ref. [23], but now the percolation hulls are confined to the half plane in two

dimensions with a reflecting boundary (see Fig. 3.1).

We will consider below correlation functions of operators in the network model in the vicinity of the SQH transition. When using continuum notation one needs to recall [37-39] that, in general, operators acquire additional singularities when approaching a boundary; they may vanish or diverge. By saying that points lie on the boundary, we imply that these points are not literally located *at* the boundary, but rather that the distance of the points from the boundary is much smaller than the distance of these points from each other, and much smaller than the system size. The same general reasoning will apply when we consider multifractality of wave functions at the boundary. Let us recall that in the literature of surface transitions in ordinary magnets, various kinds of cases which are often referred to as 'ordinary', 'extraordinary' and 'special' boundary transitions are discussed, referring to the respective ordering of bulk and boundary. The case of the reflecting boundary condition that we consider here is analogous to the so-called ordinary surface transition where the boundary and the bulk undergo the LD transition simultaneously.

We will need the bulk and boundary scaling dimension of the field theory operator corresponding to a single percolation hull (the '1-hull' operator) in various calculations below. This has been derived using a variety of techniques in the literature [16, 40, 41] and is found to be $x_s = 1/3$ for the boundary 1-hull operator. The corresponding bulk operator has scaling dimension $x_b = 1/4$.

3.5 Multifractality using supersymmetry

3.5.1 Wave function correlators

We have defined multifractal exponents in terms of moments of wave function at a single point in the sample (see Chapter 2). In field theory, for calculating the

multifractal exponent Δ_q^x, (restricting q to be an integer,) it is easier to find the scaling of correlation function of q operators, each corresponding to the wave function intensity $L^2|\psi(r)|^2$. The q-point correlations of critical eigenfunction intensities take on a convenient scaling form when the distances between all points are equal to the same scale r, that is, $|r_i - r_j| \sim r$. In this case, it follows from the discussion in Sec. 2.3 that

$$L^{q(d+\mu_x)}\overline{|\psi(r_1)\psi(r_2)\ldots\psi(r_q)|^2} \sim \left(\frac{r}{L}\right)^{\Delta_q^x}, \tag{3.7}$$

where L is the linear system size. The location of the operators can be in the bulk, boundary or in a corner of the sample. The above equation is easily related to the equations in Sec. 2.3 by considering the limit when r is of the scale of lattice spacing, i.e. when all operators essentially lie at the same point and can be considered as a single operator corresponding to the quantity $L^2|\psi(r)|^2$ raised to power q.

Off criticality (that is, for $\epsilon \neq 0$ or $\gamma > 0$ in the SQH system), multifractal scaling behavior holds on length scales much shorter than the localization length [23] $\xi_\gamma \sim \gamma^{-4/7}$, beyond which the wave function amplitudes are exponentially small [32,33]. This implies that off criticality, the above q-point correlator should be written as

$$L^{q(d+\mu_x)}\overline{|\psi(r_1)\psi(r_2)\ldots\psi(r_q)|^2} \sim \left(\frac{r}{\xi_\gamma}\right)^{\Delta_q^x}, \qquad r \ll \xi_\gamma. \tag{3.8}$$

Assuming that all wave functions at a given energy show statistically identical mul-

tifractal scaling behavior, one can write the above correlator as

$$L^{q(d+\mu_x)}\overline{|\psi(r_1)\psi(r_2)\dots\psi(r_q)|^2} \tag{3.9}$$

$$= \frac{\sum_{i_1,i_2\dots i_q}\overline{|\psi_{i_1}(r_1)\psi_{i_2}(r_2)\dots\psi_{i_q}(r_q)|^2\delta(\epsilon_1-\epsilon_{i_1})\delta(\epsilon_2-\epsilon_{i_2})\dots\delta(\epsilon_q-\epsilon_{i_q})}}{\overline{\rho(\epsilon_1)}\,\overline{\rho(\epsilon_2)}\dots\overline{\rho(\epsilon_q)}}, \tag{3.10}$$

where $i_1, i_2 \dots i_q$ are additional quantum numbers required, besides position r, to label the wave function (energy and spin in the SQH case). ρ represents the global density of states. The above line is similar to what we did in Sec. 2.3 to relate the wave function moments to field theory operators. Taking $\epsilon_1, \epsilon_2 \dots \epsilon_q \sim \epsilon$ and $|r_i - r_j| \sim r$, we see that the exponent Δ_q^x is given by the scaling behavior of $\tilde{\mathcal{D}}_q^x(r_1, r_2 \dots r_q; \epsilon)$ with respect to r, where the function $\tilde{\mathcal{D}}_q^x$ is defined by

$$\tilde{\mathcal{D}}_q^x(r_1, r_2 \dots r_q; \epsilon) = \sum_{i_1,i_2\dots i_q}\overline{|\psi_{i_1}(r_1)\psi_{i_2}(r_2)\dots\psi_{i_q}(r_q)|^2\delta(\epsilon-\epsilon_{i_1})\delta(\epsilon-\epsilon_{i_2})\dots\delta(\epsilon-\epsilon_{i_q})}.$$

$$\tag{3.11}$$

We understand that the points $r_1 \dots r_q$ are all chosen to lie in the region $\mathcal{M}_x$ considered in Eq. (2.2).

Using the Green's functions defined in Sec. 3.2, we can write the above wave function correlator (ignoring overall factors of $(2\pi)^{-q}$) as

$$\tilde{\mathcal{D}}_q^x(r_1, r_2 \dots r_q; z) \propto \overline{\prod_{k=1}^{q} \mathrm{tr}\left[G_R(r_k, r_k) - G_A(r_k, r_k)\right]}. \tag{3.12}$$

Here 'tr' denotes the trace over the spin indices. As was discussed in Ref. [32], the

multifractal exponents can also be obtained from a different Green's function product,

$$\mathcal{D}_x^q(r_1, r_2 \ldots r_q; z) \propto \overline{\text{tr} \prod_{k=1}^{q} [G_R(r_k, r_{k+1}) - G_A(r_k, r_{k+1})]}, \qquad (3.13)$$

where $r_{q+1} \equiv r_1$. When $|r_i - r_j| \sim r$, this product shows the same scaling behavior, $r^{\Delta_q^x}$ as the previous one. Since the calculations of both functions $\tilde{\mathcal{D}}$ and $\mathcal{D}$ are very similar, we have explained in detail only the calculation of $\tilde{\mathcal{D}}$. By suitably choosing the correct SU(2) invariant (see next section), we will extract below the scaling of $\tilde{\mathcal{D}}$. Our results agree with those previously obtained in Ref. [32] for the *bulk* case, $x = b$, but we obtain these results using a different method (namely that developed in Ref. [23], using supersymmetry). For the other cases, $x = s$ (boundary) and $x = c$ (corner), our results are entirely new.

3.5.2   Calculation of Δ_2

We start with the calculation of the exponent Δ_q^x for the case $q = 2$. The corresponding Green's function product that we have to evaluate is (dependence on $z =$ $= \exp(-\gamma)$, defined in Eqs (3.4, 3.5), is understood)

$$\tilde{\mathcal{D}}_2^x(r_1, r_2) \propto \overline{\text{tr} \left[G_R(r_1, r_1) - G_A(r_1, r_1) \right] \text{tr} \left[G_R(r_2, r_2) - G_A(r_2, r_2) \right]}. \qquad (3.14)$$

Using Eq. (3.6), we can write the above relation in terms of retarded functions alone as

$$\tilde{\mathcal{D}}_2^x(r_1, r_2) \propto \overline{\text{tr} \left[G_R(r_1, r_1) - 1 \right] \text{tr} \left[G_R(r_2, r_2) - 1 \right]}$$
$$= \overline{\text{tr}\, G_R(r_1, r_1) \text{tr}\, G_R(r_2, r_2)} - \overline{\text{tr}\, G_R(r_1, r_1)} - \overline{\text{tr}\, G_R(r_2, r_2)} + 1. \quad (3.15)$$

We will use the supersymmetry technique [26,34,35] to implement the disorder average and express [23] all averaged Green's functions using the second quantized formalism in terms of generators of the sl(2|1) Lie superalgebra. (A summary of certain basic elements of the relevant representation theory of the sl(2|1) superalgebra is presented in Appendix A.)

The retarded Green's functions can be expressed as expectation values of canonical boson and fermion operators. (From here on, all Green's functions are understood as retarded unless they have an explicit subscript A). Specifically, we can write the following Green's functions, in any fixed realization of disorder, as (the subscripts below refer to both, the spatial coordinate and the spin index)

$$G_{ij} = \text{STr}\big[b_i b_j^\dagger (U_B U_A)^{L_T}\big] = \langle b_i b_j^\dagger \rangle, \tag{3.16}$$

$$G_{kn} = \text{STr}\big[f_k f_n^\dagger (U_B U_A)^{L_T}\big] = \langle f_k f_n^\dagger \rangle, \tag{3.17}$$

$$G_{ij} G_{kn} = \text{STr}\big[b_i b_j^\dagger f_k f_n^\dagger (U_B U_A)^{L_T}\big] = \langle b_i b_j^\dagger f_k f_n^\dagger \rangle. \tag{3.18}$$

(Here, the fact that $\text{STr}\,(U_B U_A)^{L_T} = 1$ was used.) Let us take $i \to (r_1, \alpha_1), j \to (r_1, \beta_1), k \to (r_2, \alpha_2)$, and $n \to (r_2, \beta_2)$ in the above equations. The LHS of the last equation thus reads $G_{\beta_1}^{\alpha_1}(r_1, r_1) G_{\beta_2}^{\alpha_2}(r_2, r_2)$. After performing the disorder average, only SU(2) singlet combinations are non-vanishing. Hence we contract both sides with the SU(2) invariant $\delta_{\beta_1}^{\alpha_1} \delta_{\beta_2}^{\alpha_2}$ giving LHS $= \overline{\text{tr}\,G(r_1, r_1)\,\text{tr}\,G(r_2, r_2)}$. The RHS of Eq. (3.18) is (we can raise and lower indices trivially since the metric is the unit matrix)

$$\text{RHS} = \delta_{\beta_1}^{\alpha_1} \delta_{\beta_2}^{\alpha_2} \langle b_{\alpha_1}(r_1) b_{\beta_1}^\dagger(r_1) f_{\alpha_2}(r_2) f_{\beta_2}^\dagger(r_2) \rangle = \big\langle \big(2B(r_1) + 1\big)\big(1 - 2Q_3(r_2)\big) \big\rangle.$$

(The expressions for the generators B and Q_3 of the Lie superalgebra, as reviewed in

Appendix A, were used.) Thus the LHS and RHS together imply:

$$\overline{\operatorname{tr} G(r_1, r_1) \operatorname{tr} G(r_2, r_2)} = \left\langle \left(2B(r_1) + 1 \right) \left(1 - 2Q_3(r_2) \right) \right\rangle. \tag{3.19}$$

Similarly, considering Eq. (3.17), let $k \to (r_2, \alpha_2)$ and $n \to (r_2, \beta_2)$ giving LHS $= G_{\beta_2}^{\alpha_2}(r_2, r_2)$. To do disorder average, contract with the SU(2) invariant $\delta_{\alpha_2}^{\beta_2}$, giving LHS $= \overline{\operatorname{tr} G(r_2, r_2)}$. The RHS of Eq. (3.17) gives

$$\text{RHS} = \delta_{\alpha_2}^{\beta_2} \langle f_{\alpha_2}(r_2) f_{\beta_2}^\dagger(r_2) \rangle = \left\langle 1 - 2Q_3(r_2) \right\rangle. \tag{3.20}$$

Hence from LHS and RHS, we obtain

$$\overline{\operatorname{tr} G(r_2, r_2)} = \left\langle 1 - 2Q_3(r_2) \right\rangle. \tag{3.21}$$

Now using Eqs. (3.19) and (3.21), we can write Eq. (3.15) as

$$\tilde{\mathcal{D}}_2^x(r_1, r_2) \propto -\left\langle B(r_1) Q_3(r_2) \right\rangle. \tag{3.22}$$

We will now compute this correlator off criticality, at a finite correlation length ξ_γ, arising from a non-vanishing 'broadening' $\gamma > 0$, that is $z = \exp(-\gamma) < 1$.

The angular brackets in Eq. (3.22) denote the supertrace 'STr' taken over the *full* Fock space of canonical bosons and fermions on each link of the network before disorder averaging. As explained in Ref. [23], the disorder average projects this Fock space into the fundamental three-dimensional representation of sl(2|1) on the up links and the corresponding dual representation on the down links. To sum only over the three states in this representation, we use the notation 'str' (see Eq. (3.23)). We note that the state with odd fermion number in both of these representations

has negative norm [23]. The prefix 's' in str denotes the fact that these negative norm states contribute to the trace with a negative sign. This is essential to get the correct overall factor of unity for each loop traversed [23]. The action of the node transfer matrix, $T_{S\sigma}$, on the tensor product of the disorder-averaged states on an up link and a neighboring down link can be represented by a linear combination of the only two sl(2|1) invariant operators in this 3×3 dimensional vector space. These are the identity operator and the projection operator onto the singlet state, with weights $1 - t_{S\sigma}^2$ and $t_{S\sigma}^2$ respectively. These weights can be considered as the classical probability of a state turning left or right at a given node under the action of the node transfer matrix. When we multiply all such node transfer matrices together, the partition function can be represented as a sum over all classical configurations of densely packed loops (the closed classical paths along which the disorder averaged states propagate) on a square lattice. Each loop gets an overall weight which is the product of the probabilities of turning in a particular direction at each node. The loops can be interpreted (see Ref. [23] for a diagrammatic perspective) as the external perimeters of a cluster percolating along the bonds of a square lattice. This completes the mapping to percolation identified in Ref. [23].

Now, in order to evaluate a disorder averaged correlator such as the one in Eq. (3.22), consider the three-dimensional representation on the links (for example, the case where r_1 and r_2 lie on up links) and all calculations are done in this representation. A loop passing through a link corresponds to all three states in the three-dimensional sl(2|1) representation propagating on that link. Away from criticality, we assign a factor of $z^{2(B+Q_3)}$ for each such link since the operator $2(B+Q_3)$ counts the number of states propagating on that link. The product of these factors along a path on the network gives the same power of z that occurs in the Taylor expansion of a matrix element of the Green's function in Eq. (3.4). After multiplying such factors

for all links through which a given loop passes, we also multiply it with the overall weight coming from the classical probability of the loop turning at each node as mentioned in the previous paragraph. Further, if there are operators inserted at specific points on the lattice, the only loops contributing to the correlation function are those which are constrained to pass through these points. Considering the correlator in Eq. (3.22), there are two different kinds of loop configurations which contribute: (1) a single loop passes through both points r_1 and r_2, (2) two different loops pass through each of these two points, r_1 and r_2. These two terms are the probabilistic versions of the usual connected and disconnected parts of any correlation function. Writing the contribution for each of these types separately and summing over all possible loop configurations together with their respective weights, we write Eq. (3.22) as

$$
4\langle B(r_1)Q_3(r_2)\rangle
$$

$$
= \sum_{N_{12},N_{21}} \text{str} \begin{pmatrix} 1 & 0 & 0 \\ 0 & 2 & 0 \\ 0 & 0 & 1 \end{pmatrix} \begin{pmatrix} 1 & 0 & 0 \\ 0 & z^{2N_{12}} & 0 \\ 0 & 0 & z^{2N_{12}} \end{pmatrix} \begin{pmatrix} -1 & 0 & 0 \\ 0 & 0 & 0 \\ 0 & 0 & 1 \end{pmatrix} \begin{pmatrix} 1 & 0 & 0 \\ 0 & z^{2N_{21}} & 0 \\ 0 & 0 & z^{2N_{21}} \end{pmatrix}
$$

$$
\times P(r_1, r_2; N_{12}, N_{21})
$$

$$
+ \sum_{N,N'} \text{str} \begin{pmatrix} 1 & 0 & 0 \\ 0 & 2 & 0 \\ 0 & 0 & 1 \end{pmatrix} \begin{pmatrix} 1 & 0 & 0 \\ 0 & z^{2N} & 0 \\ 0 & 0 & z^{2N} \end{pmatrix} \text{str} \begin{pmatrix} -1 & 0 & 0 \\ 0 & 0 & 0 \\ 0 & 0 & 1 \end{pmatrix} \begin{pmatrix} 1 & 0 & 0 \\ 0 & z^{2N'} & 0 \\ 0 & 0 & z^{2N'} \end{pmatrix}
$$

$$
\times P_-(r_1, r_2; N, N')
$$

$$
= -\sum_{N} \left[1 - z^{2N}\right] P(r_1, r_2; N) - \sum_{N,N'} \left[1 - z^{2N}\right]\left[1 - z^{2N'}\right] P_-(r_1, r_2; N, N'),
$$

$$
(3.23)
$$

where $P(r_1, r_2; N)$ is the probability of a single loop of length N passing through both r_1 and r_2, and $P_-(r_1, r_2; N, N')$ is the probability that in a given percolation

configuration the points r_1 and r_2 belong to two different, non-overlapping loops of lengths N and N', respectively. In the above equation, the probability factor $P(r_1, r_2; N_{12}, N_{21})$ is for a path of length N_{12} going from r_1 to r_2 and then a path of length N_{21} returning from r_2 to r_1. In the next line, we simplified this using the fact that this is the same as a loop of overall length, $N = N_{12} + N_{21}$ passing through both the points, and setting $P(r_1, r_2; N) := P(r_1, r_2; N_{12}, N_{21})$. The appearance of these classical percolation probabilities in the above formula arises from the product of the individual factors for turning left or right at each node of the network model. Thus, using Eq. (3.23), we can write Eq. (3.22) as:

$$\tilde{\mathcal{D}}_2^x(r_1, r_2) \propto \sum_N \left[1 - z^{2N}\right] P(r_1, r_2; N)$$
$$+ \sum_{N, N'} \left[1 - z^{2N}\right]\left[1 - z^{2N'}\right] P_-(r_1, r_2; N, N'). \qquad (3.24)$$

We see that the leading order terms turn out to vanish in the critical limit $z \to 1$, as observed in Ref. [32]. So we need to consider the sub-leading behavior. The percolation probabilities discussed above are the Laplace transformed versions of the correlation functions of 1-hull operators in percolation. The 1-hull operator represents the density-of-states operator in the SQH problem [23]. We know the scaling dimension of these operators as mentioned in the last paragraph in Sec. 3.4. Under the Laplace transform, the variable N is the conjugate of the energy $\epsilon + i\gamma \equiv -i \ln z$ which is represented by the 1-hull operator. Now, using the scaling dimensions of the 1-hull operator to deduce the scaling of the Laplace transformed correlation functions (see, for example, Ref. [42]), one finds the following leading scaling behavior of the

above-mentioned probabilities:

$$P(r_1, r_2; N) \sim N^{-2/(2-x_b)} r^{-x_b} \quad \sim N^{-8/7} r^{-1/4}, \tag{3.25}$$

$$P_-(r_1, r_2; N, N') \sim P(r_1; N) P(r_2; N') \sim N^{-8/7} N'^{-8/7}, \tag{3.26}$$

where $P(r_1; N)$ is the probability that the point r_1 belongs to a loop of length N. The points r_1 and r_2 lie in the bulk and $r = |r_1 - r_2| \ll \xi_\gamma \sim \gamma^{-4/7} \sim N^{4/7}$. Similarly, the scaling expressions in the case where both points lie on the boundary are

$$P(r_1, r_2; N) \sim N^{-1-x_s/(2-x_b)} r^{-x_s} \sim N^{-25/21} r^{-1/3}, \tag{3.27}$$

$$P_-(r_1, r_2; N, N') \sim P(r_1; N) P(r_2; N') \quad \sim N^{-25/21} N'^{-25/21}. \tag{3.28}$$

We see that only the first term in Eq. (3.24) (which is the connected part) gives rise to the non-analytic r dependence in the limit $r \ll \xi_\gamma$, which we are interested in computing. Hence the scaling of $\tilde{\mathcal{D}}_2^x(r_1, r_2)$ is given by:

$$\tilde{\mathcal{D}}_2^x(r_1, r_2) \sim \sum_N \left[1 - e^{-2N\gamma}\right] P(r_1, r_2; N) \quad \sim \begin{cases} r^{-1/4} \text{ (bulk)}, \\ r^{-1/3} \text{ (boundary)}. \end{cases} \tag{3.29}$$

Thus, upon comparison with Eq. (3.8), we finally read off the multifractal exponent for $q = 2$ as being $\Delta_2^b = -1/4$ for the bulk, and $\Delta_2^s = -1/3$ for the boundary. We will discuss the case of the wave function scaling behavior at corners at the end (see Sec. 3.7) as it is a straightforward extension of the boundary case upon making use of conformal invariance. In the next subsection, we consider the more interesting exponent describing the scaling of the third moment of the square of the wave function amplitudes.

3.5.3   Calculation of Δ_3

The algebraic procedure for calculating the multifractal exponent Δ_q for $q = 3$ is almost same as that we used above for $q = 2$. Hence we present only the important steps and focus on the main results and the interesting differences. We start with the expression:

$$\tilde{\mathcal{D}}_3^x(r_1, r_2, r_3) \propto \overline{\mathrm{tr}\,[G_R(r_1, r_1) - G_A(r_1, r_1)]}$$
$$\times \overline{\mathrm{tr}\,[G_R(r_2, r_2) - G_A(r_2, r_2)]\,\mathrm{tr}\,[G_R(r_3, r_3) - G_A(r_3, r_3)]}. \quad (3.30)$$

Converting all advanced Green's functions to retarded ones using Eq. (3.6), we can write the above equation as:

$$\tilde{\mathcal{D}}_3^x(r_1, r_2, r_3) \propto \overline{\mathrm{tr}\,[G(r_1, r_1) - 1]\,\mathrm{tr}\,[G(r_2, r_2) - 1]\,\mathrm{tr}\,[G(r_3, r_3) - 1]}$$
$$= \overline{\mathrm{tr}\,G(r_1, r_1)\,\mathrm{tr}\,G(r_2, r_2)\,\mathrm{tr}\,G(r_3, r_3)} - 1$$
$$- \sum_{[r_1, r_2, r_3]} \overline{\mathrm{tr}\,G(r_1, r_1)\,\mathrm{tr}\,G(r_2, r_2)} + \sum_{[r_1, r_2, r_3]} \overline{\mathrm{tr}\,G(r_1, r_1)}, \quad (3.31)$$

where $\sum_{[r_1, r_2, r_3]}$ denotes sum over terms with all cyclic permutations of (r_1, r_2, r_3).

The new piece we have to evaluate here is the product of three Green's functions. For this consider the following two identities, obtained by applying Wick's theorem, and valid in any fixed realization of disorder:

$$\left[G_{ij} G_{lm} + G_{im} G_{lj}\right] G_{kn} = \langle b_i b_j^\dagger b_l b_m^\dagger f_k f_n^\dagger \rangle. \quad (3.32)$$

Exchanging bosons and fermions in the above equation, we find

$$\left[G_{ij} G_{lm} - G_{im} G_{lj}\right] G_{kn} = \langle f_i f_j^\dagger f_l f_m^\dagger b_k b_n^\dagger \rangle. \quad (3.33)$$

In Eq. (3.32), let $i \to (r_1, \alpha_1)$, $j \to (r_1, \beta_1)$, $l \to (r_2, \alpha_2)$, $m \to (r_2, \beta_2)$, $k \to (r_3, \alpha_3)$, $n \to (r_3, \beta_3)$, yielding

$$\text{LHS} = [G^{\alpha_1}_{\beta_1}(r_1, r_1) G^{\alpha_2}_{\beta_2}(r_2, r_2) + G^{\alpha_1}_{\beta_2}(r_1, r_2) G^{\alpha_2}_{\beta_1}(r_2, r_1)] G^{\alpha_3}_{\beta_3}(r_3, r_3). \qquad (3.34)$$

As above, it is convenient to contract with the SU(2) invariant $\delta^{\beta_1}_{\alpha_1} \delta^{\beta_2}_{\alpha_2} \delta^{\beta_3}_{\alpha_3}$, after performing the disorder average

$$\overline{\text{tr}\, G(r_1, r_1) \,\text{tr}\, G(r_2, r_2) \,\text{tr}\, G(r_3, r_3)} + \overline{\text{tr}\, G(r_3, r_3) \,\text{tr}\, [G(r_1, r_2) G(r_2, r_1)]}$$
$$= \langle b_\alpha(r_1) b_\alpha^\dagger(r_1) b_\beta(r_2) b_\beta^\dagger(r_2) f_\gamma(r_3) f_\gamma^\dagger(r_3) \rangle$$
$$= \big\langle\, [1 + 2B(r_1)]\, [1 + 2B(r_2)]\, [1 - 2Q_3(r_3)]\, \big\rangle. \qquad (3.35)$$

We see that the first term on the LHS of Eq. (3.35) is the Green's function product we want to evaluate in Eq. (3.31), while the second term has to be eliminated. This can be achieved by performing steps, analogous to those above, in Eq. (3.33), yielding

$$\overline{\text{tr}\, G(r_1, r_1) \,\text{tr}\, G(r_2, r_2) \,\text{tr}\, G(r_3, r_3)} - \overline{\text{tr}\, G(r_3, r_3) \,\text{tr}\, [G(r_1, r_2) G(r_2, r_1)]}$$
$$= \langle f_\alpha(r_1) f_\alpha^\dagger(r_1) f_\beta(r_2) f_\beta^\dagger(r_2) b_\gamma(r_3) b_\gamma^\dagger(r_3) \rangle$$
$$= \big\langle\, [1 - 2Q_3(r_1)]\, [1 - 2Q_3(r_2)]\, [1 + 2B(r_3)]\, \big\rangle. \qquad (3.36)$$

Adding Eqs. (3.35) and (3.36), we obtain

$$2\,\overline{\text{tr}\, G(r_1, r_1) \,\text{tr}\, G(r_2, r_2) \,\text{tr}\, G(r_3, r_3)} = \big\langle\, [1 + 2B(r_1)]\, [1 + 2B(r_2)]\, [1 - 2Q_3(r_3)]$$
$$+ [1 - 2Q_3(r_1)]\, [1 - 2Q_3(r_2)]\, [1 + 2B(r_3)]\, \big\rangle. $$
$$(3.37)$$

We can now use Eqs. (3.19), (3.21), and (3.37) to write Eq. (3.31) as

$$\tilde{\mathcal{D}}_3^x(r_1, r_2, r_3) \propto \Big\langle \left[1 + 2B(r_1)\right]\left[1 + 2B(r_2)\right]\left[1 - 2Q_3(r_3)\right]$$

$$+ \left[1 - 2Q_3(r_1)\right]\left[1 - 2Q_3(r_2)\right]\left[1 + 2B(r_3)\right] \Big\rangle + \sum_{[r_1, r_2, r_3]} \Big\langle 1 + 2B(r_1)\Big\rangle$$

$$- \sum_{[r_1, r_2, r_3]} \Big\langle \left[1 - 2Q_3(r_1)\right]\left[1 + 2B(r_2)\right] \Big\rangle - 1. \tag{3.38}$$

Converting these expressions to percolation probabilities is exactly analogous to the two point case. Taking the critical limit $z \to 1$, we obtain

$$\tilde{\mathcal{D}}_3^x(r_1, r_2, r_3) \propto P(r_1, r_2, r_3) + P(r_1, r_3, r_2). \tag{3.39}$$

where $P(r_1, r_2, r_3)$ is the probability of a loop of any size traversing r_1, r_2, r_3 in that order. There is no cancelation to leading order at criticality here, unlike the two point case. The final scaling of this correlator is simply given by that of the usual 3-point correlation function of percolation 1-hull operators at criticality,

$$P(r_1, r_2, r_3), P(r_1, r_3, r_2) \sim \begin{cases} r^{-3x_b} \sim r^{-3/4} \text{ (bulk)}, \\ r^{-3x_s} \sim r^{-1} \text{ (boundary)}. \end{cases} \tag{3.40}$$

Hence the value of multifractal exponent for $q = 3$ is $\Delta_3^b = -3/4$ and $\Delta_3^s = -1$, for bulk and boundary, respectively.

3.5.4   Higher multifractal exponents

The procedure for calculating Δ_3^x was very similar to that of Δ_2^x (albeit more tedious) and one might ask if it can be extended to higher multifractal exponents, Δ_q^x with

$q > 3$. On the other hand however, the fact that we are able to calculate Δ_3^x at all using our formalism is conceptually surprising because usually in supersymmetric problems, an additional set (='replica') of boson and fermion operators is required for each additional Green's function factor entering the product in Eq. (3.12). Here we are able to calculate both two and three-point functions with the same number of boson and fermion operators (replicas).

To understand this, we look at the calculation of Δ_3 carefully. We had an extra 'unwanted' Green's function product in Eq. (3.35). But we were able to eliminate it by using an equation similar to Eq. (3.36), with bosons and fermions exchanged. The unwanted Green's function product canceled between Eq. (3.35) and Eq. (3.36) when added together, giving us the exact product that we wanted.

Now does such a cancelation go through for higher point functions? To answer this, we look at the next higher exponent, Δ_4^x. Here we will have to evaluate a product of four Green's functions,

$$\overline{\operatorname{tr} G(r_1, r_1) \operatorname{tr} G(r_2, r_2) \operatorname{tr} G(r_3, r_3) \operatorname{tr} G(r_4, r_4)}.$$

To evaluate this, we will have to use the following identity obtained from Wick's theorem (in a fixed realization of disorder):

$$\left[G_{ij}G_{lm} - G_{im}G_{lj}\right]\left[G_{pq}G_{rs} + G_{ps}G_{rq}\right] = \langle f_i f_j^\dagger f_l f_m^\dagger b_p b_q^\dagger b_r b_s^\dagger \rangle. \tag{3.41}$$

In this equation, let again $i \to (r_1, \alpha_1)$, $j \to (r_1, \beta_1)$, $l \to (r_2, \alpha_2)$, $m \to (r_2, \beta_2)$, $p \to (r_3, \alpha_3)$, $q \to (r_3, \beta_3)$, $r \to (r_4, \alpha_4)$, $s \to (r_4, \beta_4)$. Then contracting with the

SU(2) invariant $\delta^{\beta_1}_{\alpha_1}\delta^{\beta_2}_{\alpha_2}\delta^{\beta_3}_{\alpha_3}\delta^{\beta_4}_{\alpha_4}$ gives us upon averaging the relation:

$$\overline{\operatorname{tr} G(r_1,r_1)\operatorname{tr} G(r_2,r_2)\operatorname{tr} G(r_3,r_3)\operatorname{tr} G(r_4,r_4)}$$

$$+ \overline{\operatorname{tr} G(r_1,r_1)\operatorname{tr} G(r_2,r_2)\operatorname{tr} [G(r_3,r_4)G(r_4,r_3)]}$$

$$- \overline{\operatorname{tr} [G(r_1,r_2)G(r_2,r_1)]\operatorname{tr} G(r_3,r_3)\operatorname{tr} G(r_4,r_4)}$$

$$- \overline{\operatorname{tr} [G(r_1,r_2)G(r_2,r_1)]\operatorname{tr} [G(r_3,r_4)G(r_4,r_3)]}$$

$$= \big\langle\, [1-2Q_3(r_1)]\,[1-2Q_3(r_2)]\,[1+2B(r_3)]\,[1+2B(r_4)]\,\big\rangle. \qquad (3.42)$$

There are three unwanted terms on the LHS. Exchanging bosons and fermions gives on the other hand:

$$\overline{\operatorname{tr} G(r_1,r_1)\operatorname{tr} G(r_2,r_2)\operatorname{tr} G(r_3,r_3)\operatorname{tr} G(r_4,r_4)}$$

$$- \overline{\operatorname{tr} G(r_1,r_1)\operatorname{tr} G(r_2,r_2)\operatorname{tr} [G(r_3,r_4)G(r_4,r_3)]}$$

$$+ \overline{\operatorname{tr} [G(r_1,r_2)G(r_2,r_1)]\operatorname{tr} G(r_3,r_3)\operatorname{tr} G(r_4,r_4)}$$

$$- \overline{\operatorname{tr} [G(r_1,r_2)G(r_2,r_1)]\operatorname{tr} [G(r_3,r_4)G(r_4,r_3)]}$$

$$= \big\langle\, [1-2Q_3(r_3)]\,[1-2Q_3(r_4)]\,[1+2B(r_1)]\,[1+2B(r_2)]\,\big\rangle. \qquad (3.43)$$

Adding Eq. (3.42) and Eq. (3.43) eliminates two unwanted pieces:

$$2\,\overline{\operatorname{tr} G(r_1,r_1)\operatorname{tr} G(r_2,r_2)\operatorname{tr} G(r_3,r_3)\operatorname{tr} G(r_4,r_4)}$$

$$- 2\,\overline{\operatorname{tr} [G(r_1,r_2)G(r_2,r_1)]\operatorname{tr} [G(r_3,r_4)G(r_4,r_3)]}$$

$$= \big\langle\, [1+2B(r_1)]\,[1+2B(r_2)]\,[1-2Q_3(r_3)]\,[1-2Q_3(r_4)]\,\big\rangle +$$

$$\big\langle\, [1-2Q_3(r_1)]\,[1-2Q_3(r_2)]\,[1+2B(r_3)]\,[1+2B(r_4)]\,\big\rangle. \qquad (3.44)$$

We are still left with one unwanted piece which cannot be evaluated or canceled with

something else. Any other combination of the generators of the Lie superalgebra at four points will generate more terms on applying Wick's theorem and cannot be canceled out.

Now we see the special feature of the three point calculation. We had two Green's function products (by applying Wick's theorem), of which only one was necessary. The supersymmetric formulation gave us one more equation due to boson-fermion interchangeability. The unwanted piece canceled between the fermionic and bosonic equations. This fact does not help us in higher correlation functions as they have more unwanted pieces. It is also clear that situation becomes worse for higher n-point functions. Interestingly, the same conclusion was reached in a very different way in Ref. [32].

3.6   Local density of states and point contact conductance

Having considered the multifractal calculation in detail, the calculation of other boundary critical exponents is completely analogous and we list only the important results. Some of the bulk exponents were found in Refs. [23, 31, 32] using a very different technique. The averaged local density of states (LDOS), summed over the spin indices, can be written in terms of Green's functions as

$$\langle \rho^x(r, \epsilon) \rangle = \frac{1}{4\pi} \overline{\text{tr}\left[G_R(r, r) - G_A(r, r)\right]} = \frac{1}{2\pi} \overline{\text{tr}\, G_R(r, r)} - 1. \qquad (3.45)$$

This can again be expressed in terms of the sl(2|1) supersymmetry generators as $(1/2\pi)\langle 2B(r) \rangle$. This average, following the same steps presented in Sec. 3.5.2, can

be written in terms of percolation probabilities as

$$\langle 2B(r) \rangle = 1 - \sum_N P(r; N) \cos 2N\epsilon. \qquad (3.46)$$

(The same result was also obtained in Ref. [31] using, as mentioned, different techniques.) As we have mentioned at the end of Sec. 3.4, the boundary and the bulk scaling dimensions of the one hull operator are $x_s = 1/3$ and $x_b = 1/4$. The latter value implies that the percolation hull has fractal dimension $2 - x_b = 7/4$, so that $P(r, N) \sim N^{-8/7}$ for r in bulk. This yields, according to Eq. (3.45), the following scaling behavior of the LDOS [23]

$$\rho^b(\epsilon) \propto \epsilon^{x_b/(2-x_b)} = \epsilon^{1/7}. \qquad (3.47)$$

Note that $2 - x_b = 7/4$ is the dynamic critical exponent governing the scaling of energy with the system size L at SQH criticality, so that the level spacing at $\epsilon = 0$ (and thus the characteristic energy of critical states) is $\delta \sim L^{-7/4}$. In our case, when the point r is located at the boundary we find

$$P(r, N) \sim N^{-1-x_s/(2-x_b)} = N^{-25/21}, \qquad (3.48)$$

and the LDOS scaling

$$\rho^s(r, \epsilon) \propto \epsilon^{x_s/(2-x_b)} = \epsilon^{4/21}. \qquad (3.49)$$

Here we have used the bulk dynamic critical exponent in determining the energy scaling of the boundary LDOS. This is because we are dealing with an 'ordinary surface transition' and here surface (boundary) criticality is driven by the divergence

of the bulk correlation length [43]. Thus the scaling of LDOS changes between bulk and boundary. This means, as was mentioned in Sec. 3.5.1, that the average of the (square of the) wave function amplitude is suppressed at the boundary, giving rise to a non-vanishing value of $\mu_{x=s} = 1/3 - 1/4 = 1/12$ (see Eq. (2.19)).

A similar procedure is adopted for the calculation of other boundary exponents. (Many of the calculated exponents are given in Tables 3.1 and 3.2). The boundary diffusion propagator can be written as

$$\langle \Pi_{ss}(r_1, r_2) \rangle = 2 \langle V_-(r_1) W_+(r_2) \rangle, \tag{3.50}$$

where r_1 and r_2 lie at the boundary. In terms of percolation probabilities this reads

$$\langle \Pi_{ss}(r_1, r_2) \rangle = 2 \sum_N P(r_1, r_2; N) \, z^{2N}. \tag{3.51}$$

Taking the limit $z \to 1$ (critical point), gives

$$\langle \Pi_{ss}(r_1, r_2) \rangle = 2 \sum_N P(r_1, r_2; N) = 2P(r_1, r_2). \tag{3.52}$$

Here the probability $P(r_1, r_2)$ for the points r_1 and r_2 to be connected by a hull of any length scales at the boundary as r^{-2x_s} giving

$$\langle \Pi_{ss}(r_1, r_2) \rangle \sim |r_1 - r_2|^{-2/3}. \tag{3.53}$$

Another physical quantity of interest is the boundary point-contact conductance. In a network model setting, this is defined as the conductance between two boundary links r_1 and r_2 which are cut to make it possible to insert and extract currents from

them [44]. In the second quantized formalism, this translates to

$$\langle g_{point}(r_1, r_2) \rangle \equiv \langle f_\uparrow^\dagger(r_1) f_\downarrow^\dagger(r_1) f_\downarrow(r_2) f_\uparrow(r_2) \rangle. \tag{3.54}$$

In terms of sl(2|1) generators, this equals $\langle Q_+(r_1) Q_-(r_2) \rangle$. Skipping here the mapping to percolation probabilities, we find that the point-contact conductance decays exactly in the same way as the diffusion propagator, and, in particular, scales as $|r_1 - r_2|^{-2/3}$ at the boundary, at criticality.

3.7   Exponents in other geometries

There are two distinct ways of extending our discussion of boundary behavior. The first one is when some of the points lie on the boundary while the others lie in the bulk. The other case is to consider boundaries with more complicated geometries, the simplest example of which would be a wedge with opening angle θ. (The boundary case, considered in the previous sections corresponds to $\theta = \pi$).

The two-point quantities are easily computed when one point r_1 lies in the bulk and the other point, r_2 is at the boundary. These scale as $r^{-(\eta_b + \eta_\parallel)/2}$ where η_b and $\eta_\parallel$ are the usual exponents giving the decay of the two point function in the bulk and along the boundary, respectively. Hence the diffusion propagator and the point-contact conductance between a point in the bulk and another at the boundary, both scale with distance r as $r^{-7/12}$.

In the case of multifractal exponents, we can calculate the scaling behavior of correlation functions similar to those in Eq. (3.12). But we should not interpret these as representing properties of a single multifractal since multifractality is essentially a single point property. With this caveat, the value of the quantity analogous to Δ_2

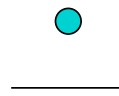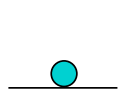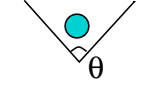when one point is in the bulk and another is at the boundary is $-1/4$.

Geometry			θ
LDOS	$\epsilon^{1/7}$	$\epsilon^{4/21}$	$\epsilon^{(4/21)(\pi/\theta)}$
Δ_2	$-1/4$	$-1/3$	$-\pi/3\theta$
Δ_3	$-3/4$	-1	$-\pi/\theta$

Table 3.1: One-point exponents in various geometries.
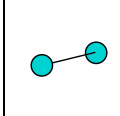
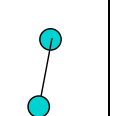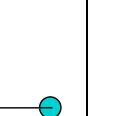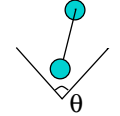| Geometry				θ
Diffusion Propagator	$r^{-1/2}$	$r^{-7/12}$	$r^{-2/3}$	$r^{-1/4-(1/3)(\pi/\theta)}$

Table 3.2: Two-point exponents in various geometries. The point-contact conductance has the same scaling behavior as the diffusion propagator.

The next generalization is to analyze the SQH transition in a wedge geometry. From the discussion in Sec. 2.4, it can be deduced that if we consider a 2-point function with one point lying near the wedge tip and another deep in the bulk at distance r, the two point function decays as $r^{-\eta_\theta}$ where

$$\eta_\theta = x_b + \frac{\pi}{\theta}x_s. \tag{3.55}$$

This enables us to calculate the relevant exponents. In the density of states calculation, we will have to replace x_s with $(\pi/\theta)x_s$.

The central result of this chapter is the calculation of boundary critical and multifractal exponents for the spin quantum Hall transition in various geometries (see Tables 3.1 and 3.2 for a summary of results).

Chapter 4

Power-law Random Banded Matrix Model

In this chapter, we analyze boundary criticality in the framework of the power-law random banded matrix (PRBM) model [17, 45]. The model is defined [45] as the ensemble of random Hermitean matrices $\hat{H}$. $\hat{H}$ is real for a time-reversal invariant system (orthogonal class, $\beta = 1$) and is complex otherwise (unitary class, $\beta = 2$). The matrix elements H_{ij} are independently distributed Gaussian variables with zero mean $\langle H_{ij} \rangle = 0$ and variance given by

$$\langle |H_{ij}|^2 \rangle = a^2(|i - j|) , \tag{4.1}$$

where $a^2(r)$ is given by

$$a^2(r) = \frac{1}{1 + (r/b)^{2\alpha}}. \tag{4.2}$$

At $\alpha = 1$ the model undergoes an LD transition from the localized ($\alpha > 1$) to the delocalized ($\alpha < 1$) phase. We concentrate below on the critical value $\alpha = 1$, when $a(r)$ decreases as $a(r) \propto 1/r$ at $r \gg b$. The parameter b determines the width of the band of non-zero matrix elements in the PRBM model.

In a straightforward interpretation, the PRBM model describes a 1D sample with random long-range hopping, the hopping amplitude decaying as $1/r^\alpha$ with the distance, with the parameter b setting the scale of hopping length. Furthermore, such an ensemble arises as an effective description in a number of physical contexts (see Ref. [17] for relevant references). At $\alpha = 1$ the PRBM model is critical for arbitrary values of b and shows all the key features of an LD critical point, including multifractality of eigenfunctions [17, 45]. The existence of the parameter b which labels

critical points is a distinct feature of the PRBM model: Eq. (4.1) defines a whole family of critical theories parametrized by b. The limit $b \gg 1$ represents a regime of weak multifractality, analogous to the conventional Anderson transition in $d = 2 + \epsilon$ with $\epsilon \ll 1$. This limit allows for a systematic analytical treatment via the mapping onto a supermatrix σ-model and the weak-coupling expansion [17, 45]. The opposite limit $b \ll 1$ is characterized by very strongly fluctuating eigenfunctions, similar to the Anderson transition in $d \gg 1$, where the transition takes place in the strong disorder (strong coupling in the field-theoretic language) regime. It is also accessible to an analytical treatment using a real-space renormalization-group (RG) method [17] introduced earlier for related models in Refs. [46, 47].

In addition to the feasibility of the systematic analytical treatment of both the weak-coupling and strong-coupling regimes, the PRBM model is very well suited for direct numerical simulations in a broad range of couplings. Here we employ the PRBM model for the analysis of boundary multifractality. The existence of a line of fixed points describing the critical system in the bulk makes this problem particularly interesting. We will demonstrate that the boundary critical theory of the PRBM model is not uniquely determined by the bulk properties. Instead, boundary criticality is controlled by an additional parameter characterizing the hopping amplitudes of particles reflected by the boundary.

The structure of this chapter is as follows. In Sec. 4.1 we formulate the model. Sec. 4.2 is devoted to the analytical study of the boundary multifractal spectrum, with the two limits $b \gg 1$ and $b \ll 1$ considered in Secs. 4.2.1 and 4.2.2, respectively. In Sec. 4.3 we compare our analytical work with numerical results obtained by our collaborators A. Mildenberger, F. Evers and A. D. Mirlin.

4.1   Description of the model

We consider now the critical PRBM model with a boundary at $i = 0$, which means that the matrix element H_{ij} is zero whenever one of the indices is negative. The important point is that, for a given value of the bulk parameter b, the implementation of the boundary is not unique, and that this degree of freedom will affect the boundary criticality. Specifically, we should specify what happens with a particle which "attempts to hop" from a site $i \geq 0$ to a site $j < 0$, which is not allowed due to the boundary. One possibility is that such hops are simply discarded, so that the matrix element variance is simply given by $\langle |H_{ij}|^2 \rangle = [1 + (i - j)^2/b^2]^{-1}$ for $i, j \geq 0$. More generally, the particle may be reflected by the boundary with certain probability p and "land" on the site $-j > 0$. This leads us to the following formulation of the model,

$$\langle |H_{ij}|^2 \rangle = J_{ij} \, , \tag{4.3}$$

$$J_{ij} = \frac{1}{1 + |i - j|^2 / b^2} + \frac{p}{1 + |i + j|^2 / b^2}. \tag{4.4}$$

While the above probability interpretation restricts p to the interval $[0, 1]$, the model is defined for all p in the range $-1 < p < \infty$. The newly introduced parameter p is immaterial in the bulk, where $i, j \gg |i - j|$ and the second term in Eq. (4.4) can be neglected. Therefore, the bulk exponents τ_q^{b} depend on b only (and not on p), and their analysis performed in Ref. [17] remains applicable without changes. On the other hand, as we show below by both analytical and numerical means, the boundary exponents τ_q^{s} are function of two parameters, b and p.

Equation (4.4) describes a semi-infinite system with one boundary at $i = 0$. For a finite system of length L (implying that the relevant coordinates are restricted to

$0 \leq i, j \leq L$) another boundary term, $p'/[1 + (i + j - 2L)^2/b^2]$, is to be included on the right-hand side of Eq. (4.4). In general, the parameter p' of this term may be different from p. This term, however, will not affect the boundary criticality at the $i = 0$ boundary, so we discard it below.

4.2 Analytical results for boundary multifractality in the PRBM model

4.2.1 $b \gg 1$ case

The regime of weak criticality, $b \gg 1$, can be studied via a mapping onto the supermatrix σ-model [17, 45], in analogy with the conventional random banded matrix model [48]. The σ-model action has the form

$$S[Q] = \frac{\beta}{4} \mathrm{Str} \left[(\pi \nu)^2 \sum_{i,j=0}^{\infty} J_{ij} Q_i Q_j - i\pi \nu \omega \sum_{i=0}^{\infty} Q_i \Lambda \right] , \qquad (4.5)$$

where Q_r is a 4×4 ($\beta = 2$) or 8×8 ($\beta = 1$) supermatrix field constrained by $Q_r^2 = 1$, $\Lambda = \mathrm{diag}(\mathbf{1}, -\mathbf{1})$, and Str denotes the supertrace [34]. Furthermore, J_{ij} are given by Eq. (4.4), ω is the frequency, and ν is the density of states given by the Wigner semicircle law

$$\nu(E) = \frac{1}{2\pi^2 b} (4\pi b - E^2)^{1/2} , \qquad |E| < 2\sqrt{\pi b}. \qquad (4.6)$$

For definitness, we will restrict ourselves to the band center, $E = 0$, below.

To calculate the multifractal spectrum to the leading order in $1/b \ll 1$, we will need the quadratic form of the action (4.5) expressed in terms of independent coordinates.

Parametrizing the field Q (constrained to $Q^2 = 1$) in the usual way,

$$Q_i = \Lambda \left(1 + W_i + \frac{W_i^2}{2} + \dots \right), \tag{4.7}$$

we obtain the action to the second order in the W fields,

$$S[W] = \frac{\pi\nu\beta}{4}\text{Str} \sum_{i,j=0}^{\infty} W_i \left[2\pi\nu(J_0^{(i)}\delta_{ij} - J_{ij}) - i\omega\delta_{ij} \right] W_j, \tag{4.8}$$

where

$$J_0^{(i)} = \sum_{k=0}^{\infty} J_{ik}. \tag{4.9}$$

The equation of motion for this action reads (after the Fourier transformation from the frequency into the time domain)

$$\frac{\partial W_i(t)}{\partial t} + \pi\nu \sum_{j=0}^{\infty} \left[\delta_{ij} J_0^{(i)} - J_{ij} \right] W_j(t) = 0. \tag{4.10}$$

This equation is the analog of the diffusion equation for a metallic system.

The σ-model action allows us to calculate the moments $\langle |\psi(r)|^{2q} \rangle$ at a given point r. On the perturbative level, the result reads [17, 45, 48]

$$\langle |\psi(r)|^{2q} \rangle = \langle |\psi(r)|^{2q} \rangle_{\text{RMT}} \left[1 + \frac{1}{\beta} q(q-1)\Pi_{rr} \right]. \tag{4.11}$$

Here the factor $\langle |\psi(r)|^{2q} \rangle_{\text{RMT}}$ is the random-matrix-theory result equal to $(2q - 1)!!L^{-q}$ for $\beta = 1$ and $q!L^{-q}$ for $\beta = 2$. The second term in the square brackets in Eq. (4.11), which constitutes the leading perturbative correction, is governed by the return probability Π_{rr} to the point r, i.e. the diagonal matrix element of the generalized diffusion propagator $\Pi_{rr'}$. The latter is obtained by the inversion of the

kinetic operator of Eqs. (4.8), (4.10),

$$\pi\nu \sum_{j=0}^{\infty} \left[\delta_{ij} J_0^{(i)} - J_{ij} \right] \Pi_{jm} = \delta_{im} - L^{-1}. \tag{4.12}$$

(The "diffusion" operator has a zero mode related to the particle conservation. The term L^{-1} in the RHS of Eq. (4.12) ensures that the inversion is taken on the subspace of non-zero modes.) In the bulk case, the inversion is easily performed via the Fourier transform,

$$\Pi_{rr'} \longrightarrow \tilde{\Pi}(k) = \frac{t}{8|k|}, \qquad |k| \ll b^{-1}, \tag{4.13}$$

with $t^{-1} = \frac{\pi}{4}(\pi\nu)^2 b^2$, i.e. $t = 4/b$ at the band center. The $1/|k|$ behavior of the propagator should be contrasted to its $1/k^2$ scaling for a conventional metallic (diffusive) system. This implies that the kinetics governed by Eq. (4.10) is superdiffusive (known as a Lévy flight [49, 50]). Substitution of (4.13) in Eq. (4.11) yields a logarithmic correction to the moments of the wave function amplitude,

$$\langle |\psi(r)|^{2q} \rangle = \langle |\psi(r)|^{2q} \rangle_{\text{RMT}} \left[1 + \frac{q(q-1)}{2\pi\beta b} \ln \frac{L}{b} \right]. \tag{4.14}$$

Equation (4.14) is valid as long as the relative correction is small. The logarithmic divergence of the return probability in the limit $L \to \infty$, which is a signature of criticality, makes the perturbative calculation insufficient for large enough L. The problem can be solved [17, 45] then by using the renormalization group (RG), which leads to the exponentiation of the perturbative correction in Eq. (4.14). This gives us a multifractal scaling as in Eq. (2.3) with the bulk multifractal exponents

$$\tau_q^b = (q-1) \left(1 - \frac{q}{2\pi\beta b} \right). \tag{4.15}$$

The first term (unity) in the second factor in Eq. (4.15) corresponds to the normal (metallic) scaling, the second one determines the anomalous multifractal exponents

$$\Delta_q^{\mathrm{b}} = \frac{q(1-q)}{2\pi\beta b}.$$ (4.16)

At the boundary, the behavior is qualitatively the same: the return probability Π_{rr} increases logarithmically with the system size L, in view of criticality. However, as we show below, the corresponding prefactor [and thus the prefactor in front of the second term in square brackets in Eq. (4.14)] is different. After the application of the RG this prefactor emerges in the anomalous multifractal exponent,

$$\Delta_q^{\mathrm{s}} = \frac{q(1-q)}{2\pi\beta b} R_p \equiv \Delta_q^{\mathrm{b}} R_p.$$ (4.17)

In the presence of a boundary the system is not translationally invariant anymore, which poses an obstacle for an analytical calculation of the return probability Π_{rr}. While for Lévy-flight models with absorbing boundary (that is obtained from our equation (4.10) with $p = 0$ by a replacement of $J_0^{(i)}$ with its bulk value J_0) analytical progress can be achieved via the Wiener-Hopf method [51], it is not applicable in the present case, since the kernel of Eq. (4.10) is not a function of $i - j$ only. We thus proceed by solving the classical evolution equation (4.10) numerically with the initial condition $W_i(0) = \delta_{ir}$. The value $W_r(t)$ of the solution at the point r (i.e. the probability to find the particle at the initial point) decays with time as $1/t$, so that the integral $\int dt W_r(t)$ yields the logarithmically divergent return probability discussed above. Extracting the corresponding prefactor, we find the anomalous multifractal exponent,

$$\frac{\Delta_q}{q(1-q)} = \frac{1}{\beta} t W_r(t)|_{t\to\infty}.$$ (4.18)

Note that the limit of the large system size $L \to \infty$ should be taken in Eq. (4.18) before $t \to \infty$, so that the particle does not reach the boundary for r in the bulk (or, for r at the boundary, does not reach the opposite boundary).

We have checked that the numerical implementation of Eqs. (4.18), (4.10) reproduces the analytical result (4.16) in the bulk. We then proceed with numerical evaluation of the boundary multifractal exponents Δ_q^{s}. For this purpose, we discretize the time variable in Eq. (4.10) with a step $\Delta t = 1/2$. With the parameters $\pi\nu = 1/\pi$, $b = 10$, $L = 10000$, and $t = 500$, the product $tW_r(t)$ yields its required asymptotic value with the accuracy of the order of 2%. The results for the corresponding prefactor R_p, as defined in Eq. (4.17), are shown in Fig. 4.1 for several values of p between 0 and 3. It is seen that the boundary exponents not only differ from their bulk counterparts but also depend on p.

For the particular case of the reflection probability $p = 1$ we can solve the evolution equation (4.10) and find Δ_q^{s} analytically. Indeed, the corresponding equation can be obtained from its bulk counterpart (defined on the whole axis, $-\infty < i < \infty$) by "folding the system" on the semiaxis $i > 0$ according to $W_i(t) + W_{-i}(t) \longrightarrow W_i(t)$, cf. Ref. [52,53]. This clearly leads to a doubling of the return probability, so that

$$R_1 = 2, \tag{4.19}$$

in full agreement with the numerical solution of the evolution equation.

4.2.2 $b \ll 1$ case

In the regime of small b the eigenstates are very sparse. In this situation, the problem can be studied by a real-space RG method that was developed in Ref. [46] for related models and in Ref. [17] for the PRBM model. Within this approach, one starts from
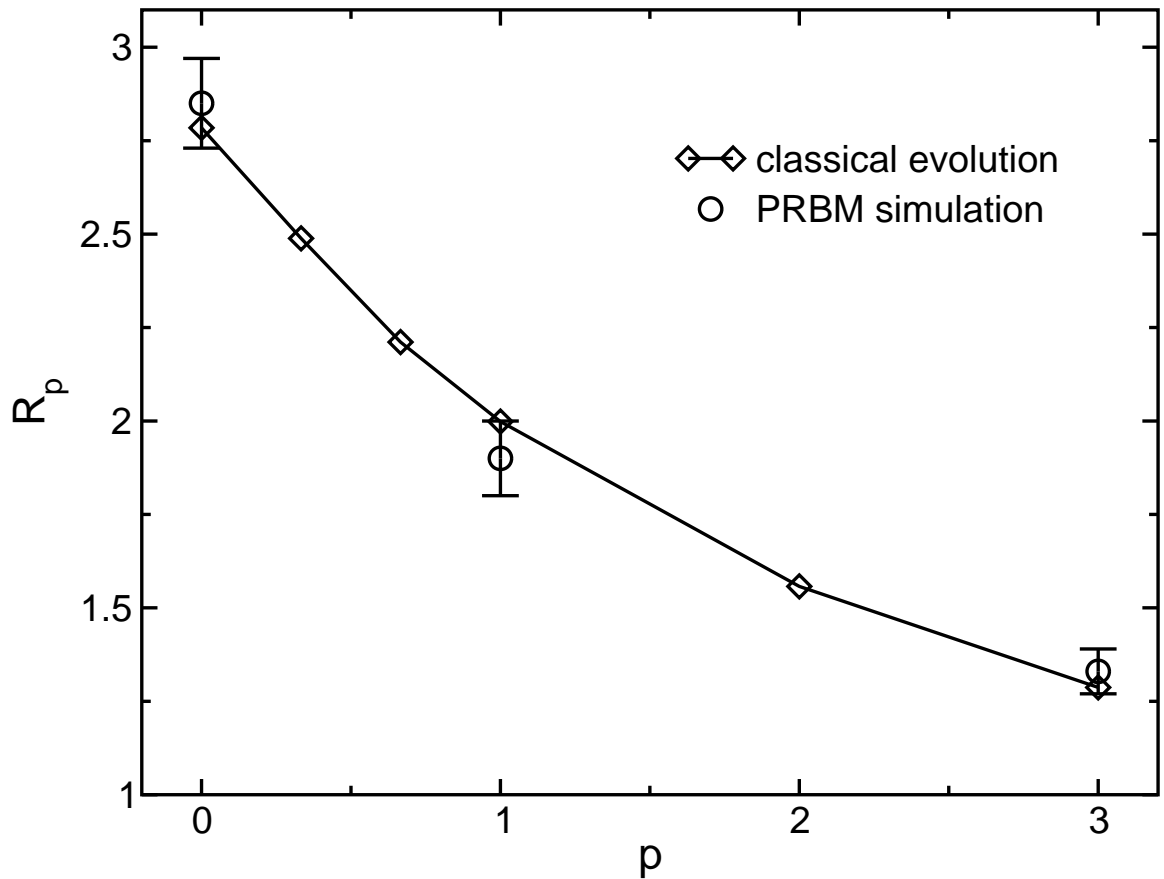
Figure 4.1: The ratio $R_p = \Delta_q^{\mathrm{s}}(b,p)/\Delta_q^{\mathrm{b}}(b)$ of the boundary and bulk anomalous multifractal exponents for large b, as a function of the reflection parameter p. Diamonds represent the results of the σ-model analysis with a numerical solution of the corresponding classical evolution equation, as described in Sec. 4.2.1. Circles represent a direct computer simulation of the PRBM model, Eqs. (4.3), (4.4), see Sec. 4.3, with $b = 8$. The ratio R_p has been evaluated for the range $0 < q < 1$, where the numerical accuracy of the anomalous multifractal exponents is the best. Within this interval, R_p is q-independent (within numerical errors) in agreement with Eq. (4.17).

the diagonal part of the Hamiltonian and then consecutively includes into consideration non-diagonal matrix elements H_{ij} with increasing distance $\rho = |i - j|$. The central idea is that only rare events of resonances between pairs of remote states are important, and that there is an exponential hierarchy of scales at which any given state finds a resonance partner: $\ln \rho_1 \sim b^{-1}$, $\ln \rho_2 \sim b^{-2}$, ... This allows one to formulate RG equations for evolution of quantities of interest with the "RG time" $t = \ln \rho$. We refer the reader for technical details of the derivation to Ref. [17] where the evolution equation of the distribution $f(P_q)$ of the inverse participation ratios, $P_q = \sum_r |\psi(r)|^{2q}$, as well as of the energy level correlation function, was derived. In the present case, we are interested in the statistics of the local quantity, the wave function intensity $|\psi(r)|^2$ at a certain point r. Assuming first that r is in the bulk and generalizing the derivation of Ref. [17], we get the evolution equation for the corresponding distribution function $f(y \equiv |\psi(r)|^2)$,

$$\frac{\partial f(y, \rho)}{\partial \ln \rho} = \frac{2b}{\pi} \int_0^{\pi/2} \frac{d\theta}{\sin^2 \theta \cos^2 \theta} \int_{-\infty}^{\infty} dy' f(y', \rho)$$
$$\times [\delta(y - y' \cos^2 \theta) + \delta(y - y' \cos^2 \theta) - \delta(y - y') - \delta(y)]. \qquad (4.20)$$

Equation (4.20) is written for $\beta = 1$; in the case of $\beta = 2$ one should make a replacement $b \longrightarrow (\pi/2\sqrt{2})b$. The physical meaning of Eq. (4.20) is rather transparent: its right-hand side is a "collision integral" describing a resonant mixture of two states with the intensities y' and 0 at the point r, leading to formation of superposition states with the intensities $y' \cos^2 \theta$ and $y' \sin^2 \theta$. Multiplying Eq. (4.20) by y^q and integrating over y, we get the evolution equation for the moments $\langle y^q \rangle$,

$$\frac{\partial \langle y^q \rangle}{\partial \ln \rho} = -2bT(q)\langle y^q \rangle , \qquad (4.21)$$

where

$$T(q) = \frac{1}{\pi} \int_0^{\pi/2} \frac{d\theta}{\sin^2\theta \cos^2\theta}(1 - \cos^{2q}\theta - \sin^{2q}\theta) = \frac{1}{2^{2q-3}}\frac{\Gamma(2q-1)}{\Gamma(q)\Gamma(q-1)}. \quad (4.22)$$

The RG should be run until ρ reaches the system size L. Thus, the bulk multifractal exponents are equal to

$$\tau_q^b = 2bT(q), \quad (4.23)$$

in agreement with Ref. [17].

How will the evolution equation (4.20) be modified if the point r is located at the boundary? First, the factor 2 in the right-hand side of (4.20) will be absent. Indeed, this factor originated from the probability to encounter a resonance. In the bulk, the resonance partner can be found either to the left or to the right, thus the factor of two. For a state at the boundary only one of these possibilities remains, so this factor is absent. Second, one should now take into account also the second term in the variance J_{ij} of the matrix element H_{ij}, Eq. (4.4). In view of the hierarchy of resonances described above, the relevant matrix elements will always connect two points, one of which is much closer to the boundary than the other (say, $i \ll j$). In this situation, the two terms in (4.4) become equivalent (up to the prefactor p in the second term) and can be combined,

$$J_{ij} \simeq \frac{(1+p)b^2}{j^2}, \qquad i \ll j. \quad (4.24)$$

Therefore, the effect of the second term amounts to the rescaling $b \longrightarrow (1+p)^{1/2}b$. Combining both the effects, we get the boundary multifractal exponents,

$$\tau_q^s = (1+p)^{1/2}bT(q) = \frac{(1+p)^{1/2}}{2}\tau_q^b. \quad (4.25)$$

The above real-space RG method works for $q > 1/2$, where the multifractal exponent τ_q is small [1]. The results can, however be extended to the range of $q < 1/2$ by using the symmetry relation between the multifractal exponents [54],

$$\Delta_q = \Delta_{1-q}. \tag{4.26}$$

Independent of whether q is larger or smaller than $1/2$, the obtained relation between the boundary and the bulk multifractal spectra can be formulated in the following way for the $b \ll 1$ case:

$$\tau_q^{\mathrm{s}}(b, p) = \tau_q^{\mathrm{b}}(b \longrightarrow b(1+p)^{1/2}/2). \tag{4.27}$$

4.3   Comparison with numerical simulations

The numerical work presented in this section was done by our collaborators A. Mildenberger, F. Evers and A. D. Mirlin. The details of the numerical simuations can be found in our joint publication [55]. Here we present only the results.

Fig. 4.2 illustrates nicely our main findings. We illustrate the dependence of the anomalous multifractal dimension $\Delta_2 \equiv D_2 - 1$ on b in the bulk and at the boundary, for three different values of the reflection parameter p. It is seen, first of all, that the bulk exponent Δ_2^b does not depend on p, in agreement with the theory. Second, the boundary exponent Δ_2^s is different from the bulk one. Third, the boundary exponent

---

1. Strictly speaking, Eqs. (4.23), (4.22) are valid for all $q > 1/2$ in the limit $b \to 0$. For a finite (but small) b, Eq. (4.23) breaks down in a narrow interval of q above $1/2$, namely for $q - 1/2 \lesssim 1/\ln b^{-1}$. Indeed, the evolution equation (4.20) assumes that resonances are rare, i.e. that the angle θ describing the resonant mixture is large compared to its typical, non-resonant, value $\sim b$. On the other hand, when q approaches $1/2$, the integral in Eq. (4.22) converges at $\theta \sim \exp[-1/(q - 1/2)]$. Comparing this with b, we get the above restriction on the validity of Eq. (4.23).

is not determined by b only, but rather depends on the boundary parameter p as well. The lower panel of Fig. 4.2 demonstrates the agreement between the numerical results and the analytical asymptotics of small and large b.

Having discussed the b-dependence of the fractal exponent with fixed q (equal to 2) shown in Fig. 4.2, we turn to Fig. 4.3, where the whole multifractal spectra Δ_q are shown for fixed large values of b. Specifically, the anomalous multifractal dimensions Δ_q^{s} and Δ_q^{b} are presented for $b = 2$, 4 and 8, with the reflection parameter chosen to be $p = 1$. For all curves the q dependence is approximately parabolic, as predicted by the large-b theory, Eqs. (4.16) and (4.17), with the prefactor inversely proportional to b. To clearly demonstrate this, we plot in the lower two panels the exponents Δ_q divided by the corresponding analytical results of the large-b limit. While for moderately large b the ratio shows some curvature, the latter disappears with increasing b and the ratio approaches unity, thus demonstrating the full agreement between the numerical simulations and the analytical predictions. It is also seen in Fig. 4.3 that the bulk multifractal spectrum for $b = 4$ and the boundary spectrum for $b = 8$ are almost identical, in agreement with Eq. (4.19). The same is true for the relation between the bulk spectrum for $b = 2$ and the boundary spectrum for $b = 4$.

The ratio of the large-b boundary and bulk anomalous multifractal dimensions, $R_p = \Delta_q^{\mathrm{s}}/\Delta_q^{\mathrm{b}}$, for several values of the reflection parameter, $p = 0$, 1 and 3 was also calculated. As shown in Fig. 4.1, the results are in good agreement with the σ-model predictions for R_p obtained in Sec. 4.2.1.

In Fig. 4.4 the boundary and bulk multifractal spectra are shown for the case of small b. While the spectra are strongly non-parabolic in this limit, they clearly exhibit the symmetry $q \rightarrow 1-q$, Eq. (4.26). The data are in good agreement with the RG results of Sec. 4.2.2. In particular, the boundary spectrum for $p = 3$ is essentially identical to the bulk spectrum, as predicted by Eq. (4.27). In the inset, the boundary
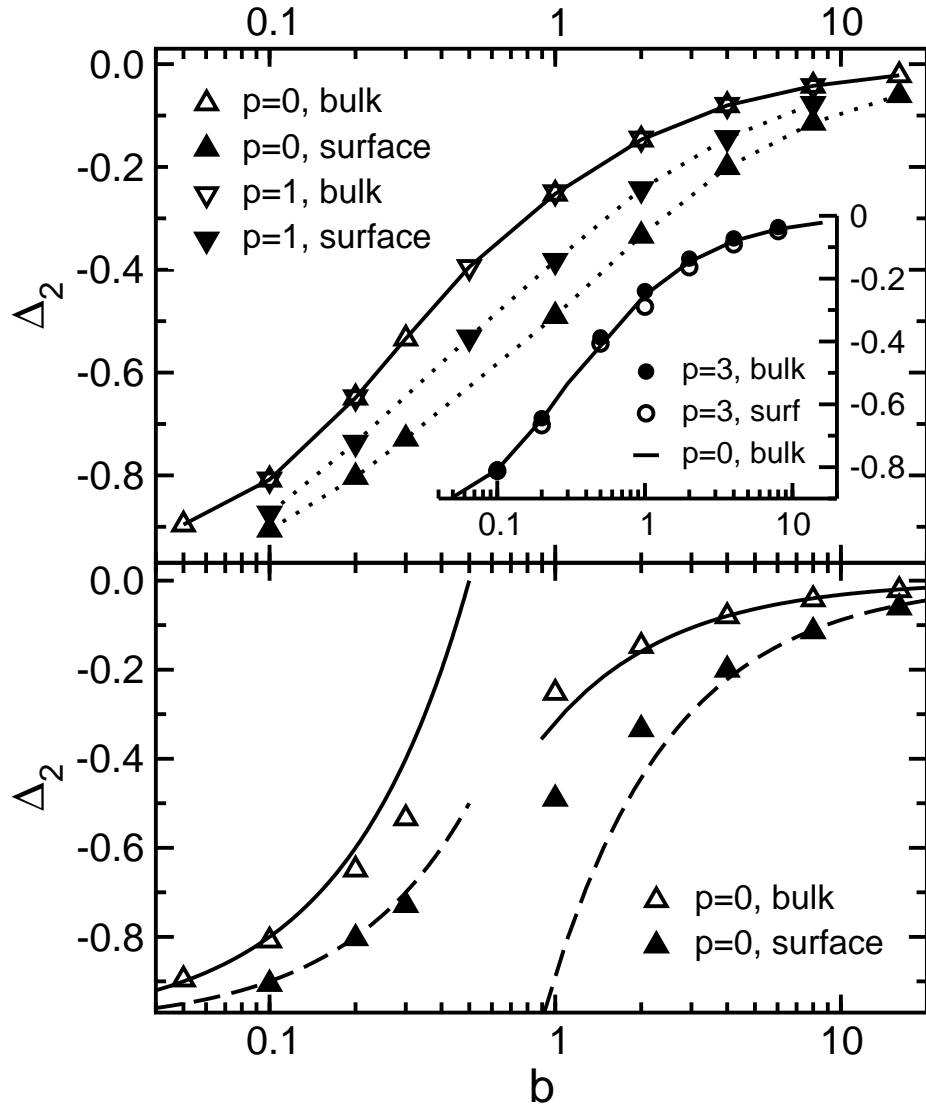
Figure 4.2: Upper panel: Anomalous multifractal exponent $\Delta_2 \equiv D_2 - 1$ as a function of b from numerical simulations in the bulk and at the boundary for the reflection parameter $p = 0$ and 1. The inset shows data for $p = 3$ compared to the $p = 0$ bulk values. Lower panel: Boundary and bulk data for $p = 0$ compared with analytical results for small and large b (using $R_0 = 2.78$), Eqs. (4.16), (4.17), (4.23), (4.25).
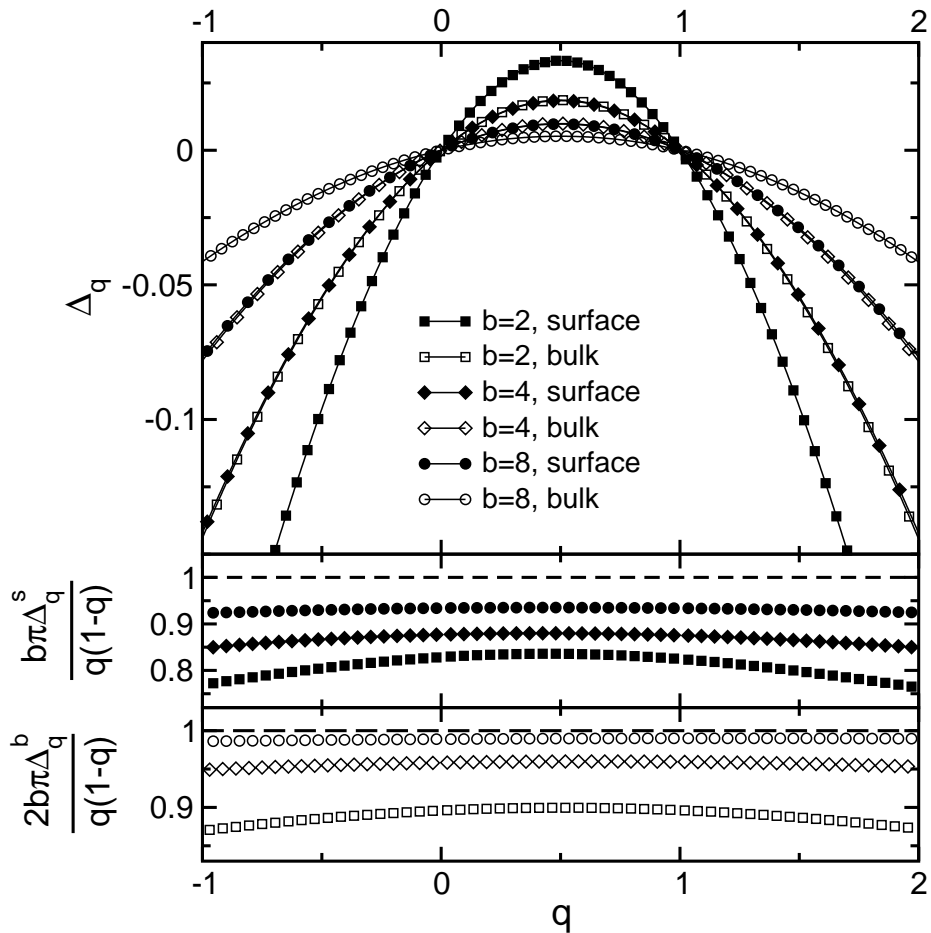
Figure 4.3: Upper panel: Boundary and bulk multifractal spectra, Δ_q^{s} and Δ_q^{b}, at $b = 2$, 4, and 8 for the reflection parameter $p = 1$. In accordance with Eq. (4.19), the boundary multifractality spectrum is enhanced by a factor close to two compared to the bulk. Middle panel: Boundary spectrum divided by the analytical large-b result, Eq. (4.17). The dashed line represents the analytical result for $b \gg 1$. With increasing b, the numerical data nicely converges towards the analytical result. Lower panel: Analogous plot for the bulk spectrum, Eq. (4.16). The error estimate from the finite size extrapolation is 3%.
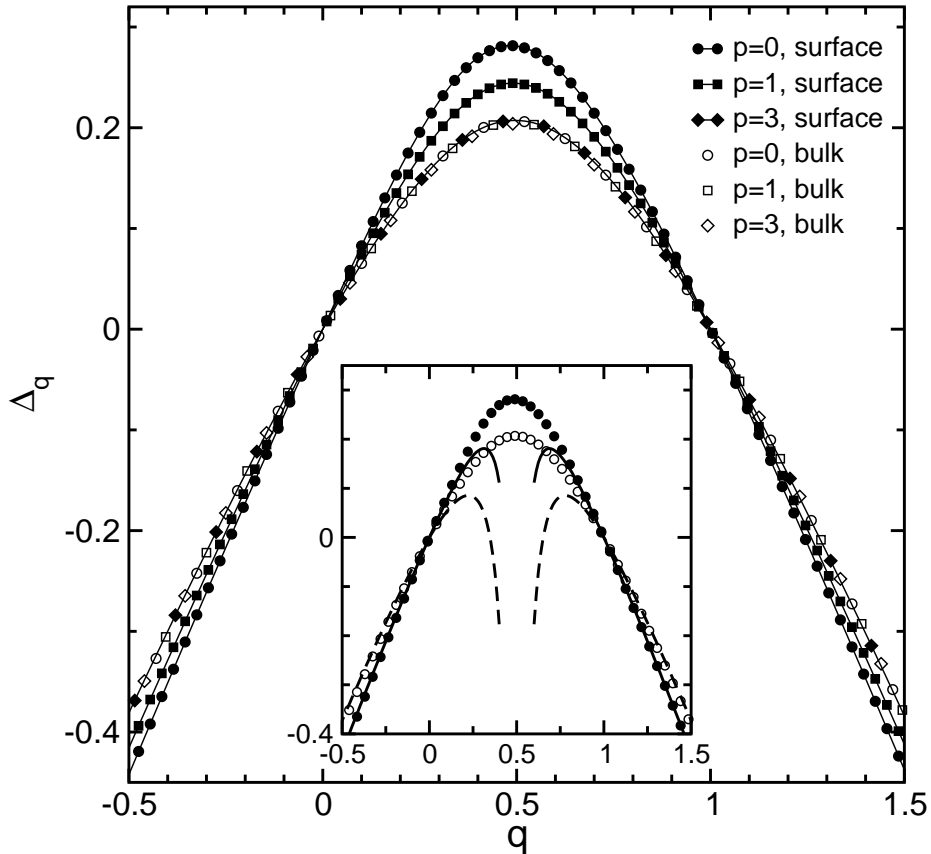
Figure 4.4: Main panel: Numerically determined boundary and bulk anomalous multifractal dimensions Δ_q at $b = 0.1$ for $p = 0$, 1, and 3. As expected, the bulk anomalous multifractal dimension is independent of the value of p. In accordance with Eq. (4.27), for $p = 3$ boundary and bulk dimensions have the same values. Inset: The $p = 0$ data compared to the analytical results, boundary [solid line, Eq. (4.25)] and bulk [dashed line, Eq. (4.23)]. Analytical data have been calculated for $q \geq 0.6$ and mirrored for $q \leq 0.4$ by using the symmetry relation $\Delta_q = \Delta_{1-q}$. Note that the analytical result (4.23) breaks down in the vicinity of $q = 1/2$, at $|q - 1/2| \lesssim 1/\ln b^{-1}$, see footnote [1]. At the boundary, one should replace $b \to b(1 + p)^{1/2}/2$ in this condition. We see, indeed, that for $b = 0.1$, $p = 0$ the analytical formula works upto $|q - 1/2| \simeq 0.4$ in the bulk and $|q - 1/2| \simeq 0.3$ at the boundary.

and bulk multifractal spectra for $p = 0$ are compared with the analytical asymptotics, Eqs. (4.23), (4.25), supplemented by the symmetry relation (4.26). Again, a very good agreement is seen, except for a vicinity of $q = 1/2$, where Eqs. (4.23), (4.25) break down (refer footnote [1]).

Chapter 5

2D Symplectic-Class Anderson Transition

In this chapter, we study boundary multifractality at the 2D LD transition for non-interacting electrons with spin-orbit scattering (symplectic universality class) [56]. Numerical simulations done by our collaborators H. Obuse and A. Furusaki are used to verify many of the predictions made in Chapter [2]. In particular we will verify the hypothesis of conformal invariance itself at this critical point. The results described in this chapter were reported in Ref. [57].

Let us first point out a number of important issues which have to be taken into consideration when wave functions near boundaries and corners are studied. The relation in Eq. (2.23) relating the boundary and corner anomalous multifractal dimensions implies the following relation for the Legendre-transformed variables defined in Eq. (2.5):

$$\alpha_q^\theta - 2 = \frac{\pi}{\theta}(\alpha_q^{\mathrm{s}} - 2), \qquad\qquad f^\theta(\alpha_q^\theta) = \frac{\pi}{\theta}\left[f^{\mathrm{s}}(\alpha_q^{\mathrm{s}}) - 1\right]. \qquad (5.1)$$

Eqs. (5.1) are valid only if $\alpha_q^\theta > 0$, because α is non-negative for normalized wave functions [17,58]. It is expected [17] that for $q > q_\theta$ (where q_θ is a solution to $\alpha_q^\theta = 0$) the exponents τ_q^θ become independent of q, while $\alpha_q^\theta = 0$. With the definition Eq. (2.3), this leads to a modified relation between Δ_q^θ and Δ_q^{s}:

$$\Delta_q^\theta = \begin{cases} \dfrac{\pi}{\theta}\Delta_q^{\mathrm{s}}, & q < q_\theta, \\[2mm] \dfrac{\pi}{\theta}\Delta_{q_\theta}^{\mathrm{s}} - 2(q - q_\theta), & q > q_\theta. \end{cases} \qquad (5.2)$$

We now discuss the numerical simulations done by our collaborators. The numerical details for the simulations can be found in our joint publication [57]. Here we
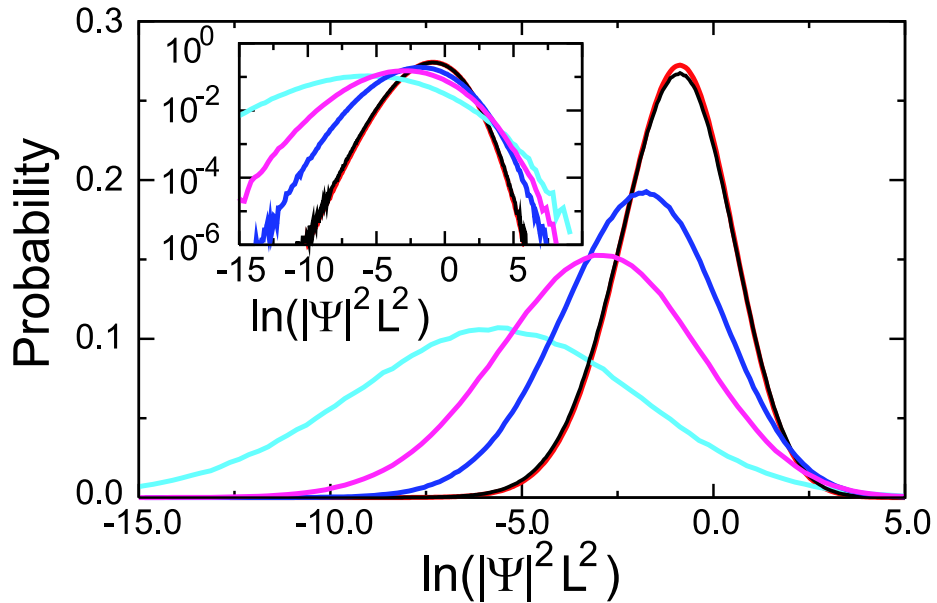
Figure 5.1: Probability distribution functions of logarithm of wave function intensities in the bulk (black and red), in the boundary (blue), and in the corner region with $\theta = \pi/2$ (pink) and $\theta = \pi/4$ (light blue); $L = 120$. Inset: Semi-logarithmic plot.

only summarize the results and their analysis.

Fig. 5.1 shows the probability distribution functions (PDFs) of $\ln |\psi(\boldsymbol{r})|^2$ measured for $\boldsymbol{r}$ at corners with angle $\theta = \pi/4$ (light blue) and $\theta = \pi/2$ (pink), at the boundary (blue), and in the bulk (red and black) at a fixed system size L. Each PDF is normalized in the region where it is defined. Clearly, the PDFs for bulk, boundary, and corner with $\theta = \pi/2$ and $\theta = \pi/4$, are all different, and, in this order, the peak position is shifted to the left, in agreement with the expectation that wave function amplitudes should be smaller near edges. In the same order, the distributions become broader with longer (presumably power-law) tails at $|\psi(r_x)|^2 L^2 \gg 1$. This means that for large q the moments $\overline{|\psi(\boldsymbol{r_x})|^{2q}}$ can become larger near edges (corners) than in the bulk, as the higher moments are dominated by long tails [17].
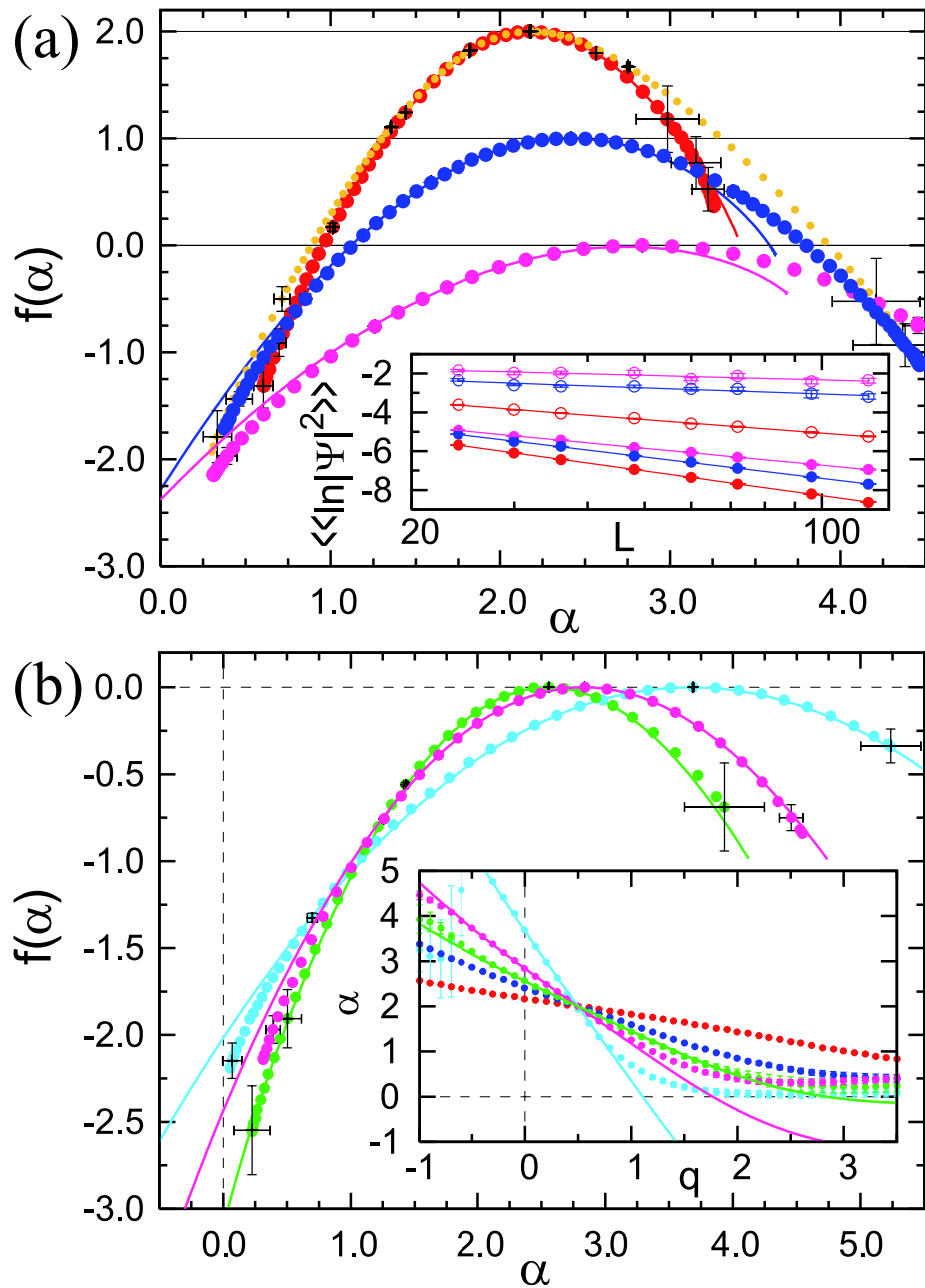
Figure 5.2: (a) Bulk (red), boundary(blue), corner $\theta = \pi/2$ (pink), and whole sample (orange) $f(\alpha)$ spectra, with error bars shown at integer values of q. Red, blue, and pink curves represent $f^{\mathrm{x}}(4-\alpha)+\alpha-2$. Inset: Scaling plot of Eq. (5.3) at $q = 1$ (filled circles) and $q = 3$ (open circles). (b) Corner $f(\alpha)$ spectra at $\theta = \pi/4$ (light blue), $\pi/2$ (pink), and $3\pi/4$ (green), with error bars shown at integer q (and at $q = -0.5$ for $\theta = \pi/4$). Curves represent the conformal relation (5.1). Inset: Numerical results for α_q^{x} compared with Eqs. (5.1) (colored curves).

Numerically α_q^{x} and $f^{\mathrm{x}}(\alpha_q^{\mathrm{x}})$ can be obtained using the relations

$$\langle\langle \ln|\psi(r_x)|^2 \rangle\rangle_q \equiv \frac{\overline{|\psi(r_x)|^{2q}\ln|\psi(r_x)|^2}}{\overline{|\psi(r_x)|^{2q}}} \sim -\alpha_q^{\mathrm{x}}\ln L, \tag{5.3}$$

$$\ln\overline{|\psi(\boldsymbol{r_x})|^{2q}} \sim \left[f^{\mathrm{x}}(\alpha_q^{\mathrm{x}}) - \alpha_q^{\mathrm{x}}q - d_{\mathrm{x}} \right]\ln L. \tag{5.4}$$

These follow directly from the definitions in Eq. (2.3), (2.5) and (2.6). Different values of q in Eq. (5.3) give different We note that μ^x is zero since the density of states does not show critical behavior at this transition. The inset of Fig. 5.2(a) shows $\langle\langle \ln|\psi|^2 \rangle\rangle_q$ as functions of L, computed for bulk (x = b), boundary (x = s), and corners ($\theta = \pi/2$). This inset exhibits distinct scaling behavior for bulk, boundary, and corner regions for the displayed values of $q = 1$ (filled circles) and $q = 3$ (empty circles).

Fig. 5.2(a) shows $f^{\mathrm{x}}(\alpha)$ of the bulk, boundary, and corner ($\theta = \pi/2$) regions. Clearly, in this order, the spectra $f^{\mathrm{x}}(\alpha)$ are seen to become broader and their maxima α_0^{x} are shifted to the right in accordance with Fig. 5.1 and Eq. (2.6). (Recall that the maximal values of $f^{\mathrm{x}}(\alpha)$ are the spatial dimensions d_{x}.) The plot of $f^{\mathrm{w}}(\alpha)$ for the whole sample with just boundaries and no corners (Fig. 5.2(a), orange) clearly represents the convex hull of $f^{\mathrm{b}}(\alpha)$ and $f^{\mathrm{s}}(\alpha)$ as discussed in Sec. 2.2. Notice that $f^{\mathrm{w}}(\alpha)$ deviates from $f^{\mathrm{b}}(\alpha)$ already at $f(\alpha) \approx 1.5$ (for $q < 0$). This confirms the prediction in Chapter 2 that the presence of boundaries drastically affects the multifractal spectrum of the system even in the thermodynamic limit and also in a typical sample (where $f(\alpha) \geqslant 0$) [17].

The data points of the bulk spectrum $f^{\mathrm{b}}(\alpha)$ [red dots in Fig. 5.2(a)] lie on top of the red curve representing data for $f^{\mathrm{b}}(\alpha_{1-q}^{\mathrm{b}})$ in Eq. (5.5). This confirms the following

relation which is the consequence of the symmetry relation in Eq. (4.26):

$$f^{\mathrm{x}}(\alpha_{1-q}^{\mathrm{x}}) - \frac{\alpha_{1-q}^{\mathrm{x}}}{2} = f^{\mathrm{x}}(\alpha_q^{\mathrm{x}}) - \frac{\alpha_q^{\mathrm{x}}}{2}, \qquad\qquad \alpha_{1-q}^{\mathrm{x}} = 4 - \alpha_q^{\mathrm{x}}, \qquad (5.5)$$

This in particular would seem to imply that α^{x} cannot exceed 4. This is not true in general for systems with boundaries and the symmetry relation cannot be used for all values of q. Here we propose, as a refinement, that the symmetry relation in Eq. (4.26) is valid for corners of any angle θ including $\theta = \pi$ (straight boundaries), but only in the range of q satisfying $1 - q_\theta \leqslant q \leqslant q_\theta$, corresponding precisely [54,57] to the range $0 \leqslant \alpha_q^\theta \leqslant 4$. Furthermore, we cannot make any statements about Δ_q^θ for values of q outside of this range. As mentioned before Eq. (5.2), the dependence on q of Δ_q^θ is linear for $q > q_\theta$ (corresponding to the termination of the multifractal spectrum [2]), whilst it may, in general, continue to be non-linear for $q < 1 - q_\theta$, even [57,54] when $\alpha_q^\theta > 4$.] Thus the boundary spectrum $f^{\mathrm{s}}(\alpha)$ (blue dots in Fig. 5.2(a)) is also seen to satisfy the relation (5.5), but for the restricted range $1 \lesssim \alpha^{\mathrm{s}} \lesssim 3$. We note that the numerical results for α_q^θ exceed 4 when $q \lesssim -0.1$ for $\theta = \pi/4$, and $q \lesssim -0.7$ for $\theta = \pi/2$ [Fig. 5.2(b) and inset]. Even the maximum α_0^θ of $f^\theta(\alpha)$ will exceed 4 for sufficiently small angles θ. Thus, the numerical data strongly support our refinement of the symmetry relation.

Figure 5.2(b) shows the corner spectra $f^\theta(\alpha)$ at $\theta = 3\pi/4$ (green), $\pi/2$ (pink), and $\pi/4$ (light blue). As θ decreases, the peak position moves to the right and the spectra become broader, indicating that at smaller θ the typical value of a wave function amplitude is smaller but its distribution is broader. The numerical data (dots) are compared with the curves predicted from conformal invariance, Eq. (5.1), using $f^{\mathrm{s}}(\alpha^{\mathrm{s}})$ of Fig. 5.2(a) within the range $1 \lesssim \alpha^{\mathrm{s}} \lesssim 3$, where $|q|$ is sufficiently small to ensure good numerical accuracy. The agreement between the numerical data and

the predicted curves is excellent, confirming the presence of conformal symmetry.

The inset of Fig. 5.2(b) shows α_q^{x} where the curves represent α_q^θ computed with α_q^{s} as input in Eq. (5.1). Note that $\alpha^{\mathrm{x}} = 2$ at $q = 1/2$ as a consequence of Eq. (5.5). We see that the numerical data for α_q^θ deviate from the predicted curves, Eq. (5.1), when $\alpha_q^\theta \lesssim 1$, in order to satisfy the constraint $\alpha_q^\theta > 0$. We expect that in the limit $L \to \infty$, α_q^θ be given by Eq. (5.1) for $q < q_\theta$ and by $\alpha_q^\theta = 0$ for $q > q_\theta$.

The anomalous multifractal dimensions Δ_q^{x} are computed numerically from the scaling $\overline{|\psi(\boldsymbol{r})|^{2q}} / (\overline{|\psi(\boldsymbol{r})|^2})^q \sim L^{-\Delta_q^{\mathrm{x}}}$, which follows from Eq. (2.3). Figure 5.3(a) shows the bulk anomalous multifractal dimension Δ_q^{b} (red) and its mirror image across the $q = 1/2$ line $\Delta_{1-q}^{\mathrm{b}}$ (grey), both rescaled by $q(1 - q)$. Note that this rescaling magnifies small numerical errors around $q = 0$ and $q = 1$. Nevertheless the numerical data in the bulk satisfy the symmetry relation in Eq. (4.26) for $-1 < q < 2$ where statistical errors are small. It is also clear from Fig. 5.3(a) that $\Delta_q^{\mathrm{b}}/[q(1 - q)]$ varies with q, which means that the bulk spectrum $f^{\mathrm{b}}(\alpha)$ is not exactly parabolic.

Figure 5.3(b) compares Δ_q^{x} for bulk, boundary, and corners with $\theta = \pi/4, \pi/2$, and $3\pi/4$. The solid curves represent the theoretical prediction (5.2) from the conformal mapping, where Δ_q^{s} is taken from Fig. 5.3(b). For sufficiently small values of $|q|$ the numerical results of Δ_q^θ are in good quantitative agreement with the prediction (5.2). It is precisely for small $|q|$ that the numerical data are most accurate [1]. This provides direct evidence for the presence of conformal symmetry at the symplectic-class LD transition.

The inset of Fig. 5.3(b) shows the exponents τ_q^{x} for bulk, boundary, and corners. We see that $\tau_q^{\pi/4}$ (light blue) is constant for $q > q_{\pi/4} \approx 1$ reflecting the exchange

---

[1]. For $q \gtrsim 1$, Fig. 5.3(b) shows discrepancies between the numerical results and the prediction from CFT, enhanced by the $(1 - q)^{-1}$ factor. In this range of q the moments of $|\psi|^2$ are dominated by rare events, which makes it difficult to obtain accurate numerical data.

between top and bottom lines in Eq. (5.2) which happens at $\alpha_q^{\pi/4} = 0$. It appears that $\tau_q^{\pi/4}$ becomes smaller than both τ_q^{s} and τ_q^{b} for $q \gtrsim 2.5$, which is when the corner exponent $\tau_q^{\pi/4}$ controls the multifractal spectrum of the whole sample with a $\pi/4$ corner, as shown in black. In a sample without corners such as a cylinder, the boundary exponent τ_q^{s} controls the multifractal spectrum of the entire sample for sufficiently large q. This confirms and generalizes the predictions made in Sec. 2.2.
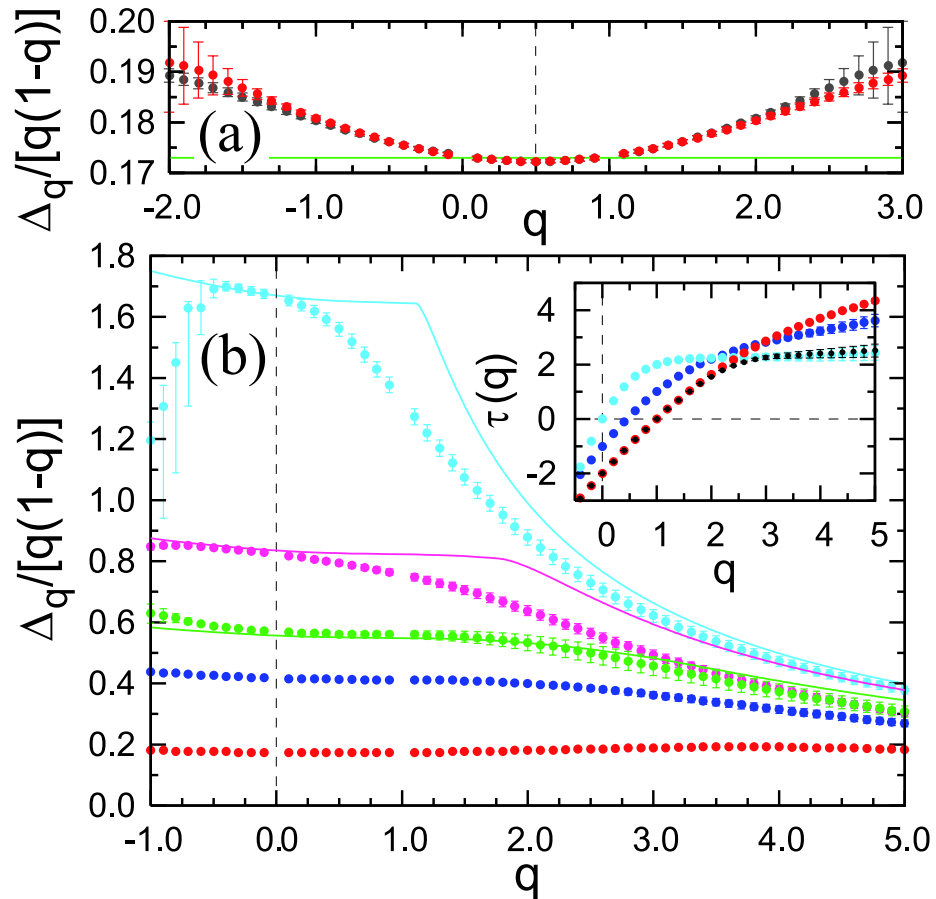
Figure 5.3: (a) The numerical data for the bulk exponents Δ_q^{b} (red) are compared with their mirror image $\Delta_{1-q}^{\mathrm{b}}$ (grey). The green line represents $\alpha_0^{\mathrm{b}} - 2$. (b) The exponents $\Delta_q/[q(1-q)]$ for the bulk (red), the boundary (blue), and corners with $\theta = \pi/4$ (light blue), $\pi/2$ (pink), and $3\pi/4$ (green). The curves represent the theoretical prediction, Eq. (5.2). Inset: Bulk (red), boundary (blue), and corner ($\theta = \pi/4$, light blue) exponents τ_q^{x}, and τ_q^{w} for a whole rhombus shaped sample with corners $\theta = \pi/4$ (black).

Chapter 6

Integer Quantum Hall (IQH) Plateau Transition

The physics of the quantum Hall effect has been an exciting area of research for more than two decades [59, 60]. While much progress has been made in this area, the identification of an analytically tractable theory describing the critical properties at the transitions between the plateaus in the integer quantum Hall (IQH) effect has been elusive ever since [5,61]. These quantum phase transitions are famous examples of LD transitions driven by disorder. The diverging localization length plays the role of a correlation length in non-random continuous phase transitions, known to be described by conformal field theories in two dimensions (2D). It is natural to expect that effective (field) theories describing IQH plateau transitions should generally also possess conformal symmetry (see also Ref. [57,62]).

Many attempts have been made in the past to identify such an analytically tractable description of the IQH plateau transition and, more recently, Wess-Zumino (WZ) field theories defined on a certain supermanifold were conjectured to provide such a description [63- 66]. (Similar theories have also appeared in the context of string propagation in Anti-de Sitter space-time [67, 68].) These proposals focussed solely on bulk observables, i.e., on physical quantities measured in a sample without any boundaries. In this chapter, we highlight important new constraints that arise when one studies the scaling behavior of wave functions near the boundaries of a sample. Any proposed candidate theory for the plateau transitions will have to be consistent with our analysis of the numerical simulations (done by our collaborators, H. Obuse and A. Furusaki) for the boundary multifractal spectrum.

Work emerging [69, 70] from Ref. [63] led to the conjecture that the proposed theory would give rise to an exactly parabolic bulk multifractal spectrum for the IQH

transition,

$$\Delta_q^b = \gamma^b q(1-q), \tag{6.1}$$

reminiscent of analytically obtained multifractal spectra for Dirac fermions in, e.g., random abelian gauge potentials [10, 71]. In those models the parabolicity of the τ_q^b spectrum can be understood through a reformulation of the problem in terms of free fields.

Previous numerical studies [70] of wave function statistics at the IQH transition appeared to exhibit a bulk multifractal spectrum that was indeed well described (with an accuracy of $\sim 1\%$) by a parabolic fit (6.1) with $\gamma^b = 0.262 \pm 0.003$, seemingly providing support for the conjectures advanced in Ref. [63- 66]. (In Ref. [70] the results are presented in terms of $f^b(\alpha)$. For a parabolic multifractal spectrum such as the one in Eq. (6.1), $f^b(\alpha^b)$ is also parabolic, with a maximum at $\alpha_0^b = \gamma^b + 2$.)

Besides its conjectured relevance [63] to the IQH transition, the above-mentioned Wess-Zumino theory is known to describe transport properties of a disordered electronic system in a different universality class [72-74] (the chiral unitary 'Gade-Wegner' class AIII of [8, 7]) which possesses an additional discrete (chiral) symmetry [8], not present in microscopic models for the IQH transition. Well-known microscopic realizations of field theories in class AIII are random bipartite hopping models, and certain network models [72- 74, 75]. The theory possesses a line of fixed points, with continuously varying critical properties parametrized by the critical longitudinal DC conductivity. (It was argued in Ref. [63] that for a particular value of this continuous parameter the Wess-Zumino theory would provide a description of the IQH transition.)

Here we summarize results of numerical work done by our collaborators on the

multifractal exponents at the IQH transition both at a boundary (Δ_q^s) and in the bulk (Δ_q^b). Based on these numerical results quadratic behavior in q is ruled out for both quantities. Deviations from the parabolic form in Eq. (6.1) are found to be much larger in the multifractal exponents Δ_q^s at a boundary. Here it is important to note that in complete analogy to the bulk, the above conjectures would *also* yield a quadratic dependence on q of the *boundary* multifractal exponents Δ_q^s. The ratio Δ_q^s/Δ_q^b was also studied over a range of q. Accounting for this ratio is an important constraint on any proposed critical theory for the transition.

The multifractality of critical wave functions were studied in a way similar to Ref. [70], with the goal of numerically determining the rescaled anomalous exponents

$$\gamma_q^x = \Delta_q^x/q(1-q), \tag{6.2}$$

both for $x = s$ (boundary) and $x = b$ (bulk).

For the case of boundary exponents we consider the critical Chalker-Coddington network model [24] placed on a cylinder. The dynamics of wave functions on links of the network is governed by a unitary evolution operator U. For each disorder realization, U was numerically diagonalized. The details of the numerical work done by our collaborators can be found in Ref. [76]. The anomalous dimensions Δ_q^s were determined from the system size dependence of the boundary wave function intensity and its moments. Independently, α_q^s and $f^s(\alpha_q^s)$ were numerically obtained from $\overline{|\psi(\boldsymbol{r})|^{2q}\ln|\psi(\boldsymbol{r})|^2}/\overline{|\psi(\boldsymbol{r})|^{2q}} \sim -\alpha_q^s \ln L$, and $\ln\overline{|\psi(\boldsymbol{r})|^{2q}} \sim \left[f^s(\alpha_q^s) - \alpha_q^s q - D_s\right]\ln L$,.

We show in Fig. 6.1(a) the rescaled boundary anomalous dimension γ_q^s (red filled circles) obtained from the numerical analysis. We see clearly that γ_q^s is not constant, implying that the boundary multifractal spectrum Δ_q^s is *not parabolic*. The change in γ_q^s over the interval $0 < q \leqslant 1/2$ is about $4 \sim 5\%$ and is significantly larger than the
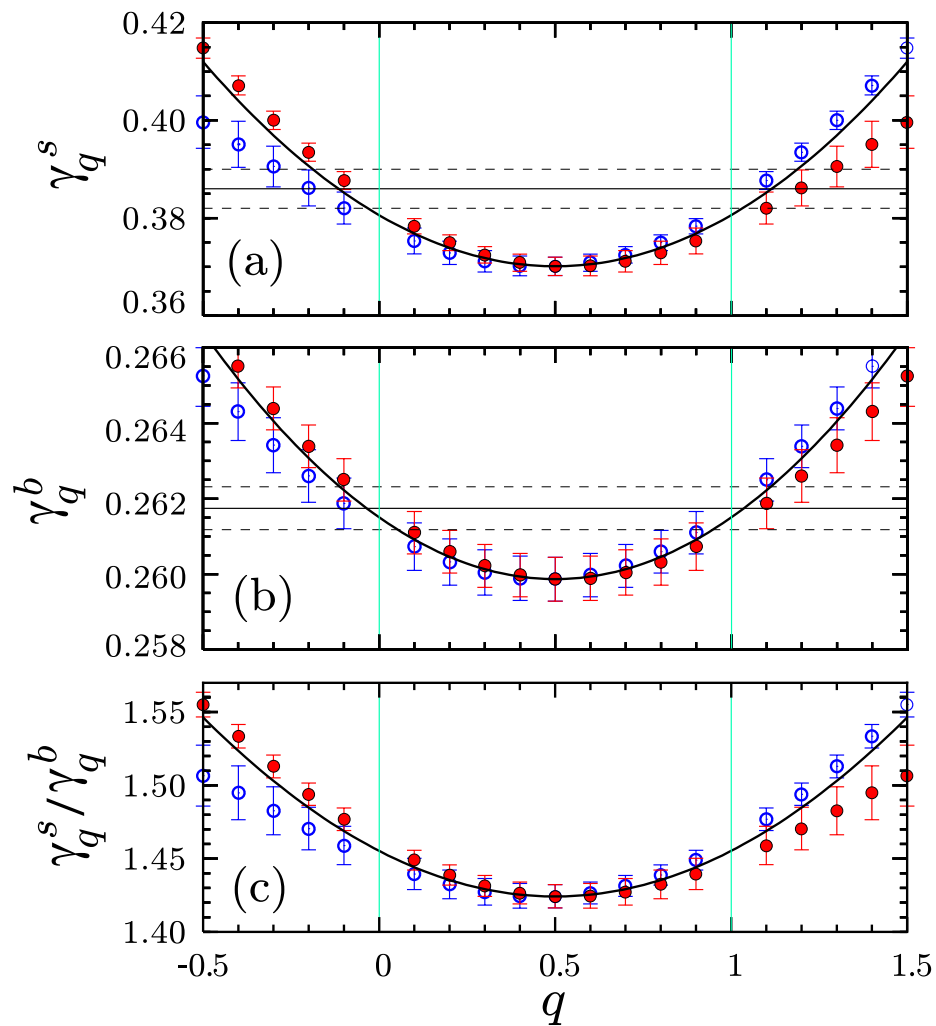
Figure 6.1: (a) Rescaled boundary multifractal exponents γ_q^s (●) and γ_{1-q}^s (○). The curve is $0.370 + 0.042(q - 1/2)^2$, obtained by fitting the data for γ_q^s in $0 < q < 1$ to a parabolic form. The horizontal solid line shows $\alpha_0^s - 2 = 0.386 \pm 0.004$ with error bars indicated by dashed lines, which is consistent with $\lim_{q \to 0,1} \gamma_q^s$. (b) Rescaled bulk multifractal exponents γ_q^b (●) and γ_{1-q}^b (○). The curve is $0.2599 + 0.0065(q - 1/2)^2$ obtained by fitting the data for γ_q^b in $0 < q < 1$ to a parabolic form. The horizontal solid line shows $\alpha_0^b - 2 = 0.2617 \pm 0.0006$ with error bars indicated by dashed lines. (c) Ratios γ_q^s/γ_q^b (●) and $\gamma_{1-q}^s/\gamma_{1-q}^b$ (○). As above, the curve is obtained from the parabolic fits for $\gamma_q^{s,b}$, which amounts to quartic approximations for $\Delta_q^{s,b}$.

error bars. This provides the strongest numerical evidence against the parabolicity of the multifractal exponents.

Shown in the same figure by blue open circles is the mirror image of γ_q^s with respect to $q = 1/2$, γ_{1-q}^s. We see that the symmetry relation Eq. (4.26) is satisfied within error bars for $0 \lesssim q \lesssim 1$. The rescaled anomalous dimension γ_q^s approaches $\alpha_0^s - 2$ (the horizontal line) at $q = 0, 1$, indicating that the two independent calculations of α_0^s and Δ_q^s are consistent. The bulk anomalous dimension Δ_q^b was also studied numerically using the Chalker-Coddington network model on a torus.

Fig. 6.1(b) shows the exponents γ_q^b, together with their mirror image. The symmetry relation Eq. (4.26) is again satisfied for $0 \lesssim q \lesssim 1$ within error bars, which provides confirmation that the numerical results are reliable. We see clearly that γ_q^b has q dependence, although it is weaker than that of γ_q^s; compare the vertical scales of Fig. 6.1(a) and (b).

The ratio γ_q^s/γ_q^b is shown in Fig. 6.1(c) and is seen to be clearly dependent on q. Any candidate theory for the IQH transition needs to be consistent with this ratio, and in particular its dependence on q. (Note that for a free field this ratio would be equal to 2, and independent of q [16, 12].)

Fig. 6.2(a) shows α_q^x as a function of q. The data significantly deviate from linear behavior that would result if Δ_q^x were strictly parabolic (constant γ_q^x). In Fig. 6.2(b) we show the corresponding singularity spectra $f^x(\alpha_q^x)$ as functions of q. (Combining the data from the two panels would result in $f^x(\alpha^x)$ as functions of α^x.) For $q \gtrsim 1.5$ where $f^s(\alpha^s) < 0$, the moments $\overline{|\psi(\boldsymbol{r})|^{2q}}$ are dominated by rare events, and thus accurate numerical calculation of multifractal exponents becomes more difficult [2]. This explains the discrepancy between the (red) data points and the solid curves for $q \gtrsim 1.5$ in Fig. 6.2. As $f_q^s > 0$ at $q \gtrsim -1$, we expect that the numerical results for $f^s(\alpha^s)$ should be more reliable at $q \approx -1$ than at $q \approx 1.5$, as evidenced by the
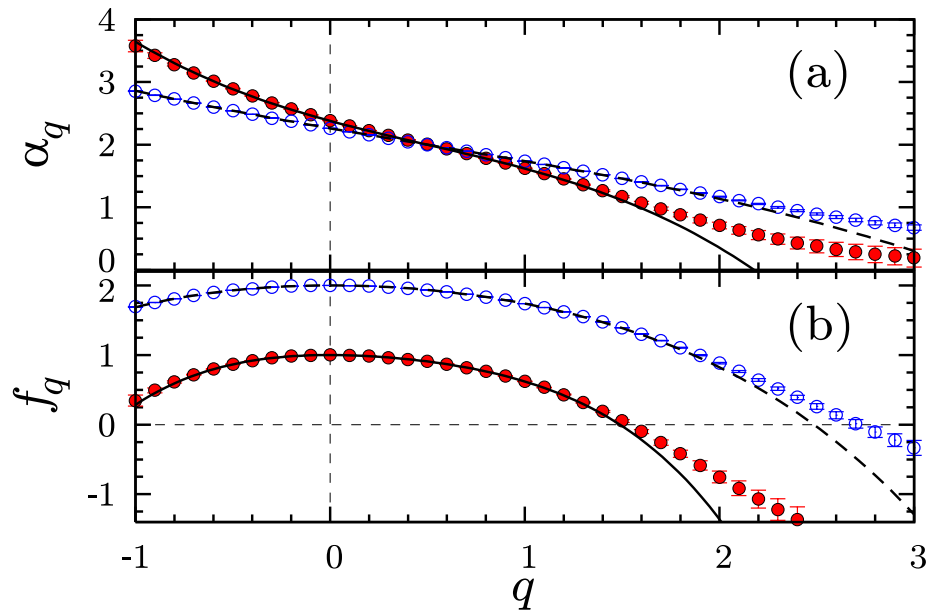
Figure 6.2: (a) α_q^s ($\bullet$) and α_q^b ($\circ$) as functions of q; (b) f_q^s ($\bullet$) and f_q^b ($\circ$) as functions of q. The solid and dashed curves on both panels are obtained from the parabolic approximations to γ_q^x (that is, quartic approximations to Δ_q^x). Notice that α_q^x significantly deviate from straight lines which would follow from strictly parabolic Δ_q^x (or constant γ_q^x).

agreement between the red dots and the solid curve in Fig. 6.2. The curve suggests termination of $f^s(\alpha^s)$ [2] to occur at $q \approx 2.2$.

These numerical results clearly demonstrate that both, the boundary and the bulk multifractal spectra, Δ_q^s and Δ_q^b, significantly deviate from parabolicity, and that their q-dependent ratio is significantly different from 2. (These conclusions were recently also reached, independently, by Evers, Mildenberger, and Mirlin [77].) These results for the bulk as well as the boundary multifractal spectra impose important constraints on any analytical theory for the IQH plateau transition.

Chapter 7

Multifractality and Entanglement Entropy

Entanglement is a unique feature of a quantum system and entanglement entropy, defined through the von Neumann entropy (vNE) measure, is one of the most widely used quantitative measures of entanglement [78-81]. Consider a composite system that can be partitioned into two subsystems A and B. The von Neumann entropy of either of the subsystems is $s_A = -\text{Tr}_A \rho_A \ln \rho_A = s_B = -\text{Tr}_B \rho_B \ln \rho_B$. Here, the reduced density matrix ρ_A is obtained by tracing over the degrees of freedom in B: $\rho_A = \text{Tr}_B |\psi_{AB}\rangle\langle\psi_{AB}|$ and similarly for ρ_B. In general, for a pure state $|\psi_{AB}\rangle$ of a composite system, the reduced density matrix is a mixture, and the corresponding entropy is a good measure of entanglement.

The scaling behavior of entanglement entropy is a particularly useful characterization near a quantum phase transition [80]. The entanglement entropy can show nonanalyticity at the phase transition even when the ground state energy (the quantum analog of the classical free energy) is analytic. While these ideas have been studied in a number of translation-invariant models [79, 80, 82], there have been far fewer investigations of random quantum critical points (for notable exceptions, see [83, 84]). Here we study von Neumann entropy at the Anderson transition in 3D and the IQH plateau transition. Von Neumann entropy will be shown to exhibit nonanalyticity at these transitions and a scaling behavior. At the outset, it should be emphasized that because of the single particle and disorder-dominated nature of these quantum phase transitions, entanglement as characterized by von Neumann entropy and its critical scaling behavior are fundamentally different from those calculated for interacting systems. This statement will be made more precise later.

75

Near the LD transition, the generalized inverse participation ratios, P_q obey,

$$P_q(E) \equiv \sum_r \overline{|\psi_E(r)|^{2q}} \sim L^{-\tau_q} \mathcal{F}_q\big[(E - E_C)L^{1/\nu}\big]. \qquad (7.1)$$

Here, L is the system size, ν is the exponent characterizing the divergence of correlation length, $\xi_E \sim |E - E_C|^{-\nu}$. This is a generalized version of Eq. (2.2) valid when we move away from the LD critical point by studying wave functions at different energy E. $\mathcal{F}_q(x)$ is a scaling function with $\mathcal{F}_q(x \to 0) = 1$ close to the critical point $E = E_C$. When E is tuned away from E_C, the system either tends towards an ideal metallic state with $P_q(E) \sim L^{-d(q-1)}$ (d being the number of spatial dimensions) or becomes localized with $P_q(E)$ independent of L.

Below, we first show that the disorder-averaged von Neumann entropy can be expressed as a derivative of P_q and thus, its scaling behavior follows from multifractal analysis. After that, we apply our formalism to understand the numerical results on von Neumann entropy at the three dimensional Anderson localization transition and the IQH plateau transition. Von Neumann entropy in the Anderson localization problem was studied previously [81,85], but the connection with mulitfractality and the unique features of von Neumann entropy at these quantum phase transitions have not been clearly elucidated.

7.1 Entanglement entropy near LD transitions

Even though the disorder induced localization problem can be studied in a single particle quantum mechanics language, there is no obvious way to define entanglement entropy in this picture. However (see Ref. [86]), entanglement can be defined using the site occupation number basis in the second-quantized Fock space. Let us divide

the lattice of linear size L into two regions, A and B. A single particle eigenstate of a lattice Hamiltonian at energy E is represented in the site occupation number basis as

$$|\psi_E\rangle = \sum_{r \in A c_\uparrow B} \psi_E(r) \, |1\rangle_r \bigotimes_{r' \neq r} |0\rangle_{r'} \tag{7.2}$$

Here $\psi_E(r)$ is the normalized single particle wave function at site r and $|n\rangle_r$ denotes a state having n particles at site r. We decompose the above sum over lattice sites r into the mutually orthogonal terms,

$$|\psi_E\rangle = |1\rangle_A \otimes |0\rangle_B + |0\rangle_A \otimes |1\rangle_B \tag{7.3}$$

where

$$|1\rangle_A = \sum_{r \in A} \psi_E(r)|1\rangle_r \bigotimes_{r' \neq r} |0\rangle_{r'}, \ |0\rangle_A = \bigotimes_{r \in A} |0\rangle_r \tag{7.4}$$

with analogous expressions for the $|1\rangle_B$ and $|0\rangle_B$ states. Notice that these states have the normalization

$$\langle 0|0\rangle_A = \langle 0|0\rangle_B = 1, \ \langle 1|1\rangle_A = p_A, \ \langle 1|1\rangle_B = p_B, \tag{7.5}$$

where

$$p_A = \sum_{r \in A} |\psi_E(r)|^2, \tag{7.6}$$

and similarly for p_B with $p_A + p_B = 1$.

To obtain the reduced density matrix ρ_A, we trace out the Hilbert space over B

in the density matrix $\rho = |\psi_E\rangle\langle\psi_E|$. This gives,

$$\rho_A = |1\rangle_A\langle 1| + p_B|0\rangle_A\langle 0|. \tag{7.7}$$

The corresponding von Neumann entropy is given by

$$s_A = -p_A \ln p_A - p_B \ln p_B. \tag{7.8}$$

In the above equation, we see that manifestly $s_A = s_B$. More importantly, s_A is bounded between 0 and $\ln 2$ for any eigenstate. This is in sharp contrast to the entanglement entropy in interacting quantum systems where it can be arbitrarily large near the critical point. The reason for this is also clear: Even though we used a second-quantized language, we are dealing with a single particle state rather than a many body correlated state. Consequently, the entanglement entropy does not grow arbitrarily large as a function of the size of A.

We also observe that at criticality, if the whole system size becomes very large in comparison with the subsystem A, we can restrict the subsystem to be a single lattice site and study the scaling dependence with respect to the overall system size L. Then, using the ansatz of scale invariance, we can always find the scaling of the entanglement as a function of the subsystem size l since near criticality, only the dimensionless ratio L/l can enter any physical quantity. To extract scaling, we find the bipartite entanglement of a single site r with the rest of the system and sum this over all lattice sites in the system. Using Eq. (7.8), we write this as

$$S(E) = -\sum_{r \in L^d} \left\{ |\psi_E(r)|^2 \ln |\psi_E(r)|^2 + \left[1 - |\psi_E(r)|^2\right] \ln \left[1 - |\psi_E(r)|^2\right] \right\}. \tag{7.9}$$

To leading order, the second term inside the square bracket in Eq. (7.9) can be dropped since $|\psi_E(r)|^2 \ll 1$ at all points r when the states are close to the critical energy. We can readily relate the disorder average (denoted by overbar) of this entropy to the multifractal scaling in Eq. (7.1) and get the L scaling as

$$\overline{S}(E) \approx -\frac{dP_q}{dq}\bigg|_{q=1} \approx \frac{d\tau_q}{dq}\bigg|_{q=1} \ln L - \frac{\partial \mathcal{F}_q}{\partial q}\bigg|_{q=1}. \tag{7.10}$$

We do not know the general form of the scaling function $\mathcal{F}_q$, but we can get the approximate L dependence of the entropy in various limiting cases. For the exactly critical case when $\mathcal{F}_q \equiv 1$ for all values of q, we get

$$\overline{S}(E) \sim \alpha_1 \ln L, \tag{7.11}$$

where the constant $\alpha_1 = d\tau_q/dq|_{q=1}$ is unique for each universality class. From the discussion following Eq. (7.1), the leading scaling behavior of $\overline{S}(E)$ in the ideal metallic and localized states is given by $d \ln L$ and $\alpha_1 \ln \xi_E$, respectively. From the limiting cases, we see that, in general, $\overline{S}(E)$ has the approximate form

$$\overline{S}(E) \sim \mathcal{K}[(E - E_C)L^{1/\nu}] \ln L, \tag{7.12}$$

where the coefficient function $\mathcal{K}(x)$ decreases from d in the metallic state to α_1 at criticality and then drops to zero for the localized state. We will see that this scaling form is verified in numerical simulations done by our collaborators.

7.2 Entanglement in the 3D Anderson model

The scaling form for the entanglement entropy averaged over all eigenstates of the single particle Hamiltonian is also of interest since this scaling can change as a function of disorder strength. To be specific, let us consider the 3D Anderson model on a cubic lattice. The Hamiltonian is

$$H = \sum_i V_i c_i^\dagger c_i - t \sum_{\langle i,j \rangle} (c_i^\dagger c_j + H.c.), \qquad (7.13)$$

where $c_i^\dagger (c_i)$ is the fermionic creation (annihilation) operator at site i of the lattice, and the second sum is over all nearest neighbors. We set $t = 1$, and the V_i are random variables uniformly distributed in the range $[-W/2, W/2]$. It is known [87] that as W is decreased from a very high value, extended states appear at the band center below the critical disorder strength $W_c = 16.3$, and a recent work [88] reported the localization length exponent $\nu = 1.57 \pm 0.03$.

The analysis leading to Eq. (7.12) also holds when we study wave functions at a single energy, say $E = 0$ and increase the disorder strength in the Anderson model across the critical value W_c. In this case, the states at $E = 0$ evolve continuously from fully metallic to critical and then finally localized, resulting in the approximate form for the entanglement entropy as

$$\overline{S}(E = 0, w, L) \sim \mathcal{C}(wL^{1/\nu}) \ln L, \qquad (7.14)$$

where $w = (W - W_c)/W_c$ is the normalized relative disorder strength and $\mathcal{C}(x)$ is a scaling function. In particular, as mentioned before, $\mathcal{C}(x) \to d$ as $w \to -1$, $\mathcal{C}(x) \to 0$ as $w \to \infty$, and $\mathcal{C}(x) = \alpha_1$ when $w = 0$.
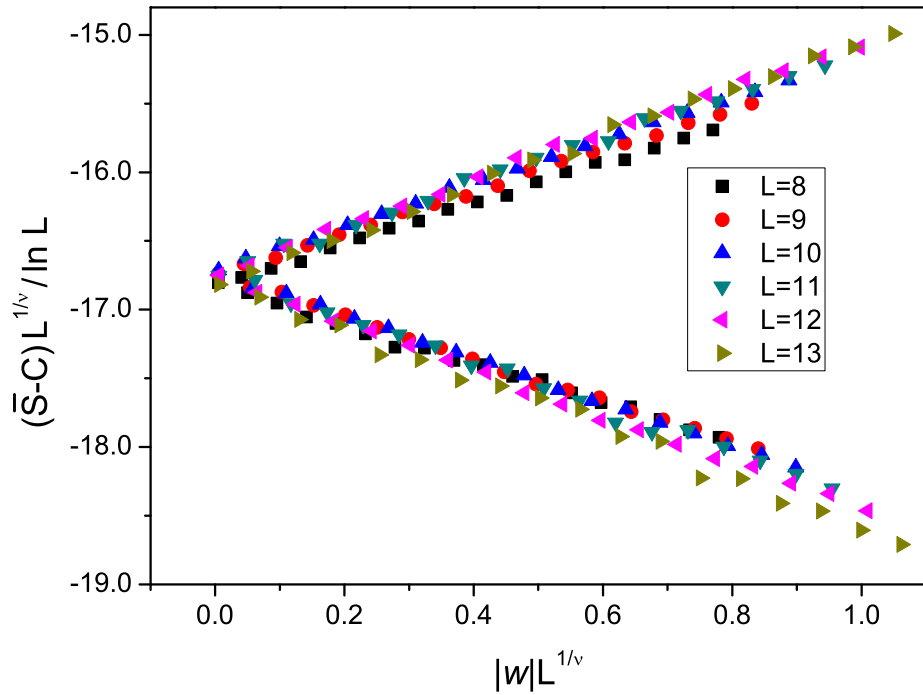
Figure 7.1: Scaling curve for the entanglement entropy in the 3D Anderson model. With the choice of $\nu = 1.57$ and $C = 12.96$, all data collapse to a universal functions $f_\pm(x)$. The two branches correspond to $w < 0$ and $w > 0$.

Next, we look at the energy-averaged entropy. We average Eq. (7.10) over the entire band of energy eigenvalues and construct the von Neumann entropy,

$$\overline{S}(w, L) = \frac{1}{L^3} \sum_E \overline{S}(E, w, L), \tag{7.15}$$

where L^3 is also the total number of states in the band. Then using Eqs. (7.12) and (7.14), one can show that close to $w = 0$,

$$\overline{S}(w, L) \sim C + L^{-1/\nu} f_\pm\left(wL^{1/\nu}\right) \ln L, \tag{7.16}$$

where C is an L *independent* constant, and $f_\pm(x)$ are two universal functions corresponding to the two regimes $w > 0$ and $w < 0$.
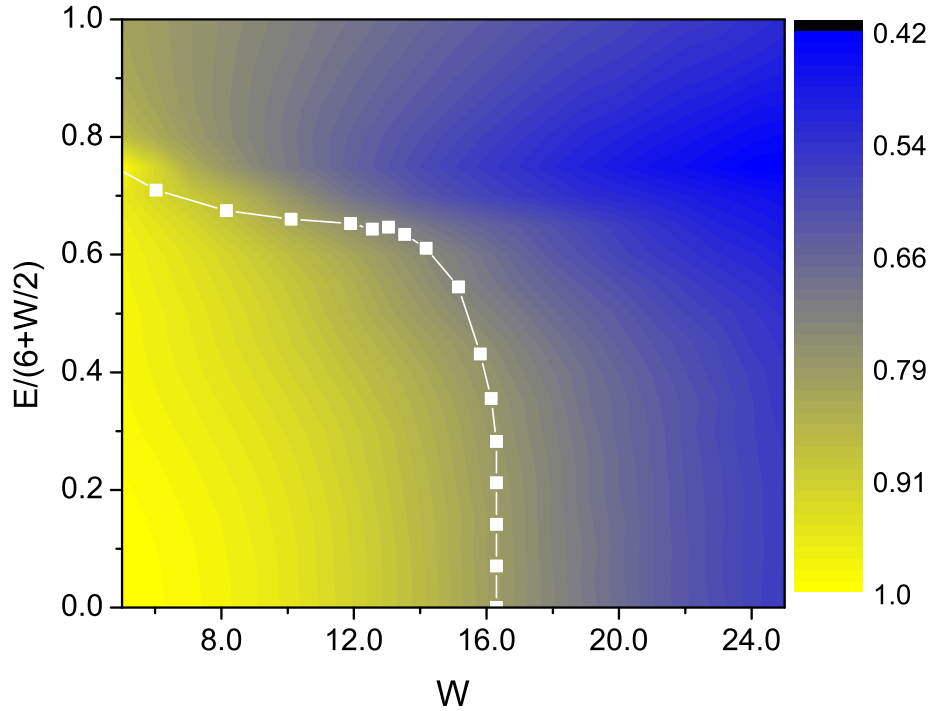
Figure 7.2: Entanglement entropy $\overline{S}(E, W, L)$ as a function of energy E and disorder strength W computed in a system with $L = 10$. The square shows the mobility edge reported in Ref. [91]. Because of the finiteness of the system, the transition from the localized to the delocalized region is smooth.

We now apply the above analysis to the numerical simulations done by our collaborators Xun Jia and Sudip Chakravarty. The Hamiltonian Eq. (7.13) was diagonalized numerically in a finite $L \times L \times L$ system with periodic boundary conditions. The scaling form of $\overline{S}(w, L)$ is given by Eq. (7.16). Fig. 7.1 shows the results of the data collapse with a choice of $\nu = 1.57$, and the non-universal constant $C = 12.96$ is determined by an algorithm described in Ref. [89]. The successful data collapse reflects the non-analyticity of the von Neumann entropy and accuracy of the multifractal analysis.

Then the transfer matrix method [90] is used to study the energy dependence of $\overline{S}(E, w, L)$ by considering a quasi-one-dimensional (quasi-1D) system with a size of $(mL) \times L \times L$, $m \gg 1$. A typical $\overline{S}(E, W, L)$ with $L = 10$ is shown in Fig. 7.2. The
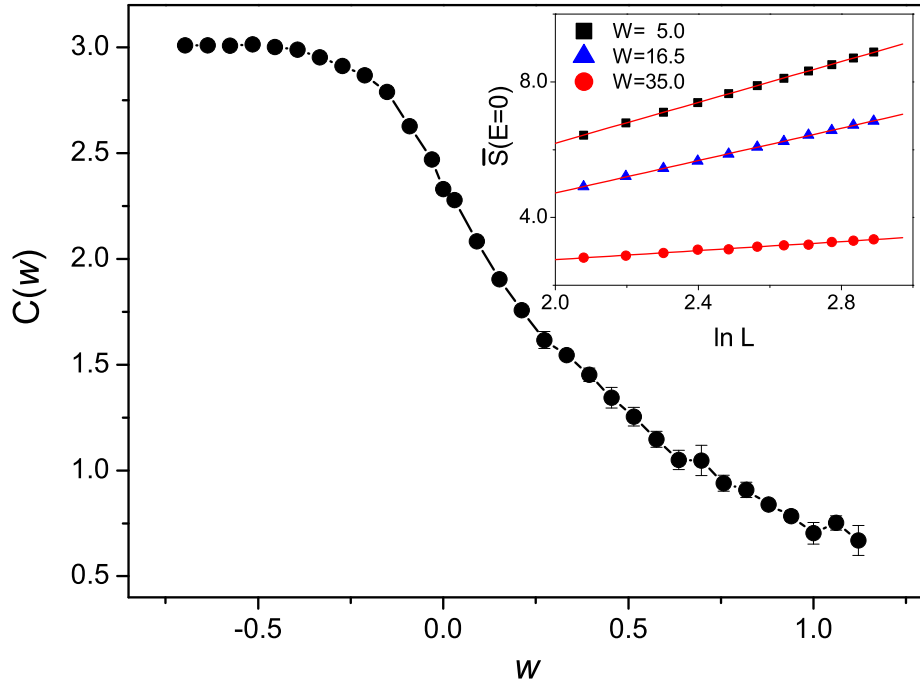
Figure 7.3: The quantity $\mathcal{C}$ in Eq. (7.14). The range of the system sizes is too small to observe the weak L dependence. Inset: $\overline{S}(E = 0, W, L)$ as a function of $\ln L$ for three different W.

value of $\overline{S}(E, W, L)$ is normalized by $\ln(L^3)$ such that $\overline{S} \to 1$ in a fully extended state. The energy E is normalized by $(W/2+6)$, which is the energy range of nonzero density of states [92]. The mobility edge computed in Ref. [91] is also plotted in Fig. 7.2. The validity of the scaling form in Eq. (7.14) is seen in Fig. 7.3. In particular, the function $\mathcal{C}(x)$ shows the expected behavior.

7.3 Entanglement in the IQH system

We now consider now the second example, the integer quantum Hall system in a magnetic field B which was again numerically simulated by our collaborators. The computation of the von Neumann entropy for a given eigenstate follows the same procedure described for the Anderson localization. The von Neumann entropy $\overline{S}(E, L)$ is
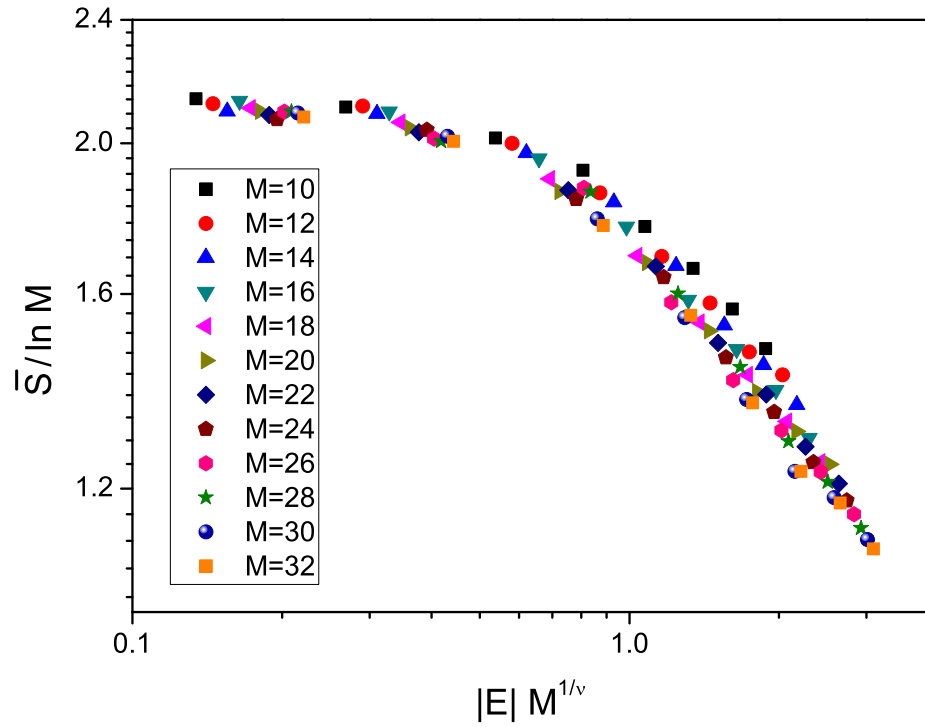
Figure 7.4: Scaling of the von Neumann entropy $\overline{S}(E)$ for the IQHE. M stands for the linear system size. The data collapse with the accepted value of $\nu = 2.33$.

obtained at a particular energy E. The scaling form of $\overline{S}(E, L)$ is given by Eq. (7.12) with $E_C = 0$ and is $\overline{S}(E, L) = \mathcal{K}(|E|L^{1/\nu}) \ln L$. A good agreement with numerical simulations is seen in Fig. 7.4.

Chapter 8

Conclusions and Outlook

In this thesis, we have introduced the concept of boundary multifractality at LD transitions and studied it both from a general perspective and also at various specific LD critical points. New features specific to boundary criticality were discussed. Analytical predictions were confronted with numerical simulations and excellent agreement was found in all the cases considered.

One of the motivations to study boundary multifractality at two dimensional LD transitions was that it might provide insights into the unsolved critical theories for the IQH plateau transition and the symplectic transition. Our work clearly demonstrates that possible candidates for these critical theories would be quite distinct from various simple free field based theories many of which have the ratio of boundary to bulk critical exponents as two. Infact, ongoing work seems to confirm this to be the case with Dirac fermions in random gauge fields. In this case, the problem has a free field based formulation. An important challenge is to identify 2D conformal field theories which are plausible candidates for LD critical points (having supersymmetry, non-unitarity etc.) and at the same time have a ratio of the boundary exponents to bulk exponents different from two. The numerical analysis done jointly with our collaborators indicates that the critical theories should also have a non-parabolic multifractal spectrum which is not typically the case with free-field based formulations of LD critical points.

Another important future line of research is to broaden the scope of boundary multifractality outside the domain of LD transitions. Multifractality is a very general scaling behavior observed in a wide variety of physical systems such as in random magnets and turbulence. One can systematically analyze boundary effects on multi-

fractality in these problems. Given the rich features discovered at different LD critical points when boundary multifractality was studied, it will not be surprising if the same holds true in these other problems too.

Appendix A

Representations of sl(2|1) Superalgebra

In this appendix, we list relevant features of sl(2|1) superalgebra representations that are useful in studying the spin quantum Hall critical point, both in the bulk and at the boundary.

The sl(2|1) superalgebra has eight generators, of which four are bosonic (B, Q_3, Q_+, Q_-) and four are fermionic (V_+, V_-, W_+, W_-). We use the convention of Ref. [93] for the generators. These satisfy the same commutation ([,]) and anticommutation ({, }) relations as the generators of osp(2|2) superalgebra:

$$[B, Q_3] = [B, Q_\pm] = 0,$$

$$[B, V_\pm] = \frac{1}{2}V_\pm, \qquad\qquad [B, W_\pm] = -\frac{1}{2}W_\pm,$$

$$[Q_3, Q_\pm] = \pm Q_\pm, \qquad\qquad [Q_+, Q_-] = 2Q_3,$$

$$[Q_3, V_\pm] = \pm\frac{1}{2}V_\pm, \qquad\qquad [Q_3, W_\pm] = \pm\frac{1}{2}W_\pm,$$

$$[Q_+, V_-] = V_+, \qquad\qquad [Q_+, W_-] = W_+,$$

$$[Q_-, V_+] = V_-, \qquad\qquad [Q_-, W_+] = W_-,$$

$$[Q_+, V_+] = [Q_+, W_+] = [Q_-, V_-] = [Q_-, W_-] = 0,$$

$$\{V_+, V_-\} = \{W_+, W_-\} = 0,$$

$$\{V_+, W_+\} = Q_+, \quad \{V_+, W_-\} = B - Q_3,$$

$$\{V_-, W_-\} = -Q_-, \quad \{V_-, W_+\} = -B - Q_3. \tag{A.1}$$

An important subalgebra is gl(1|1) formed by the generators (B, Q_3, V_-, W_+). This is the SUSY present in the SQH network at finite broadening γ, when $z = e^{-\gamma} < 1$ [see Eqs. (3.4) and (3.5)], as well as at an absorbing boundary.
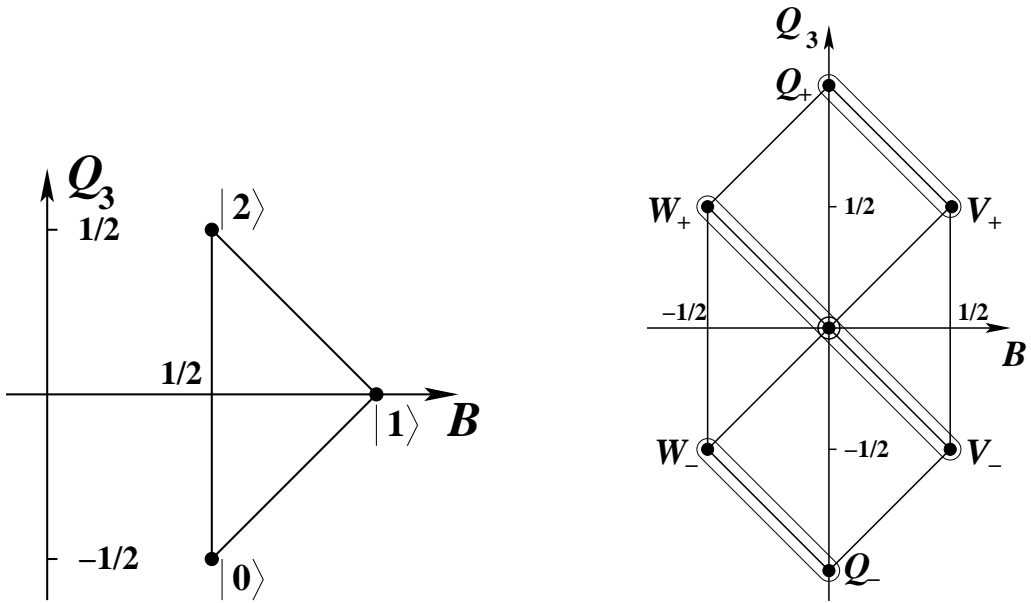
Figure A.1: Weight diagrams of sl(2|1). We show two doublets and the adjoint of the subalgebra gl(1|1) in the adjoint representation diagram.

The sl(2|1) algebra has an oscillator realization formed by bilinear combinations of the fermion and boson operators on each link that are SU(2) singlets. For the up-links the oscillator representation is:

$$Q_3 = \frac{1}{2}(f_\uparrow^\dagger f_\uparrow + f_\downarrow^\dagger f_\downarrow - 1),$$

$$Q_+ = f_\uparrow^\dagger f_\downarrow^\dagger, \qquad Q_- = f_\downarrow f_\uparrow,$$

$$B = \frac{1}{2}(b_\uparrow^\dagger b_\uparrow + b_\downarrow^\dagger b_\downarrow + 1),$$

$$V_+ = \frac{1}{\sqrt{2}}(b_\uparrow^\dagger f_\downarrow^\dagger - b_\downarrow^\dagger f_\uparrow^\dagger),$$

$$V_- = -\frac{1}{\sqrt{2}}(b_\uparrow^\dagger f_\uparrow + b_\downarrow^\dagger f_\downarrow),$$

$$W_+ = \frac{1}{\sqrt{2}}(f_\uparrow^\dagger b_\uparrow + f_\downarrow^\dagger b_\downarrow),$$

$$W_- = \frac{1}{\sqrt{2}}(b_\uparrow f_\downarrow - b_\downarrow f_\uparrow). \tag{A.2}$$

These operators act irreducibly in the fundamental three-dimensional representation of sl(2|1) (denoted by **3**) with the space of states spanned by three SU(2) singlet states which we denote as $|m\rangle$, $m = 0, 1, 2$:

$$|0\rangle = |\text{vacuum}\rangle, \tag{A.3}$$

$$|1\rangle = V_+|0\rangle = \frac{1}{\sqrt{2}}(b_\uparrow^\dagger f_\downarrow^\dagger - b_\downarrow^\dagger f_\uparrow^\dagger)|0\rangle, \tag{A.4}$$

$$|2\rangle = Q_+|0\rangle = f_\uparrow^\dagger f_\downarrow^\dagger|0\rangle. \tag{A.5}$$

We need the matrix elements of the sl(2|1) generators between the states in **3**. The non-zero matrix elements are easy to find from the following equations giving the action of the generators on the states:

$$
\begin{array}{lll}
Q_3|0\rangle = -\dfrac{1}{2}|0\rangle, & Q_3|1\rangle = 0, & Q_3|2\rangle = \dfrac{1}{2}|2\rangle, \\[2mm]
B|0\rangle = \dfrac{1}{2}|0\rangle, & B|1\rangle = |1\rangle, & B|2\rangle = \dfrac{1}{2}|2\rangle, \\[2mm]
Q_+|0\rangle = |2\rangle, & Q_-|2\rangle = |0\rangle, & \\[2mm]
V_+|0\rangle = |1\rangle, & V_-|2\rangle = -|1\rangle, & \\[2mm]
W_+|1\rangle = |2\rangle, & W_-|1\rangle = |0\rangle. &
\end{array}
\tag{A.6}
$$

These equations give us the matrices of the generators of sl(2|1) in the fundamental representation (for a generator G the matrix elements G_{ij}, $i, j = 1, 2, 3$, are defined

by $G|i\rangle = \sum_j G_{ji}|j\rangle$):

$$B = \begin{pmatrix} 1/2 & 0 & 0 \\ 0 & 1 & 0 \\ 0 & 0 & 1/2 \end{pmatrix}, \qquad Q_3 = \begin{pmatrix} -1/2 & 0 & 0 \\ 0 & 0 & 0 \\ 0 & 0 & 1/2 \end{pmatrix},$$

$$Q_+ = \begin{pmatrix} 0 & 0 & 0 \\ 0 & 0 & 0 \\ 1 & 0 & 0 \end{pmatrix}, \qquad Q_- = \begin{pmatrix} 0 & 0 & 1 \\ 0 & 0 & 0 \\ 0 & 0 & 0 \end{pmatrix},$$

$$V_+ = \begin{pmatrix} 0 & 0 & 0 \\ 1 & 0 & 0 \\ 0 & 0 & 0 \end{pmatrix}, \qquad W_- = \begin{pmatrix} 0 & 1 & 0 \\ 0 & 0 & 0 \\ 0 & 0 & 0 \end{pmatrix},$$

$$V_- = \begin{pmatrix} 0 & 0 & 0 \\ 0 & 0 & -1 \\ 0 & 0 & 0 \end{pmatrix}, \qquad W_+ = \begin{pmatrix} 0 & 0 & 0 \\ 0 & 0 & 0 \\ 0 & 1 & 0 \end{pmatrix}. \tag{A.7}$$

In Fig. A.1 we give the weight diagrams for the fundamental and adjoint representations which are useful for understanding some of our arguments.

For the down-links the construction is similar. The oscillator realization of the

sl(2|1) generators is now

$$\bar{Q}_3 = \frac{1}{2}(\bar{f}_\uparrow^\dagger \bar{f}_\uparrow + \bar{f}_\downarrow^\dagger \bar{f}_\downarrow + 1),$$

$$\bar{Q}_+ = \bar{f}_\downarrow \bar{f}_\uparrow, \qquad \bar{Q}_- = \bar{f}_\uparrow^\dagger \bar{f}_\downarrow^\dagger,$$

$$\bar{B} = -\frac{1}{2}(\bar{b}_\uparrow^\dagger \bar{b}_\uparrow + \bar{b}_\downarrow^\dagger \bar{b}_\downarrow + 1),$$

$$\bar{V}_+ = \frac{1}{\sqrt{2}}(\bar{b}_\downarrow \bar{f}_\uparrow - \bar{b}_\uparrow \bar{f}_\downarrow),$$

$$\bar{V}_- = \frac{1}{\sqrt{2}}(\bar{f}_\uparrow^\dagger \bar{b}_\uparrow + \bar{f}_\downarrow^\dagger \bar{b}_\downarrow),$$

$$\bar{W}_+ = -\frac{1}{\sqrt{2}}(\bar{b}_\uparrow^\dagger \bar{f}_\uparrow + \bar{b}_\downarrow^\dagger \bar{f}_\downarrow),$$

$$\bar{W}_- = \frac{1}{\sqrt{2}}(\bar{b}_\downarrow^\dagger \bar{f}_\uparrow^\dagger - \bar{b}_\uparrow^\dagger \bar{f}_\downarrow^\dagger). \tag{A.8}$$

These operators satisfy the same commutation relations as the ones on the up-links and act in the three-dimensional space spanned by the SU(2) singlets

$$|\bar{0}\rangle = |\text{vacuum}\rangle,$$

$$|\bar{1}\rangle = -\bar{W}_-|\bar{0}\rangle = \frac{1}{\sqrt{2}}(\bar{b}_\uparrow^\dagger \bar{f}_\downarrow^\dagger - \bar{b}_\downarrow^\dagger \bar{f}_\uparrow^\dagger)|\bar{0}\rangle,$$

$$|\bar{2}\rangle = -\bar{Q}_-|0\rangle = -\bar{f}_\uparrow^\dagger \bar{f}_\downarrow^\dagger|\bar{0}\rangle. \tag{A.9}$$

These singlets form the representation $\bar{\mathbf{3}}$ of the sl(2|1) algebra dual to the fundamental $\mathbf{3}$. Note that the state $|\bar{1}\rangle$ contains odd number of fermions, and, therefore, has negative square norm:

$$\langle \bar{1}|\bar{1}\rangle = -1. \tag{A.10}$$

The action of the generators on the states in the representation $\bar{\mathbf{3}}$ is easily found

to be

$$\bar{Q}_3|\bar{0}\rangle = \frac{1}{2}|\bar{0}\rangle, \qquad \bar{Q}_3|\bar{1}\rangle = 0, \qquad \bar{Q}_3|\bar{2}\rangle = -\frac{1}{2}|\bar{2}\rangle,$$

$$\bar{B}|\bar{0}\rangle = -\frac{1}{2}|\bar{0}\rangle, \qquad \bar{B}|\bar{1}\rangle = -|\bar{1}\rangle, \qquad \bar{B}|\bar{2}\rangle = -\frac{1}{2}|\bar{2}\rangle,$$

$$\bar{Q}_+|\bar{2}\rangle = -|\bar{0}\rangle, \qquad \bar{Q}_-|\bar{0}\rangle = -|\bar{2}\rangle,$$

$$\bar{V}_+|\bar{1}\rangle = |\bar{0}\rangle, \qquad \bar{V}_-|\bar{1}\rangle = -|\bar{2}\rangle,$$

$$\bar{W}_+|\bar{2}\rangle = -|\bar{1}\rangle, \qquad \bar{W}_-|\bar{0}\rangle = -|\bar{1}\rangle. \tag{A.11}$$

This gives the matrices for the generators in $\bar{\mathbf{3}}$:

$$\bar{B} = \begin{pmatrix} -1/2 & 0 & 0 \\ 0 & -1 & 0 \\ 0 & 0 & -1/2 \end{pmatrix}, \qquad \bar{Q}_3 = \begin{pmatrix} 1/2 & 0 & 0 \\ 0 & 0 & 0 \\ 0 & 0 & -1/2 \end{pmatrix},$$

$$\bar{Q}_+ = \begin{pmatrix} 0 & 0 & -1 \\ 0 & 0 & 0 \\ 0 & 0 & 0 \end{pmatrix}, \qquad \bar{Q}_- = \begin{pmatrix} 0 & 0 & 0 \\ 0 & 0 & 0 \\ -1 & 0 & 0 \end{pmatrix},$$

$$\bar{V}_+ = \begin{pmatrix} 0 & 1 & 0 \\ 0 & 0 & 0 \\ 0 & 0 & 0 \end{pmatrix}, \qquad \bar{W}_- = \begin{pmatrix} 0 & 0 & 0 \\ -1 & 0 & 0 \\ 0 & 0 & 0 \end{pmatrix},$$

$$\bar{V}_- = \begin{pmatrix} 0 & 0 & 0 \\ 0 & 0 & 0 \\ 0 & -1 & 0 \end{pmatrix}, \qquad \bar{W}_+ = \begin{pmatrix} 0 & 0 & 0 \\ 0 & 0 & -1 \\ 0 & 0 & 0 \end{pmatrix}. \tag{A.12}$$

Appendix B

Boundary Supersymmetry at the Spin Quantum Hall Transition

We demonstrate in this appendix that the introduction of a reflecting boundary preserves the full sl(2|1) supersymmetry (SUSY) at the spin quantum Hall critical point.

First we note some useful relations satisfied by the bosons and fermions defined in Sec. 3.3. For any function F, all bosons and fermions (denoted by $c, c^\dagger$) except the negative norm ones satisfy the commutation relations,

$$
[c, :F(c^\dagger, c):] =: \frac{\overrightarrow{\partial}}{\partial c^\dagger} F(c^\dagger, c):,
$$
$$
\left[c^\dagger, :F(c^\dagger, c):\right] = -:F(c^\dagger, c)\frac{\overleftarrow{\partial}}{\partial c}:,
$$
(B.1)

where the : : denotes normal ordering. The negative norm operators satisfy,

$$
[c, :F(c^\dagger, c):] = -: \frac{\overrightarrow{\partial}}{\partial c^\dagger} F(c^\dagger, c):,
$$
$$
\left[c^\dagger, :F(c^\dagger, c):\right] =:F(c^\dagger, c)\frac{\overleftarrow{\partial}}{\partial c}: .
$$
(B.2)

One can first write the transfer matrix for a single A node in the bulk [94]. Since the scattering at the node is diagonal in spin indices [see Eq. (3.1)], the node transfer matrices are products of two independent transfer matrices for each spin direction:

$$
T_A = \prod_{\sigma=\uparrow,\downarrow} T_{A\sigma} = T_{A\uparrow}T_{A\downarrow}.
$$
(B.3)

where

$$T_{A\sigma} = \exp\left(t_{A\sigma}(f_\sigma^\dagger \vec{f}_\sigma^\dagger + b_\sigma^\dagger \vec{b}_\sigma^\dagger)\right)(1 - t_{A\sigma}^2)^{\frac{1}{2}n_\sigma}$$

$$\times \exp\left(-t_{A\sigma}(\bar{f}_\sigma f_\sigma + \bar{b}_\sigma b_\sigma)\right), \tag{B.4}$$

$$n_\sigma = n_{f\sigma} + n_{b\sigma} + n_{\bar{f}\sigma} + n_{\bar{b}\sigma}. \tag{B.5}$$

Let us also introduce the following notation:

$$T_+ = \prod_\sigma \exp\left(t_{A\sigma}(f_\sigma^\dagger \vec{f}_\sigma^\dagger + b_\sigma^\dagger \vec{b}_\sigma^\dagger)\right), \tag{B.6}$$

$$T_0 = \prod_\sigma (1 - t_{A\sigma}^2)^{\frac{1}{2}n_\sigma}, \tag{B.7}$$

$$T_- = \prod_\sigma \exp\left(-t_{A\sigma}(\bar{f}_\sigma f_\sigma + \bar{b}_\sigma b_\sigma)\right), \tag{B.8}$$

so that $T_A = T_+ T_0 T_-$.

The three terms correspond respectively to the creation, propagation and destruction of boson and fermions on evolution along the vertical direction. Similar expressions can also be written for the B nodes. In the spin-rotation invariant case, using the relations in Eqs. (B.1) and (B.2), for any *particular* realization of the disorder in the scattering matrices, it can be checked that each node transfer matrix in Eq. (B.3) commutes with the sum of the eight generators of the superalgebra sl(2|1) $\cong$ osp(2|2) (see Appendix A) defined on the up link and down link on which the node transfer matrix acts.

Having defined the bulk node transfer matrices, we now consider the network on a semi-infinite half-plane with a fully reflecting boundary either along the horizontal direction or the vertical direction. Although it is clear that physical quantities cannot depend on whether the boundary is defined along the horizontal or the vertical di-

rection, the two cases have to be studied very differently within the second-quantized formalism. This is because of the fact that we have singled out the vertical direction as time and the tensor product of Fock spaces on which U_A and U_B act is defined along a particular horizontal row of links. For definiteness, let us assume that the boundary is always composed of A nodes.

We first consider the case of a reflecting boundary along the vertical (time) direction as shown in Fig. 3.1. In this case, we retain the periodic boundary condition along the time direction and hence also the supertrace STr in the correlation functions. Only the node transfer matrices on the boundary have to be changed to account for the complete reflection at the boundary. This can be implemented by setting $t_A = 0$ in Eq. (B.4). In this case, the boundary node transfer matrix reduces to the trivial identity operator. Consequently the operators U_A and U_B still commute with all generators of the sl(2|1) superalgebra.

As mentioned before, we could have equivalently chosen the boundary to be along the horizontal space direction, that is along a single time slice. In this case, we will have to first replace the supertrace STr with the matrix element with respect to the global vacuum state $|0\rangle$. Next we will have to modify all the node transfer matrices along the boundary by setting $t_A = 1$ in Eq. (B.4) and also consider only T_+ since no bosons or fermions can be created or propagated across the boundary. Note that the 90° rotation of the boundary changes the corresponding t_A. Hence the single spin single node transfer matrix at the boundary is:

$$T_A = \prod_\sigma \exp\left[(f_\sigma^\dagger \bar{f}_\sigma^\dagger + b_\sigma^\dagger \bar{b}_\sigma^\dagger)\right]. \tag{B.9}$$

This operator commutes only with the four elements, $B + \bar{B}, Q_3 + \bar{Q}_3, W_+ + \bar{W}_+$ and $V_- + \bar{V}_-$ which form the subalgebra gl(1|1). This seems to contradict the previous

observation that a reflecting boundary along the vertical direction preserves the full sl(2|1) SUSY. This is reconciled by the fact that in the former case, we took the supertrace STr with a trivial boundary node transfer matrix while here we need to consider the action of the boundary transfer matrix T_A in Eq. (B.9) on the global vacuum $|0\rangle$. Using the relations in Eq. (B.1) and (B.2), we can check that the state $T_A|0\rangle$ is a singlet under the action of the sl(2|1) symmetry on the two links involved. That is, it is annihilated by the sum over two links of all eight generators of the sl(2|1) superalgebra. Thus the full supersymmetry is restored within a lattice spacing from the boundary and the result matches with the previous case. For simplicity, in the main text, we always assume that the boundary is along the vertical direction as shown in Fig. 3.1. This enables us to retain the global supertrace STr in all the expressions.

References

[1] P. W. Anderson, Phys. Rev. **109**, 1492 (1958).

[2] F. Evers and A. D. Mirlin, arXiv:0708.4378 .

[3] E. Abrahams, P. W. Anderson, D. C. Licciardello, and T. V. Ramakrishnan, Phys. Rev. Lett. **42**, 673 (1979).

[4] F. Wegner, Z. Phys. B **35**, 207 (1979).

[5] H. Levine, S. B. Libby, and A. M. M. Pruisken, Phys. Rev. Lett. **20**, 1915 (1983).

[6] A. A. Belavin, A. M. Polyakov, and A. B. Zamolodchikov, Nucl. Phys. **B241**, 333 (1984).

[7] A. Altland and M. R. Zirnbauer, Phys. Rev. B **55**, 1142 (1997), arXiv:cond-mat/9602137.

[8] M. R. Zirnbauer, J. Math. Phys. **37**, 4986 (1996), math-ph/9808012.

[9] J. L. Cardy, Nucl. Phys. **B324**, 581 (1989).

[10] A. W. W. Ludwig, M. P. A. Fisher, R. Shankar, and G. Grinstein, Phys. Rev. B **50**, 7526 (1994).

[11] A. D. Mirlin, Phys. Rep. **326**, 259 (2000), arXiv:cond-mat/9907126.

[12] A. R. Subramaniam, I. A. Gruzberg, A. W. W. Ludwig, F. Evers, A. Mildenberger, and A. D. Mirlin, Phys. Rev. Lett. **96**, 126802 (2006), arXiv:cond-mat/0512040.

[13] V. I. Fal'ko and K. B. Efetov, Europhys. Lett. **32**, 627 (1995).

[14] V. I. Fal'ko and K. B. Efetov, Phys. Rev. B **52**, 17413 (1995).

[15] F. Wegner, Z. Phys. B **36**, 209 (1980).

[16] J. L. Cardy, Nucl. Phys. **B240**, 514 (1984).

[17] A. D. Mirlin and F. Evers, Phys. Rev. B **62**, 7920 (2000), arXiv:cond-mat/0003332.

[18] E. Brezin and J. Zinn-Justin, eds., *Fields, Strings and Critical Phenomena, 1988 Les Houches Lectures* (North Holland, NY, 1990).

[19] P. D. Francesco, P. Mathieu, and D. Senechal, *Conformal Field Theory* (Springer Verlag, NY, 1997).

[20] J. L. Cardy, J. Phys. A **17**, L385 (1984).

[21] V. Kagalovsky, B. Horovitz, Y. Avishai, and J. T. Chalker, Phys. Rev. Lett. **82**, 3516 (1999), arXiv:cond-mat/9812155.

[22] T. Senthil, J. B. Marston, and M. P. A. Fisher, Phys. Rev. B **60**, 4245 (1999), arXiv:cond-mat/9902062.

[23] I. A. Gruzberg, A. W. W. Ludwig, and N. Read, Phys. Rev. Lett. **82**, 4524 (1999), arXiv:cond-mat/9902063.

[24] J. T. Chalker and P. D. Coddington, J. Phys. C **21**, 2665 (1988).

[25] J. T. Chalker and A. Dohmen, Phys. Rev. Lett. **75**, 4496 (1995), arXiv:cond-mat/9510164.

[26] I. A. Gruzberg, N. Read, and S. Sachdev, Phys. Rev. B **55**, 10593 (1997), arXiv:cond-mat/9612038.

[27] I. A. Gruzberg, N. Read, and A. W. W. Ludwig, Phys. Rev. B **63**, 104422 (2001), arXiv:cond-mat/0007254.

[28] N. Read and A. W. W. Ludwig, Phys. Rev. B **63**, 24404 (2001), arXiv:cond-mat/0007255.

[29] F. Merz and J. T. Chalker, Phys. Rev. B **65**, 54425 (2002), arXiv:cond-mat/0106023.

[30] J. T. Chalker, N. Read, V. Kagalovsky, B. Horovitz, Y. Avishai, and A. W. W. Ludwig, Phys. Rev. B **65**, 12506 (2002), arXiv:cond-mat/0009463.

[31] E. J. Beamond, J. Cardy, and J. T. Chalker, Phys. Rev. B **65**, 214301 (2002), arXiv:cond-mat/0201080.

[32] A. D. Mirlin, F. Evers, and A. Mildenberger, J. Phys. A **36**, 3255 (2003), arXiv:cond-mat/0105297.

[33] F. Evers, A. Mildenberger, and A. D. Mirlin, Phys. Rev. B **67**, 41303 (2003), arXiv:cond-mat/0203134.

[34] K. Efetov, *Supersymmetry in disorder and chaos* (Cambridge University Press, 1997).

[35] N. Read, (unpublished).

[36] R. J. Baxter, *Exactly solved models in statistical mechanics* (Academic Press, New York, 1982).

[37] H. W. Diehl and S. Dietrich, Z. Physik **B42**, 65 (1981).

[38] H. W. Diehl and S. Dietrich, Z. Physik **B43**, 281 (1981).

[39] H. W. Diehl, in C. Domb and J. Lebowitz., eds., *Phase Transitions and Critical Phenomena* (Academic, New York, 1986), vol. 10.

[40] H. Saleur and B. Duplantier, Phys. Rev. Lett. **58**, 2325 (1987).

[41] N. Read and H. Saleur, Nucl. Phys. **B777**, 316 (2007), arXiv:hep-th/0701117.

[42] P. de Gennes, *Scaling Concepts in Polymer Physics* (Cornell University Press, 1988).

[43] K. Binder, in C. Domb and J. Lebowitz, eds., *Phase Transitions and Critical Phenomena, Vol. 8* (Academic, New York, 1983), p. 1.

[44] M. Janssen, M. Metzler, and M. R. Zirnbauer, Phys. Rev. B **59**, 15836 (1999), arXiv:cond-mat/9810319.

[45] A. D. Mirlin, Y. V. Fyodorov, F.-M. Dittes, J. Quezada, and T. H. Seligman, Phys. Rev. E **54**, 3221 (1996), arXiv:cond-mat/9604163.

[46] L. S. Levitov, Phys. Rev. Lett. **64**, 547 (1990).

[47] L. S. Levitov and B. L. Altshuler, Phys. Rep. **288**, 487 (1997).

[48] Y. V. Fyodorov and A. D. Mirlin, Int. J. Mod. Phys. B **8**, 3795 (1994).

[49] M. F. Schlesinger, G. F. Zaslavsky, and J. Klafter, Nature **31**, 363 (1993).

[50] R. Metzler and J. Klafter, Phys. Rep. **339**, 1 (2000).

[51] G. Zumofen and J. Klafter, Phys. Rev. E **51**, 2805 (1995).

[52] R. Metzler and J. Klafter, Physica A **278**, 107 (2000).

[53] N. Krepysheva, L. D. Pietro, and M. C. Neel, Phys. Rev. E **73**, 021104 (2006).

[54] A. D. Mirlin, Y. V. Fyodorov, A. Mildenberger, and F. Evers, Phys. Rev. Lett. **97**, 046803 (2006).

[55] A. Mildenberger, A. R. Subramaniam, R. Narayanan, F. Evers, I. A. Gruzberg, and A. D. Mirlin, Phys. Rev. B **75**, 94204 (2007), arXiv:cond-mat/0611713.

[56] S. Hikami, A. I. Larkin, and Y. Nagaoka, Prog. Theor. Phys. **63**, 707 (1980).

[57] H. Obuse, A. R. Subramaniam, A. Furusaki, I. A. Gruzberg, and A. W. W. Ludwig, Phys. Rev. Lett. **98**, 156802 (2007), arXiv:cond-mat/0609161.

[58] M. Janssen, Int. J. Mod. Phys. B **8**, 943 (1994).

[59] K. v. Klitzing, G. Dorda, , and M. Pepper, Phys. Rev. Lett. **45**, 494 (1980).

[60] R. E. Prange and S. M. Girvin, eds. (Springer-Verlag, New York, 1990).

[61] D. E. Khmelnitskii, JETP Lett. **38**, 552 (1983).

[62] H. Obuse, A. R. Subramaniam, A. Furusaki, I. A. Gruzberg, and A. W. W. Ludwig, Physica E **40**, 1404 (2008), arXiv:cond-mat/0609161.

[63] M. R. Zirnbauer, arXiv:hep-th/9905054 .

[64] M. J. Bhaseen, I. I. Kogan, O. A. Soloviev, N. Taniguchi, and A. M. Tsvelik, Nucl. Phys. **B580**, 688 (2000).

[65] A. M. Tsvelik, Phys. Rev. B **75**, 184201 (2007).

[66] A. LeClair, arXiv:0710.3778 .

[67] M. Bershadsky, S. Zhukov, and A. Vaintrob, Nucl. Phys. **B559**, 205 (1999), arXiv:hep-th/9902180.

[68] N. Berkovits, C. Vafa, and E. Witten, J. High Energy Phys. **03**, 018 (1999), arXiv:hep-th/9902098.

[69] R. Klesse and M. R. Zirnbauer, Phys. Rev. Lett. **86**, 2094 (2001), arXiv:cond-mat/0010005.

[70] F. Evers, A. Mildenberger, and A. D. Mirlin, Physical Review B **64**, 241303 (2001), arXiv:cond-mat/0105297.

[71] C. Mudry, C. Chamon, and X.-G. Wen, Nucl. Phys. **B466**, 383 (1996), arXiv:cond-mat/9509054.

[72] R. Gade and F. Wegner, Nucl. Phys. **B360**, 213 (1991).

[73] R. Gade, Nucl. Phys. **B398**, 213 (1993).

[74] S. Guruswamy, A. LeClair, and A. W. W. Ludwig, Nucl. Phys. **B583**, 475 (2000), arXiv:cond-mat/9909143.

[75] M. Bocquet and J. T. Chalker, Phys. Rev. B **67**, 054204 (2004), arXiv:cond-mat/0210695.

[76] H. Obuse, A. R. Subramaniam, A. Furusaki, I. A. Gruzberg, and A. W. W. Ludwig, Phys. Rev. Lett. **101**, 116802 (2008), arXiv:0804.2409.

[77] F. Evers, A. Mildenberger, and A. D. Mirlin, Phys. Rev. Lett. **101**, 116803 (2008), arXiv:0804.2334.

[78] T. Osborne and M. Nielsen, Phys. Rev. A **66**, 32110 (2002).

[79] P. Calabrese and J. Cardy, J. Stat. Mech. **6**, 2 (2004).

[80] G. Vidal, J. I. Latorre, E. Rico, and A. Kitaev, Phys. Rev. Lett. **90**, 227902 (2003).

[81] A. Kopp, X. Jia, and S. Chakravarty, Ann. Phys. **322**, 1466 (2007).

[82] L. A. Wu, M. S. Sarandy, and D. A. Lidar, Phys. Rev. Lett. **93**, 250404 (2004).

[83] G. Refael and J. E. Moore, Phys. Rev. Lett. **93**, 260602 (2004).

[84] R. Santachiara, J. Stat. Mech. **06**, L002 (2006).

[85] I. Varga and J. A. Mendez-Bermudez, Phys. Stat. Sol. (C) **5**, 867 (2008), arXiv:0708.3682.

[86] P. Zanardi, Phys. Rev. A **65**, 42101 (2002).

[87] A. MacKinnon and B. Kramer, Phys. Rev. Lett. **47**, 1546 (1981).

[88] K. Slevin, P. Markos, and T. Ohtsuki, Phys. Rev. Lett. **86**, 3594 (2001).

[89] P. Goswami, X. Jia, and S. Chakravarty, Phys. Rev. B **76**, 205408 (2007), (refer Appendix C), arXiv:0706.3737.

[90] B. Kramer and M. Schreiber, in K. H. Hoffmann and M. Schreiber, eds., *Computational Physics* (Springer, Berlin, 1996), p. 166.

[91] B. Bulka, M. Schreiber, and B. Kramer, Z. Phys. B **66**, 21 (1987).

[92] F. Wegner, Z. Phys. B **44**, 9 (1981).

[93] M. Scheunert, W. Nahm, and V. Rittenberg, J. Math. Phys. **18**, 155 (1977).

[94] I. A. Gruzberg, A. W. W. Ludwig, and N. Read, (unpublished).